

Proceedings of the 2008 Mathematics and Statistics in Industry Study Group

Editors: Tim Marchant, Maureen Edwards and Geoff Mercer



Proceedings of the
2008 Mathematics and Statistics in Industry
Study Group, MISG2008

Director: Professor Tim Marchant
Associate Director: Dr Maureen Edwards
School of Mathematics and Statistics
University of Wollongong

Editors: Professor Tim Marchant, Dr Maureen Edwards and A/Professor Geoff Mercer
Administrator and Assistant Editor: Ms Joell Hall

First published in Australia January 2009

©MISG2008 (Mathematics and Statistics in Industry Study Group, School of Mathematics and Applied Statistics, University of Wollongong)

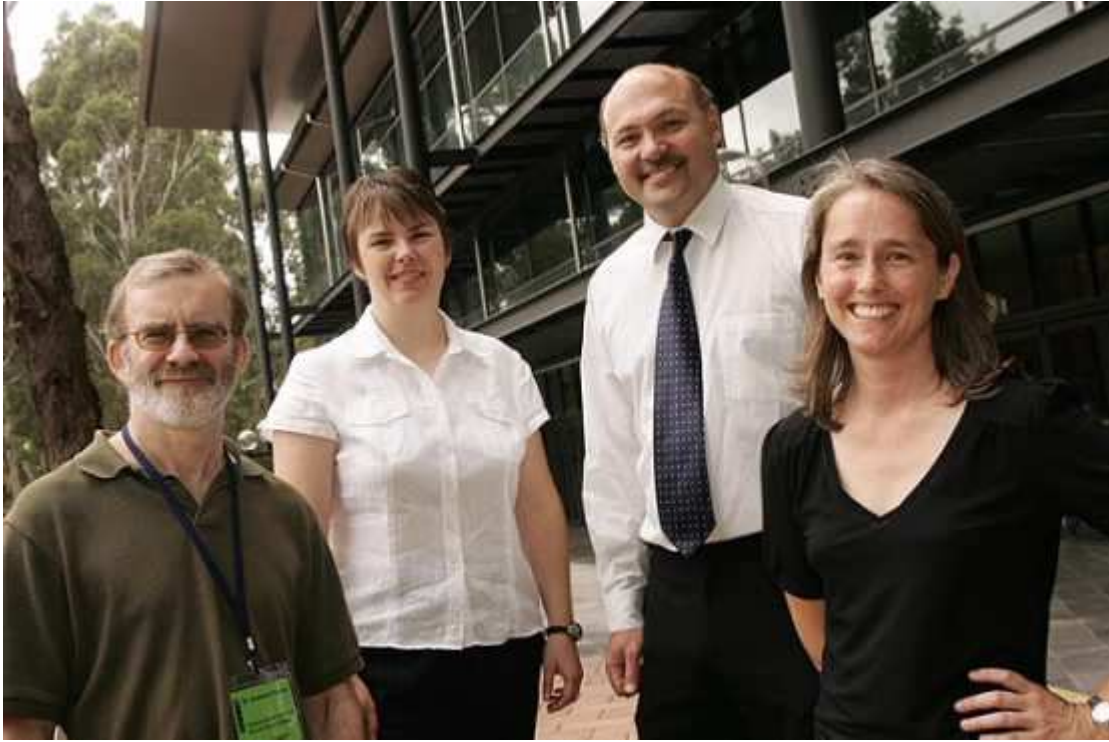
This book is copyright. Apart from any fair dealings for the purpose of private study, research, criticism or review, as permitted under the Copyright Act, no part may be reproduced by any process without written permission. Enquiries should be made to the publisher.

All manuscripts for the Proceedings of the MISG were written by the moderators in consultation with company representatives. Manuscripts submitted to the Editors, Prof Tim Marchant, Dr Maureen Edwards and A/Prof Geoff Mercer, were subsequently reviewed by expert referees. On the advice of the referees all manuscripts were accepted for publication subject to the recommended revisions, and then formally approved by the editorial committee.

ISBN 978-0-646-50544-2

Mathematics in
Industry
Study
Group
2008

Preface



MISG2008 Opening Ceremony: From left, Prof Andrew Fowler, Universities of Limerick and Oxford, Dr Jane Sexton, Geoscience Australia, Prof Tim Marchant, Director MISG2008 and Dr Maureen Edwards, A/Director MISG2008

The Mathematics and Statistics in Industry Study Group (MISG2008), was hosted by the University of Wollongong during the week January 28 - February 1, 2008, at the University of Wollongong. The MISG is a special interest meeting of ANZIAM, the Australian and New Zealand Society for Applied and Industrial Mathematics. The event was directed by Prof Tim Marchant and Dr Maureen Edwards from the University of Wollongong. Administrative support was ably supplied by Ms Joell Hall.

Seven industry projects were presented; five of these came from Australia and two from New Zealand. There was broad range of project themes which covered the fields of applied mathematics, statistics and financial mathematics. MISG2008 had 100 attendees, including 20 postgraduate students.

MISG2008 was opened by Prof Lee Astheimer, Pro-Vice Chancellor, Research, University of Wollongong. The plenary speaker was Prof Andrew Fowler, from the Universities of Limerick and Oxford. Prof Jim Hill and Dr Milorad Kovacevic also presented invited talks.

The Australian Mathematics Sciences Institute (AMSI) supported postgraduate attendance

at MISG2008. Thanks go to AMSI and to the University of Wollongong for their financial support.

Due to the broad range of skills required to tackle modern industrial mathematics problems many high-profile scientists from the Australian and NZ Statistics and Financial Mathematics communities attended MISG2008 as delegates or moderators. If the MISG meeting is to remain relevant and important in the coming years then this multi-disciplinary approach to industrial problem solving needs to continue, with participation at MISG from all the Mathematical Sciences.

Our thanks go to all of these people and organisations, and of course, to the project moderators. The moderators take responsibility for the industry projects and put in an inordinate amount of time and effort. These contributions are critical to the success of MISG.

Tim Marchant & Maureen Edwards, Directors MISG2008

Contents

Preface	3
Sponsors	6
Projects	7
Overheard in passing ...	9
Delegates	10
Geoscience Australia, Tsunami risk modelling for Australia: Understanding the impact of data	12
<i>G.C. Hocking, J. Jakeman, J. Sexton and M. Wand</i>	
New Zealand Steel, Annealing steel coils	26
<i>M. McGuinness, W. Sweetman, D. Boawan and S. Barry</i>	
Transpower NZ, The response of power systems to autonomous “grid friendly” devices	46
<i>B. Whiten, G. Fulford, R. Hickson and G. Pritchard</i>	
Provisor and Food Science Australia, The shelf life of wine	67
<i>G. Mercer, A. Wilkins, J. Crook, S. Barry and A. Fowler</i>	

MISG2008 SPONSORS

The organisers of MISG2008 gratefully acknowledge all contributions that were made by the sponsors:

Host of MISG2008

University of Wollongong

Financial Sponsors

Australian Mathematical Sciences Institute

Project Sponsors

Australian Bureau of Statistics

Food Science Australia

Geoscience Australia

Integral Energy

Provisor

New Zealand Steel

Transpower, NZ

Projects

Australian Bureau of Statistics

The table builder problem

Industry Contact:	Ms Melanie Black	ABS
Moderators:	Dr Christine O’Keefe Prof Steve Haslett A/Prof Robert Mellor	CSIRO Massey University University of Western Sydney
Student Moderator:	Mr Wilford Molefe	University of Wollongong

Geoscience Australia

Tsunami risk modelling for Australia: understanding the impact of data

Industry Contact:	Dr Jane Sexton	Geoscience Australia
Moderators:	A/Prof Graeme Hocking Prof Matt Wand	Murdoch University University of Wollongong
Student Moderator:	Mr John Jakeman	Australian National University

Integral Energy

Diagnostic testing for earnings simulation engines in the Australian electricity market

Industry Contact:	Dr Andrew Ziogas	Integral Energy
Moderators:	Prof Carl Chiarella Dr Max Stevenson	University of Technology, Sydney University of Sydney

Integral Energy

Optimising Trading Strategies

Industry Contact:	Dr Adam Kucera	Integral Energy
Moderators:	A/Prof Jeff DeWynne Dr Will Bertram	University of Wollongong University of Sydney
Student Moderator:	Mr. Cheng Jun	Shanghai University of Technology

New Zealand Steel
Annealing steel coils

Industry Contacts: Dr Philip Bagshaw NZ Steel
Dr Jason Mills NZ Steel

Moderators: A/Prof Mark McGuinness Victoria University of Wellington
Dr Winston Sweatman Massey University

Student Moderator: Ms DuangKamon Baowan University of Wollongong

Provisor and Food Science Australia
Shelf life of wine

Industry Contacts: Dr Philip Giesbertz Provisor
Dr Francisco Trujillo Food Science Australia

Moderators: A/Prof Geoff Mercer Australian Defence Force Academy
Dr Andy Wilkins CSIRO

Student Moderator: Mr Jonathon Crook Victoria University of Wellington

Transpower NZ
The response of power systems to autonomous “grid friendly” devices

Industry Contacts: Dr Doug Goodwin Transpower
Dr Cynthia Liu Transpower

Moderators: Prof Bill Whiten University of Queensland
Dr Glenn Fulford Queensland University of Technology

Student Moderator: Ms Roslyn Hickson Australian Defence Force Academy

Overheard in Passing...

Ken Russell - *I once wrote a limerick that ends in hetroscedasticity.*

Ruth Luscombe - *The problem is soluble, just add water and it has a solution.*

Tony Gibb - *The power function is initially cubic then constant before it drops suddenly to zero - I am using a linear approximation.*

Andrew Dixon - *When I say thin, I mean not thick.*

Ken Russell - *That sounds so logical; we must have done something wrong.*

David Marlow - *So it's not just a question of a buckle being a fulfilled wrinkle.*

Patrick Tobin - *Its somewhere between the waylines; let's call it the half-way line.*

Ruth - *When do you not go backwards?* Judy - *When there are no ships behind you.*

And the Grand Winners of MISG2008 overheard in passing...

Phil Kilby - *The undetected ships are displayed in Cyan, which is apparently a bad colour to use.*

Ken Russell - *That's why they're undetected*

Ahn,	Ms	Seonmin	KAIST
Anand,	Dr	Tularam	Griffith University
Arundell,	Dr	Justin	Integral Energy
Bagshaw,	Mr	Phil	New Zealand Steel
Baloi,	Ms	Luminita	University of Queensland
Baowan,	Ms	Duangkamon(Yui)	University of Wollongong
Barry,	Dr	Steven	UNSW at ADFA
Bertram,	Dr	Will	University of Sydney
Bianco,	Ms	Sabrina	University of Wollongong
Black,	Ms	Melanie	Australian Bureau of Statistics
Blakers,	Ms	Rachel	Geoscience Australia
Britz,	Dr	Thomas	University of New South Wales
Byrne,	Dr	Graeme	La Trobe University
Chambers,	Prof	Ray	University of Wollongong
Chan,	Mr	Yue	University of Wollongong
Chen,	Mr	Weiming	Massey University
Cheng,	Mr	Jun	University of Wollongong
Chiarella,	Prof	Carl	University of Technology Sydney
Choy,	Dr	Boris	University of Technology Sydney
Clarke,	Dr	Simon	Monash University
Clements,	Dr	David	University of Adelaide
Cogill,	Dr	John	Retired
Cox,	Dr	Barry	University of Wollongong
Cox,	Dr	Grant	University of Wollongong
Crook,	Mr	Jonathan	Victoria University of Wellington
Davy,	Dr	Pam	University of Wollongong
Denny,	Ms	Sue	University of Wollongong
Dewynne,	Dr	Jeff	University of Wollongong
Doherty,	Dr	Greg	Uow and ANSTO
Edwards,	Dr	Maureen	University of Wollongong
Fowler,	Dr	Andrew	University of Limerick/ Oxford
Fulford,	Dr	Glenn	Queensland University of Technology
Garanovich,	Mr	Ivan	Australian National University
Georgiev,	Dr	Dian	University of Southern Queensland
Giesbertz,	Mr	Philip	Provisor
Goodwin,	Mr	Doug	Transpower New Zealand Ltd
Griffiths,	Prof	David	University of Wollongong
Hall,	Ms	Joell	University of Wollongong
Haslett,	Prof	Stephen	Massey University
Hickson,	Ms	Roslyn	UNSW at ADFA
Hill,	Prof	Jim	University of Wollongong
Hocking,	A/Prof	Graeme	Murdoch University
Jakeman,	Mr	John	Australian National University
Jovanoski,	Dr	Zlatko	UNSW at ADFA PEMS
Kang,	Mr	Byunghoon	KAIST
Kang,	Mr	Sinuk	KAIST

Kim,	Ms	Minjeong	KAIST
Kovacevic,	Dr	Milorad	STATS Canada
Kucera,	Dr	Adam	Integral Energy
Laird,	Dr	Philip	University of Wollongong
Lee,	A/Prof	Chang-Ock	KAIST
Liu,	Ms	Cynthia	Transpower NZ Ltd
Lu,	Dr	Xiaoping	University of Wollongong
Mackay,	Mr	Andrew	New Zealand Steel
Maher,	Mr	Stephen	University of Wollongong
Marchant,	A/Prof	Tim	University of Wollongong
Marion,	Ms	Kaye E.	RMIT University
McCrae,	A/Prof	Michael	University of Wollongong
McGuinness,	Dr	Mark	Victoria University of Wellington
Mellor,	A/Prof	Robert	University of Western Sydney
Mercer,	Dr	Geoff	UNSW at ADFA
Mills,	Mr	Jason	NZ Steel
Min,	Mr	Nam Chang	KAIST
Mitchell,	Mr	Lewis	University of Wollongong
Molefe,	Mr	Wilford	University of Wollongong
Musicki-Kovacevic,	Dr	Vesna	Oracle Corp
Nelson,	Dr	Mark	University of Wollongong
O'Keefe,	A/Prof	Christine	CSIRO
Pritchard,	Dr	Geoffrey	University of Auckland
Ramagge,	A/Prof	Jacqui	University of Wollongong
Roberts,	Ms	Melanie	University of Western Australia
Sciberras,	Mr	Luke	University of Wollongong
Sexton,	Dr	Jane	Geoscience Australia
Shteinman,	Mr	David	ARC Centre of Excellence MASCOS
Snow,	Ms	Kate	University of Wollongong
Sozio,	Mr	Gerry	St Mary Star of the Sea College
Steel,	Prof	David	University of Wollongong
Stevenson,	Dr	Max	University of Sydney
Storozhev,	Dr	Andrei	Australian Mathematics Trust
Subhani,	Mr	Salman	University of Wollongong
Sweatman,	Dr	Winston	Massey University
Thamwattana,	Dr	Ngamta (Natalie)	University of Wollongong
Thornton,	Mr	Aaron	University of Wollongong
Tritscher,	Dr	Peter	University of Wollongong
Trujillo,	Mr	Francisco Javier	Food Science Australia
Wand,	Prof	Matt	University of Wollongong
Whiten,	Prof	Bill	University of Queensland
Wilkins,	Dr	Andy	University of Queensland
Williams,	A/Prof	Graham	University of Wollongong
Yuen,	Dr	Daniel	Bluescope Steel
Zhu,	Prof	Song-Ping	University of Wollongong
Ziogas,	Dr	Andrew	Integral Energy

Tsunami risk modelling for Australia: understanding the impact of data

Graeme Hocking
Murdoch University

John Jakeman
Australian National University

Jane Sexton
Geoscience Australia

Matt Wand
University of Wollongong

1 Introduction

Modelling the impacts from tsunami events is a complex task. The approach taken by Geoscience Australia is a hybrid one where two models are combined. The first is one which models the earthquake rupture and subsequent propagation in deep water with the second propagating the tsunami through shallow water and focusing on subsequent inundation and impact ashore. The computer model ANUGA is used for the latter part of the approach and was developed collaboratively between the Australian National University and Geoscience Australia.

A critical requirement for reliable modelling is an accurate representation of the earth's surface that extends from the open ocean through the inter-tidal zone into the onshore areas. However, this elevation data may come from a number of sources and will have a range of reliability.

There are two questions that arise when data is requested. The first deals with the true variability of the topography, e.g. a flat surface needn't be sampled as finely as a highly convoluted surface. The second relates to sensitivity; how large is the error in the modelled output if the range of errors in the elevation data is known? ANUGA and similar models can take up days of computer time to simulate a particular scenario, and so full comparative tests for a range of input values is not viable. The main aim of this project was to understand the uncertainties in the outputs of the inundation model based on possible uncertainty in the input data.

2 The model

ANUGA is a model based on the shallow-water or depth integrated equations of fluid flow (see [10]). These are used in the form

$$h_t + (uh)_x + (vh)_y = 0 \tag{1}$$

$$(uh)_t + (u^2h + gh^2/2)_x + (vuh)_y + gh(z_x + S_{fx}) = 0 \quad (2)$$

$$(vh)_t + (vuh)_x + (v^2h + gh^2/2)_y + gh(z_y + S_{fy}) = 0 \quad (3)$$

where uh and vh are momentum in the x and y -directions, respectively, $z(x, y, t)$ is the bottom elevation, g is acceleration due to gravity, and $h(x, y, t)$ is the total water depth (above the terrain), so that $h(x, y, t)$ incorporates the contribution of the wave in addition to the existing depth of the water column. When the terrain represents the onshore elevation, $h(x, y, t)$ simply measures the height of water above the ground. The quantities S_{fx} and S_{fy} are the bottom friction modelled using Manning's resistance law as

$$S_{fx} = \frac{u\eta^2(u^2 + v^2)^{1/2}}{h^{4/3}} \quad \text{and} \quad S_{fy} = \frac{v\eta^2(u^2 + v^2)^{1/2}}{h^{4/3}}$$

where η is the Manning resistance coefficient. The three model equations can be simplified to two by subtracting the mass conservation terms, but it is in the form given that they are solved in the model.

The model equations (1)-(3) are solved on a variable triangular mesh over the region of interest using a finite volume method. There are a number of models of similar type described in the literature using both this approach and the Boussinesq equations. These have been verified across a wide range of situations by comparison with both experimental and field data, to the extent that it is clear that the models do a good job of predicting the flow in shallow water, (or when the wavelength clearly exceeds the water depth), and subsequent runup of the tsunami wave [5, 8, 9, 11, 17]. This particular model (ANUGA) consequently has been shown to be accurate for a series of flow simulations including dam breaks and tsunamis [10].

These facts allowed the Mathematics and Statistics in Industry Study Group (MISG) group to assume the model to be sufficiently accurate to be used as a tool to determine the variations caused by errors in the input data. Variations in the runup of the tsunami can be treated as resulting purely from the changes in the input (topographic and wave) data, rather than from the model itself. This assumption also allowed us to consider using other similar models or even using analytic calculations to determine the variability due to variations in the input data.

3 Approach

The standard approach to finding the errors in a model of this kind is to perform a series of simulations varying the grid-spacing, time stepping and data inputs. Nonetheless, as stated above, this is not possible for the real situations under consideration because of time constraints. The best approach would therefore seem to be to follow the same process but with some much simpler scenarios that can be run quickly and easily. By necessity, these simulations were run on a coarse grid and with a greatly simplified geometry, and some more refined tests would need to be completed after the workshop to verify the conclusions. However, the results of these simple simulations may be assumed to be representative of the full simulations, and also to provide a framework for future tests outside of the time constraints provided by the MISG.

Therefore, the main activities undertaken by the workshop can be placed into four categories;

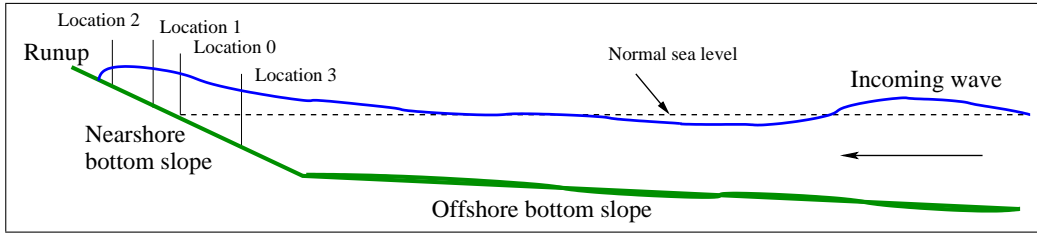


Figure 1: Simple one dimensional coastal scenario used in baseline simulations

- Sensitivity analysis using simple one and two dimensional situations to compute a table of first and second order variations in each output given each input, testing both sensitivity and nonlinearity.
- Monte Carlo simulations, using a simple model scenario, in which a random distribution of a particular input about some mean value was used in the simulation, and then considering the distribution of the output quantities.
- Consideration of other models to see if some simple or analytic expressions could be derived for the error.
- Determination of the sampling locations to adequately resolve the bottom topography.

In order to address the first three, the group decided on a scenario with a simple plane beach along a 50m wide strip, extending 2000m offshore, with two piecewise linear segments; one approaching the shore and one running up onto the inundation zone, see Figure 1. The bottom segment furthest out from the shore was also perturbed by a sinusoidal function to provide some variation away from a simple slope. To allow some two dimensional effects, some simulations involved a lateral, sinusoidal perturbation as well. Using this simple case, simulations ran in a matter of seconds. Due to the time constraints of the one week workshop, the activities outlined above were carried out in parallel, so it was not possible to use the results of one approach to refine the others.

In order to compare the results of the simulations, a measure is required, such as the inundation extent. As ANUGA uses an unstructured triangular mesh, the mesh vertices do not run parallel to the beach and so it was not possible to compare the extent of inundation directly between simulations unless an extremely fine grid was employed. This measure was used initially and an error of magnitude equal to the local grid resolution became evident in trial runs. Therefore, it was decided to measure the maximum ocean elevation at several points along the middle of the strip from just above the normal ocean level to just offshore within the inundation zone. The maximum elevation at these points can therefore be used as a proxy for runup. The four locations chosen are illustrated in Figure 1, and identified as Location 0, at the usual shoreline, Location 1, 0.55m above the shoreline, Location 2, 1.22m above the usual shore level, and Location 3 at 2.44m below the shoreline. The elevations at these locations are denoted as h_0, h_1, h_2 and h_3 respectively, and the horizontal velocities at these locations are denoted by v_0, v_1, v_2 and v_3 .

3.1 Sensitivity Assessment

Perhaps the most successful approach considered at MISG was a process in which the rate of variation of the outputs was computed from a series of simulations in which each of the input data values in turn was perturbed about some control value. This is sometimes called a first and second order local sensitivity assessment [12]. In other words, a very simple scenario was considered and the outputs computed. Then, in turn, each of the parameters of interest was varied by a small amount, in this case by $\Delta_5 = 0.5\%$ of the control value, while all others were kept at the control value. This gives an approximation to the local dependence of the model outputs on each of the individual inputs, or a first derivative of the model outputs with respect to each of the model inputs - a Jacobian matrix. Thus, if $H(I_C)$ is the value of the output parameter at the control value, where I is the input parameter, then

$$\frac{\delta H}{\delta I} \approx \frac{H(I_C + \Delta_5 I) - H(I_C)}{\Delta_5 I}$$

gives an approximation to the rate at which H changes as I is varied.

For example, if we choose the input parameter to be the bottom slope, the inundation level could be computed at a particular value of slope, the slope changed slightly and then the inundation recalculated. The change in inundation level is an estimate of how strongly the output depends on this particular input. This can then be repeated for other factors.

A second series of simulations with a variation of $\Delta_{25} = 0.25\%$ was also conducted. This allows an approximation to the second derivative to be calculated for the output dependence on each factor and hence provides an estimate of the degree of nonlinearity in the response. If this estimate is zero, then the response is linear. Using standard centered differences, this means that

$$\frac{\delta^2 H}{\delta I^2} \approx \frac{H(I_C + \Delta_5 I) - 2H(I_C + \Delta_{25}) + H(I_C)}{(\Delta_{25} I)^2}$$

provides an estimate for the nonlinearity of the relationship between H and I .

The parameters to be tested were bottom friction, input wave height, bottom slope, wavelength of the bottom oscillation and amplitude of the bottom oscillation. In the first two test cases, no variation was allowed in the lateral direction. The model consequently solved what is essentially a one dimensional problem. The ‘‘full’’ simulation took a matter of seconds and so output data were easily generated.

Two cases were considered using this one dimensional test. In the first, the control parameters were; bottom slope $S_B = 1/40$, input wave amplitude $A_I = 1\text{m}$, Manning friction coefficient $\eta = 0.01$, bottom oscillation amplitude $A_B = 1\text{m}$ and bottom oscillation wavelength $\lambda_B = 100\text{m}$. The values selected are representative of tsunami; the bottom slope is reasonable for many nearshore beach slopes and tsunami amplitudes of 1m are entirely plausibly in 100m water depth. The Manning friction coefficient is representative of the nearshore bottom slope, (often η is given the value of 0.015 for smooth terrains such as grasslands, 0.03 for built up areas and 0.07 for landscapes with densely covered forest, therefore the value selected for η in this work is representative of the nearshore environment). Tsunami typically have much longer wavelength than that chosen here, however, for the purposes of the exercise and to speed up computations, a much shorter wavelength was used (otherwise a much larger computational domain would have been required). The input wave at the outer boundary (the right hand boundary in Figure 1) had the form $A_I \sin \omega t$ with $A_I = 1\text{m}$ and $\omega = 1/100$. A range of input waves could have been selected here and the sine wave was chosen for its

simplicity and is often used to compare with the non-breaking analytical solutions of Carrier and Greenspan [3]. Other options include solitary waves and N-waves as suggested by Tadepalli and Synolakis [15]. It must be noted here that the purpose of the exercise was to develop a methodology for investigating sensitivity that will be applied to tsunami examples in the future and thus regardless of the type of the input wave, the methodology still stands. The bottom oscillation wavelength was chosen to be long compared to the local grid spacing so that it was accurately represented. The results are shown in Tables 1 and 2. Table 1 is the numerically approximated Jacobian, while Table 2 shows computations of the second derivative and hence shows the nonlinearity. In each case, the row that contains the largest absolute numbers is the dominant influence on the output variables.

Jacobian	h_0	h_1	h_2	h_3	v_0	v_1	v_2	v_3
Bottom Friction	-0.0000	-0.0000	-0.0000	-0.0000	-0.0001	0.0001	0.0002	-0.0002
Input Wave Amplitude	0.0240	0.0340	0.0478	0.0114	0.0485	0.0678	0.0900	0.0308
Bottom Oscillation Period	-0.0005	-0.0008	-0.0011	-0.0002	0.0011	0.0011	0.0003	0.0007
Bottom Slope	-0.0018	-0.0024	-0.0033	-0.0009	0.0030	0.0028	0.0025	0.0022
Bottom Oscillation Amplitude	0.0003	0.0004	0.0006	0.0001	0.0005	0.0011	0.0013	0.0002

Table 1: Jacobian matrix - Run 1. The dominant row is ‘Input Wave Amplitude’.

	h_0	h_1	h_2	h_3	v_0	v_1	v_2	v_3
Bottom Friction	0.0007	0.0031	0.0072	0.0014	0.0527	-0.0975	-0.3048	0.2510
Input Wave Amplitude	-39.4539	-55.9124	-78.5101	-18.0534	-77.4300	-112.8141	-147.7459	-49.6513
Bottom Oscillation Period	0.8779	1.2916	1.8720	0.3607	-0.9700	-0.8461	0.4121	-0.7944
Bottom Slope	2.6535	3.6376	4.9962	1.4277	-6.9591	-6.6874	-5.5659	-4.8113
Bottom Oscillation Amplitude	-0.4357	-0.6279	-0.8973	-0.1959	-0.9226	-1.0726	-2.4443	-0.2227

Table 2: Second derivative (Nonlinearity) matrix - Run 1. The dominant row is ‘Input Wave Amplitude’.

The second test series used the values; bottom slope $S_B = 1/20$, incoming wave amplitude $A_I = 1\text{m}$, Manning friction coefficient $\eta = 0.02$, bottom oscillation amplitude $A_B = 2\text{m}$, bottom oscillation wavelength $\lambda_B = 50\text{m}$. The incoming wave was chosen as above. The results are shown in Tables 3 and 4.

Jacobian	h_0	h_1	h_2	h_3	v_0	v_1	v_2	v_3
Bottom Friction	-0.0000	-0.0000	0.0025	-0.0000	-0.0003	-0.0044	-0.0039	-0.0002
Input Wave Amplitude	0.0486	0.1116	0.4889	0.0157	0.0973	0.0422	0.2110	0.0576
Bottom Oscillation Period	0.0007	0.0018	0.0080	0.0002	0.0034	-0.0005	0.0049	0.0018
Bottom Slope	-0.0009	-0.0020	-0.0080	-0.0003	0.0109	0.0017	-0.0042	0.0082
Bottom Oscillation Amplitude	0.0003	0.0008	0.0031	0.0001	0.0001	0.0001	0.0017	-0.0000

Table 3: Jacobian matrix - Run 2. The dominant row is ‘Input Wave Amplitude’.

In both of these one dimensional scenarios, it is clear that the row that measures the changes due to variation in incoming wave amplitude, A_I , is an order of magnitude larger than the variation due to the other input variables that are related to the topography. If substantiated across the spectrum of parameter values, this is a very significant result, because it implies that unless the amplitude of the incoming wave is known very accurately, the error in the simulation of inundation will be dominated by the uncertainty in this factor.

In a third test case, a lateral (alongshore) oscillation in the bottom topography was included, as shown with significant vertical exaggeration in Figure 2. The width of the region

Non-Linearity	h_0	h_1	h_2	h_3	v_0	v_1	v_2	v_3
Bottom Friction	-0.0112	-0.03783	2.0222	-0.0027	-0.2286	-3.5136	-3.0792	-0.1509
Input Wave Amplitude	38.6997	88.8546	403.7461	12.5231	78.3693	33.8159	153.7179	46.2542
Bottom Oscillation Period	0.5592	1.4251	6.2283	0.1357	2.6693	-0.2462	3.8037	1.5023
Bottom Slope	-0.7503	-1.6836	-6.6934	-0.2673	9.2542	0.4028	-3.4113	6.4378
Bottom Oscillation Amplitude	0.2585	0.5990	2.4468	0.0797	0.0295	0.2014	1.3887	-0.0191

Table 4: Second derivative matrix - Run 2. The dominant row is ‘Input Wave Amplitude’.

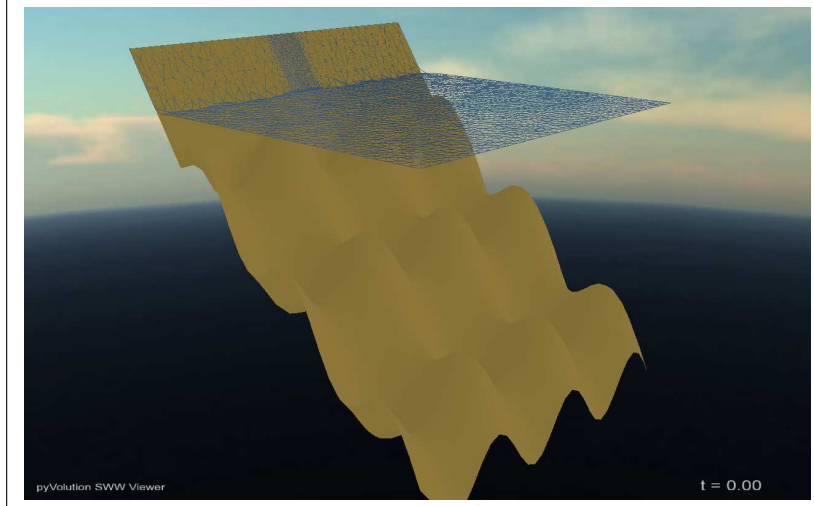


Figure 2: Diagram of the simulation geometry with lateral oscillations in the bottom bed.

was increased to $2000m$ so that some lateral effects could be seen. The onshore component was still broken into two components, and the inshore component was not perturbed laterally. This gives a first pass at determining the effect of lateral variations on the model outputs. The control was computed using the first case above with the added lateral perturbation with amplitude of $A_L = 1m$ and a bottom wavelength of $\lambda_L = 100m$.

Again, as in the one dimensional cases, it was found that the amplitude of the incoming wave was the dominant factor by an order of magnitude on the value of the outputs. It also, again, turned out to be the term that exhibited the most nonlinear response.

This test needs to be performed over a range of control parameter values to ensure that there are no special cases. For example, there may be a bottom oscillation wavelength that will resonate with the wavelength of the incoming wave, causing significant steepening. In addition, one must be mindful that these tests do not take into account sudden bathymetric changes or focusing effects from the coastline; two dimensional effects that may cause ‘catastrophic’ changes in the inundation. However, these tests can be repeated easily and quickly over the full range of possible inputs, and hence some reliability can be determined about the results.

3.2 Monte Carlo simulations

This series of tests was implemented as a comparison with the results above, and was performed in parallel. A similar coastal shape scenario was used to that above, but the simula-

Jacobian	h_0	h_1	h_2	h_3	v_0	v_1	v_2	v_3
Bottom Friction	0.0000	0.0000	0.0000	0.0000	-0.0003	-0.0007	-0.0008	-0.0004
Input Wave Amplitude	0.0247	0.0328	0.0545	0.0117	0.0428	0.0579	0.0970	0.0289
Bottom Oscillation Period	0.0003	0.0005	0.0008	0.0001	0.0020	0.0021	0.0010	0.0014
Bottom Slope	-0.0004	-0.0005	-0.0009	-0.0002	0.0034	0.0027	0.0030	0.0031
Bottom Oscillation Amplitude	0.0001	0.0001	0.0002	0.0000	0.0003	0.0002	0.0005	0.0001

Table 5: Jacobian with lateral oscillations. The dominant row is ‘Input Wave Amplitude’.

Non-Linear	h_0	h_1	h_2	h_3	v_0	v_1	v_2	v_3
Input Wave Amplitude	-39.4822	-53.3244	-89.0271	-18.6628	-69.7723	-93.6795	-163.0223	-46.6794
Bottom Slope	0.6532	0.8762	1.4873	0.3573	-4.8038	-5.0484	-5.0257	-4.5641
Bottom Friction	-0.0216	-0.0297	-1.5316	-0.2278	-0.8917	0.0905	1.0824	-1.5286
Bottom Oscillation Period	-0.5747	-0.8426	-1.5316	-0.2278	-0.8917	0.0905	1.0824	-1.5286
Bottom Oscillation Amplitude	-0.1246	-0.1660	-0.2769	-0.0568	-0.1736	-0.4351	-0.9721	-0.2110

Table 6: Second derivative with lateral oscillations. The dominant row is ‘Input Wave Amplitude’.

tions were performed with a number of randomized variations in the input parameters. This method is known as probabilistic Monte-Carlo simulation [12] and is shown schematically in Figure 3. The drawback of this approach is the large number of simulations that must be performed to determine a representative distribution. The advantage is that a much wider variation in each parameter can be considered in a series of simulations, for example a 20% variation around a particular value rather than the 0.5% considered in the above tests.

In this approach, the value of one input parameter was varied in a random, but normally distributed fashion while all other input values were held fixed. The idea is that this would be repeated for each of the input values. During the MISG a series of simulations were conducted in which the wavelength of the bottom bathymetry perturbation was varied about a mean of $\lambda_B = 100$ with a standard deviation of $s(\lambda_B) = 20$, using the Python normal/random distribution. Again, the maximum height of water above each of the test locations was recorded as for the one dimensional test case.

The randomly simulated distribution of input values seen in Figure 4 suggests that more simulations than time permitted at MISG are required to achieve a normal distribution. However, we were still able to draw some preliminary conclusions.

The distribution of the resultant maximum water depths at each of the four test locations is shown in Figure 5. The main outcome of the four plots shown is that the variance in the water depth is extremely small in comparison with the variance in the input (period of the

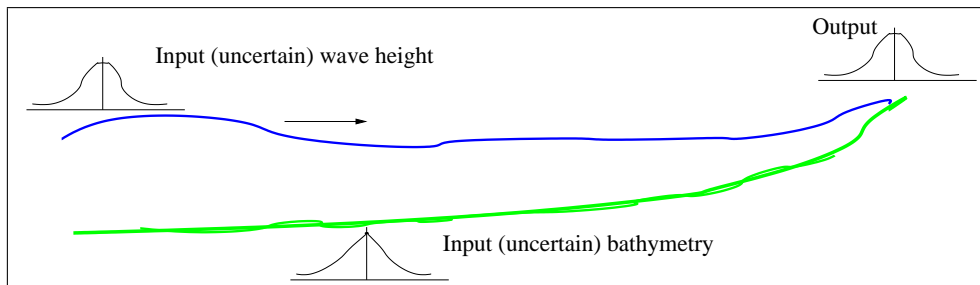


Figure 3: Schematic of sensitivity test method 2

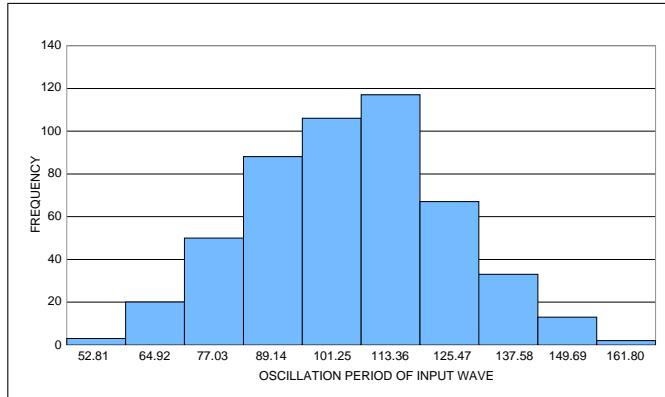


Figure 4: Distribution of input wave periods for the Monte-Carlo simulation

seafloor disturbance). This outcome aligns with the results from the previous section in that the period of the bottom oscillation had minimal effect on the outputs.

Time did not permit a comparison of the normalised variance of the input and output and it is recommended that this be considered in future work. Additionally, further investigation is required to determine the nature of the peaks and whether the bi-modality persists for more simulations. The random selection of the wavelength from a normal distribution will select values close to the mean and the small standard deviation selected here may be a result of the high peaks seen in Figure 5. Future work could investigate stratified sampling that also allows the consideration of extreme values. Further work should also incorporate an investigation of the grid resolution to determine whether this has affected the asymmetry in the plots shown in Figure 5 and additionally separate the results into more than ten bins.

This approach is computationally slower in comparison to the one described in section 3.1. Further tests investigating the response to an input distribution of initial wave amplitude, bottom slope, oscillation etc. should be a good comparison with the first sensitivity analysis and should be able to confirm or disprove the inferences of that test.

3.3 Other Models

There is a large body of work on the shallow water equations that could be studied to better understand the situation under consideration. For example, [3] used a transformation to compute the exact solution to the one-dimensional case for flow up a linear slope, while [4] and [16] considered runup over variable topography. [14] found a semi-analytic solution using a series method, again for a linear bottom slope, while [8] computed solutions with a series of combined linear segments for the bottom slope. Other numerical models have been used to assess errors and compare with experimental and field data. For example, [5] showed that errors in the cross-shore boundary conditions dissipated in the wave-breaking zone near to the beach and recommended that an accurate model needed to be applied over a length scale of around 10 times the width of this zone.

All of this earlier work shows clearly that the numerical models using the shallow water equations (or in some cases the Boussinesq approximation) provide good estimates not only of runup but also wave shape, e.g. (field) [17] or [14] (experimental).

The analytical solutions could be used to assess the effect of errors in some of the factors

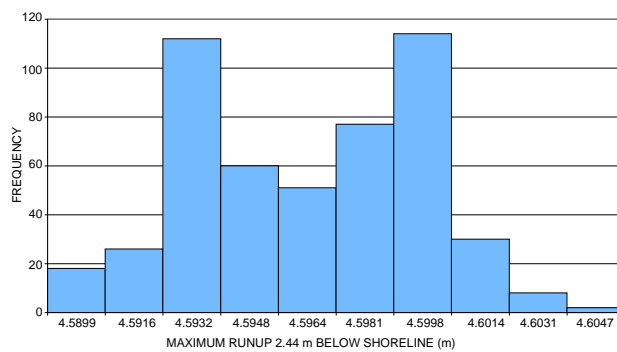
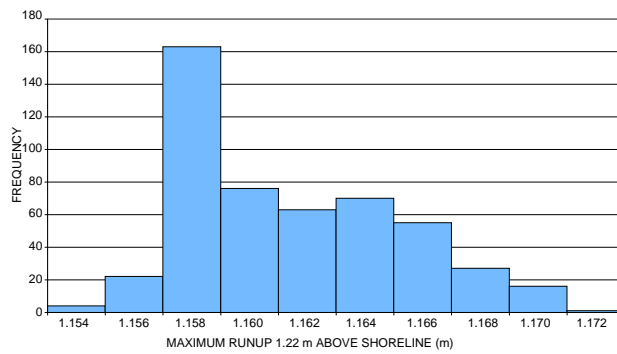
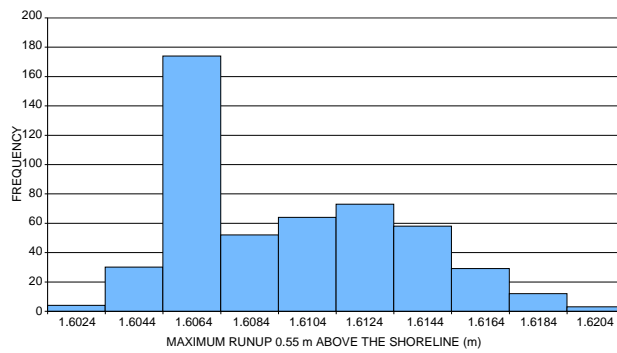
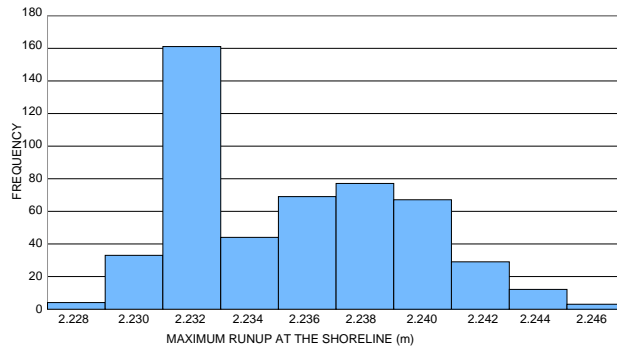


Figure 5: Frequency distribution of maximum water level at the 4 locations; (a) at the usual shoreline, (b) 0.55m above (c) 1.22m above (d) 2.44m below the usual shoreline.

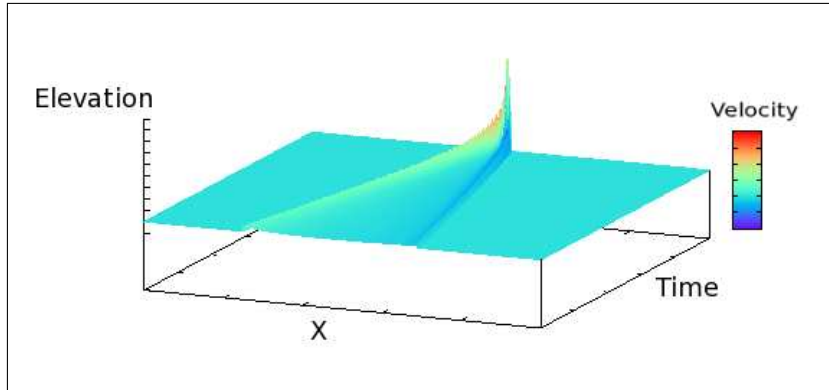


Figure 6: The time evolution of a tsunami wave with no initial velocity using [7]. Time is moving toward the reader. Colours indicate magnitude of water velocity. The vertical scale is greatly exaggerated.

in which we are interested, while there also exist simple versions of one dimensional solvers for the shallow water equations that could be used in a similar manner to obtain fast and accurate sensitivity results, e.g. `clawpack` [2] or the more specific `tsunamiclaw`, [6]. Alternatively, a much more detailed model, such as that of [7], which solves the two dimensional Navier-Stokes equations (through a vertical slice running onshore) with a Smagorinsky model of turbulence, could be used. During the MISG, some simulations were performed with both `clawpack` and the model of [7] to compare with the sensitivity analyses using ANUGA, with encouraging results. A typical simulation using this latter model is given in Figure 6.

The model `clawpack` was used to perform some preliminary tests to consider the variation in inundation as several of the major input parameters were altered. The case considered was a single, linear slope (with only one segment this time) in which the bottom slope was $S_B = 1/50$, the amplitude of the incoming wave was half of the bottom depth at the outer limit, and no bottom friction was included (so it is a worst case scenario). Tsunami amplitudes in the open water do not have this characteristic but can occur once the tsunami shoals in the nearshore environment. As before, this value was selected for testing purposes only. The effect of incoming wave amplitude, incoming wavelength and bottom slope can be seen in Figure 7. Given that this model is based on the same equations as ANUGA, the relationship would be the same. Clearly as the incoming wave amplitude or wavelength increases, the inundation level increases, and at a similar rate. This is to be expected because in both cases there is an increase in the mass of water in the wave. However, it does mean that the wavelength needs to be incorporated into the sensitivity simulations. The effect of increasing bottom slope is to cause a decrease in inundation, but this is also to be expected since more energy is required to push the water up the slope. These simulations do show how this model or even a semi-analytic model could be used to investigate the parameter space without having to set up simulations using the full ANUGA model.

3.4 Omissions

The MISG work group was unable to consider several aspects of the problem that were originally considered of interest. In particular, we did not consider the sampling required to

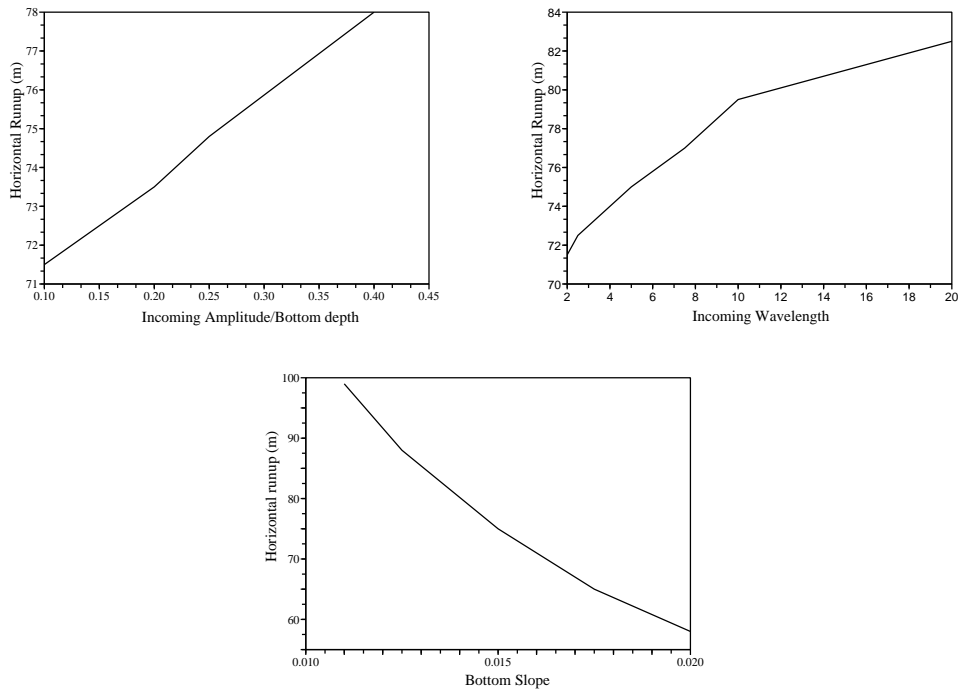


Figure 7: Simulations performed using `clawpack`, showing change in runup while varying (a) incoming amplitude, (b) wavelength and (c) bottom slope

correctly resolve the bottom topography sufficiently given the desired accuracy of the model. This requires further research and statistical input. The sampling required to adequately resolve the bottom of an uncharted bay does indeed depend on the variation in depth of the bay itself. There is no point in measuring on a scale smaller than the resolution of the model. In fact, if the test results above are replicated over a wide range of scenarios, it may not be necessary to have particularly accurate topographical resolution, as the main source of error is in the incoming wave. It seems likely that except for large vertical obstacles, unless the variation is of an order significant compared to the wavelength of the incoming wave, it is likely to have little impact. However, the location and movement of sandbars may cause significant variations in the topography, and their effect is under consideration for future work.

4 Outcomes and further work

The main outcome of the MISG workshop was the methodology to investigate the sensitivity of the tsunami inundation model to a range of inputs. That is, the variation in the model output can be determined by calculating the first and second derivatives with respect to variations in inputs. This methodology can be implemented as part of Geoscience Australia's tsunami risk modelling program.

The results of the MISG week have pointed to several options for further investigation. Continuation of both the one dimensional and two dimensional sensitivity analyses at different

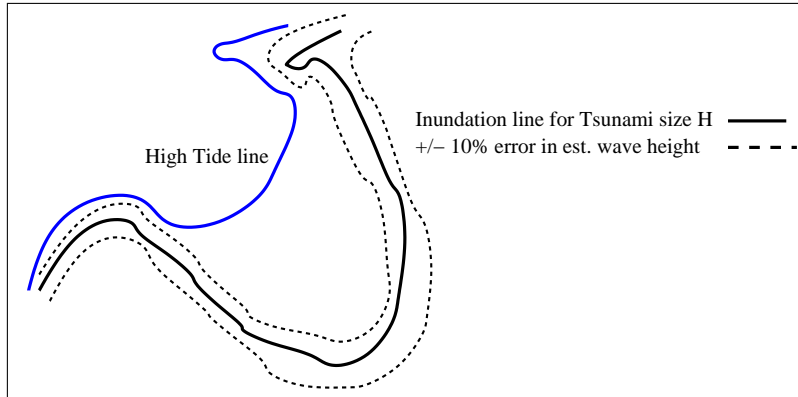


Figure 8: Schematic of what an inundation map with errors might look like.

locations in the parameter space is required to verify the initial findings. Inclusion of the sensitivity to the wavelength of the incoming wave also seems necessary and wavelengths appropriate to the shallow water wave equations must be selected (the wavelength used in this initial exercise is not valid in this context). This could be done by proceeding in a similar manner to that outlined above, or could be followed up using similar techniques in the analytic solutions, i.e. compute the Jacobian matrix analytically from the equations. Automatic differentiation techniques as described by [13] could also be investigated.

In addition, further work is required to understand how sudden bathymetric changes or focusing or reflections from islands or other coastal features affect runup calculations. The presence of seasonal movement of sandbars should also be considered as well as any focusing of the wave by the coastline. All of these tests, however, can be done using the simple one and two dimensional scenarios described above rather than full simulations. These idealised cases should be verified against full models when available. [1] have used ANUGA to study how tsunami run-up is affected by a range of coastal embayment types. Whilst they did not investigate sensitivity specifically, the results indicate that the bathymetry does play an important role in predicting tsunami impact. Continuation of studies similar to this will determine the parameters that lead to the greatest sensitivity. These studies will need to follow a probabilistic analysis approach whereby a range of scenarios are investigated.

Another conclusion of the MISG group is that *for simple cases*, the effect of relative errors in estimates of the amplitude of the tsunami are large in comparison to the effects of the other input errors, e.g. topographic errors. If the error in the input wave is understood then three simulations could be conducted to understand the sensitivity to the input wave only. The three simulations would be one with the given input wave and the remaining two with the input wave \pm the error as shown in Figure 8. In addition to understanding the sensitivity to the input wave, the simulations would highlight how the topography under consideration responds, i.e. is the topography inherently vulnerable to wave attack? This will lead to an increased understanding for what problems bathymetry and topography are important.

Conducting tsunami risk assessments in Australia will continue to rely on the validation of the tsunami risk modelling methodology. This process is ultimately linked to having a complete understanding of the likelihood and mechanisms of the tsunamigenic earthquake. This requires a program to understand the history of tsunami through palaeotsunami research both in Australia and within the region, as well as more improved rupture models. The

question remains on the required accuracy and spatial resolution of the supporting elevation data.

Acknowledgements

The moderators would like to thank the industry representative, Jane Sexton, from Geoscience Australia, and the others who contributed to the discussions and work on this problem; Simon Clarke, Dian Georgiev, Songping Zhu, Melanie Roberts, Steve Roberts, Lewis Mitchell, Kate Snow, Fatimah Noor Harun and John Cogill.

References

- [1] Baldcok, T.E., Barnes, M.P., Guard, P.A., Hie, T., Hanslow, D., Ranasinghe, R., Gray, D. & Nielsen, O. (2007) Modelling tsunami inundation on coastlines with characteristic form, 16th Australasian Fluid Mechanics Conference, 2-7 December, 2007, Australia.
- [2] Berger, M.J. & LeVeque, R.J. (1998) Adaptive Mesh Refinement Using Wave Propagation Algorithms for Hyperbolic Systems, *SIAM J. Numer. Anal.* **35**, 2298-2316.
- [3] Carrier, G.F. & Greenspan, H.P. (1958) Water waves of finite amplitude on a sloping beach, *J. Fluid Mech.*, **4**, 97-109.
- [4] Carrier, G.F. (1966) Gravity waves on water of finite depth, *J. Fluid Mech.*, **24**, 641-659.
- [5] Chen, Q. & Svendsen, A. (2003) Effects of cross-shore boundary conditions errors in nearshore circulation modelling, *Coastal Engng.*, **48**, 243-256.
- [6] George, D.L. (2006) *Finite Volume Methods and Adaptive Refinement for Tsunami Propagation and Inundation*, PhD Thesis, University of Washington, see <http://www.math.utah.edu/~george/tsunamiclaw.html>
- [7] Georgiev, D., Roberts, A.J. & Strunin, D. (2007) The dynamics of the vertical structure of turbulence in flood flows, *ANZIAM J.*, **48**, C573-C590.
- [8] Kânoğlu, U. & Synolakis, C.E. (1998) Long wave runup on piecewise linear topographies, *J. Fluid Mech.*, **374**, 1-28.
- [9] Lynett, P.J., Wu, T-R. & Liu, P.L-F. (2002) Modeling wave runup with depth-integrated equations, *Coastal Engng.*, **46**, 89-107.
- [10] Nielsen, O., Roberts, S., Gray, D., McPherson, A. & Hitchman, A. (2005), Hydrodynamic modelling of coastal inundation, *MODSIM 2005, Int. Cong. Modelling and Simulation, Modelling and Simulation Soc. of Australia and NZ*, 518-523.
- [11] Pelinovsky, E., Troshina, E., Golinko, V. & Petrukhin, N. (1999) Runup of tsunami waves on a vertical wall in a basin of complex topography, *Phys. Chem Earth (B)*, **24**, 431-436.
- [12] Saltelli, A., Chan K. & Scott E.M., Eds, (2000), *Sensitivity Analysis*, John Wiley and Sons Ltd., West Sussex, England.

- [13] Sambridge, M., Rickwood, P., Rawlinson, N. & Sommacal, S. (2007) Automatic differentiation in geophysical inverse problems, *Geophys. J. Int.*, **170**, 1-8.
- [14] Synolakis, C.E. (1987) The runup of solitary waves, *J. Fluid Mech.*, **185**, 523-545.
- [15] Tadepalli, S. & Synolakis, C.E. (1994), The run-up of N-waves on sloping beaches, *Proceedings: Mathematical and Physical Sciences*, **445**, 1923, 99-112.
- [16] Tuck, E.O. & Hwang, L. (1972) Long wave generation on a sloping beach, *J. Fluid Mech.*, **51**, 449-461.
- [17] Zahibo, N., Pelinovsky, E., Talipova, T., Kozelkov, A. & Kurkin, A. (2006), Analytical and numerical study of nonlinear effects at tsunami modelling, *Appl. Maths & Computation*, **174**, 795-809.

Annealing steel coils

Mark McGuinness

Victoria University of Wellington

Winston Sweatman

Massey University

Duangkamon Baowan

University of Wollongong

Steve Barry

University of New South Wales @ADFA

Abstract

Cold rolled steel in the form of coiled sheets requires heat treatment (annealing) in order to release stresses and reform the crystalline structure. During this process the whole coil must be heated to the required temperature and then maintained at this temperature for a period of time. At New Zealand Steel the process takes place inside a batch annealing furnace. The MISG group considered the problem of where the cold point lies within the steel coils, i.e. what is the last part of the coil to reach the required temperature, and how long does it take to reach this temperature? Challenges include deciding what the boundary conditions are on a coil, and dealing with the nonlinearity and anisotropy caused by height-dependent gaps within coils.

1 Introduction

During steel manufacture, the process of cold rolling introduces stresses due to changes in the crystalline structure of the metal. These stresses are released by further heat treatment (annealing) which reforms the crystalline structure and reintroduces desirable mechanical properties. The steel for this stage is in the form of a coil. This coil has been produced by wrapping a long steel sheet about an armature, which is then removed, leaving a curved inner surface. The entire steel coil has to be raised to a specified temperature within a *Uniflow Annealing System* (UAS) furnace. The steel coil is then maintained at this temperature for a period of time to achieve annealing.

New Zealand Steel have a number of empirical formulae that they use to decide how long to keep a set of coils in the furnace, to ensure the thermal centre of each coil reaches the desired temperature. These formulae were derived from data generated during commissioning of the furnace, and subsequently lost. The formulae have also been modified over the years, and the original formulae are no longer available.

The following are the objectives identified by the industry representatives:

1. Determine the cold point in a single cold rolled annealed coil taking into account radial and axial heat transfer.

2. Develop new heating formulas based on coil weight, width and thickness if appropriate.
3. Evaluate heating time variation with coil position in the furnace.

During the week some progress was made on addressing both of the first two objectives. The third (extra) objective was also the subject of discussion. A challenging feature of modelling this process remains the practical difficulties encountered in taking experimental measurements within the furnace.

To begin to address the issues, the heat transfer from the furnace through the steel coils must be modelled. We desire to determine the internal point within each coil that takes the longest time to reach the required temperature, and to find how much time is necessary for that to occur. Two parts to the problem can be identified. One is to establish the boundary conditions at the exterior of the steel coils and the other is to model the internal conduction within the steel coils. In both these areas information and insight were provided to the MISG group by the industry representatives and from the literature.

2 Conditions within the UAS furnace

For the New Zealand Steel annealing process, batches of steel coils are placed upon a ventilated steel platform in a single layer on their circular ends (see Figure 1). The ventilation consists of vertical holes that pass completely through the platform. Typically there are nine coils in a square formation on the platform. Each coil weighs between ten and twenty tonnes, is 700 to 1500mm high (this is the width of the steel strip before being coiled), and the steel strips are from 0.4 to 3mm thick.

The ventilated platform is transported through the front door of the furnace to initiate the heating process. After annealing is complete the platform exits at the back of the furnace into another chamber. The furnace is filled with heated gas, an inert mixture of nitrogen (93% by volume) and hydrogen. This is circulated around the coils. Heating is by radiant burners in the ceiling and on the sides of the furnace. The burners at the sides are shrouded so that they do not radiatively heat the coils, but they do heat the gas. The burners in the ceiling are almost uniformly spread over the set of nine coils.

It is difficult to determine exact boundary conditions for the steel coils. There is limited experimental data available and the gathering of such data is difficult. One measurement that has been recorded is the temperature at two points in the furnace: one in contact with the top surface of one of the steel coils and the other directly above this position and within the heated gas. An example of this data is shown in Figure 2.

Considering an individual steel coil, heat transfer is achieved by a mixture of direct radiation from the heaters in the ceiling of the furnace, conduction from the ventilated steel platform below the coils, and convection by the inert gas (nitrogen/hydrogen mixture) which is blown over heaters and around the coils inside the furnace. The measurements in Figure 2 indicate that the temperature on the circular top of the coil is very close to that of the neighbouring gas. This is likely due to rapid direct radiative heating of the top of the coil by the heaters in the ceiling. As a consequence, the upper boundary is here assumed to have a temperature that matches the furnace gas temperature. The circular base of the coil is assigned this temperature too, as the ventilated steel platform with its relatively large surface area is anticipated to heat very rapidly to the gas temperature, and then conduct heat directly into the lower end of each coil. Heating on the curved inner and outer surfaces of a



Figure 1: Photographs of steel coils being prepared for and entering the UAS furnace. (Photographs courtesy of NZ Steel.)

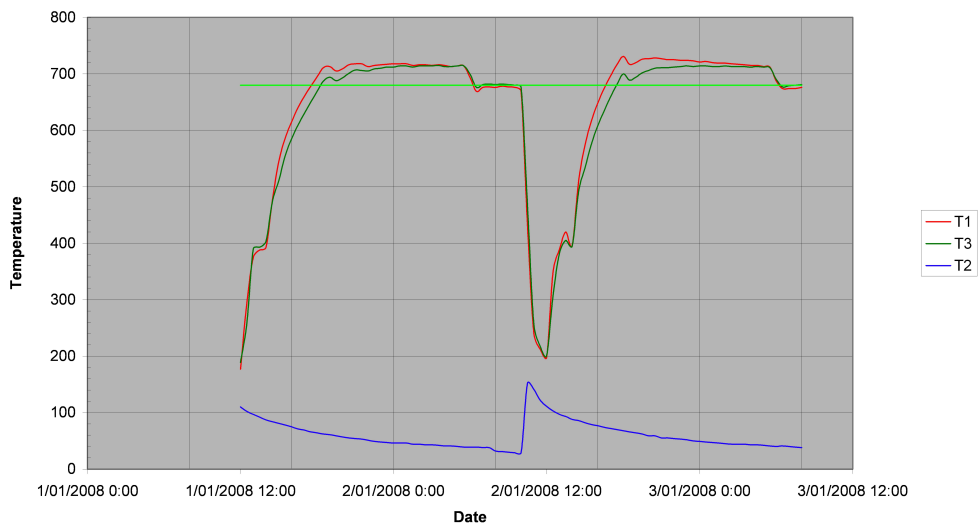


Figure 2: Temperature measurements ($^{\circ}\text{C}$) taken inside a UAS furnace during just under two heating cycles. The uppermost curve (T1) is the gas temperature above a set of coils, and the curve just below (T3) is the temperature of the upper outer edge of a coil. The target temperature of 680°C is also shown. The lowest line (T2) is the gas temperature in the chamber that the coils are cooled down in following annealing. (Figure courtesy of NZ Steel.)

coil is by convection from the surrounding gas and so the boundary condition here is that of Newton's Law of Cooling.

3 Heat transport within the coils

Superficially, each steel coil can be considered to be a hollow cylinder, annular in cross-section. However, as the coils are rolls of sheets of steel, there are gaps in the radial direction between the neighbouring parts of the steel sheet. As the gas in these gaps has a lower conductivity than steel, the effective conductivity of the coil in the radial direction is lower than that in the vertical direction (within the steel sheet). As a first approximation, the gap between the sheets is assumed to be constant. However, in practice, due to the non-uniformity of the rolling process, the steel sheet has a crown; that is it is thicker in the middle of the sheet than at the edges. This means that the radial gap varies in width vertically along the coil, being larger at the top and bottom ends of the coil, and smaller halfway up, where it is primarily due to surface roughness that there is a gap present. In principle, the thermal conductivity in the radial direction also varies with coil tension and differential heat expansion of the coils due to temperature gradients, and so is dependent on radial position as well as vertical position. When there is contact between the radial steel layers, heat transport could occur through steel-steel contact [6], by diffusion through the gas in the gap, and by radiation across the gap. However, to a reasonable extent, a rough contact surface can still be treated as if it were effectively a small uniform width gap [10, 9].

Therefore, since the number of windings in each one is large, we model a coil as a uniform hollow cylinder with radial conductivity dependent on position:

$$\frac{\partial(c_p\rho T)}{\partial t} = \frac{1}{r} \frac{\partial}{\partial r} \left(k_r r \frac{\partial T}{\partial r} \right) + \frac{\partial}{\partial z} \left(k_z \frac{\partial T}{\partial z} \right), \quad (1)$$

where T [K] is the temperature, c_p [J/kg/K] is the heat capacity which is a function of temperature, ρ [kg/m³] is the density of the steel, $k_r(z)$ [J/m/s/K] is the radial conductivity, and k_z [J/m/s/K] is the vertical conductivity which is assumed to be the constant conductivity of steel, k_s .

The relevant dimensions and properties are listed in Table 1.

3.1 Radial Conductivity — Modelling the Gaps

In some of the literature [7, 8], the coils are modelled as a concentric series of separate annular cylinders of metal with hot gas between, as illustrated in Figure 3. Then variations in the radial gaps due to crowning (varying strip thickness) and due to temperature gradients inducing differential expansions are calculated [7, 8].

Using the data provided by New Zealand Steel, the geometry is sketched in Figure 4, where lengths, a , b , and d are indicated. Here we use z' to represent the vertical distance from the centre of the coil or equivalently the distance from the centre of the steel sheet towards its edges. The sheets are of a fairly constant thickness at their centre but taper towards the edges. Near the edges, that is the top or base of the coil, the effective radial thermal conductivity is given by

$$k_{\text{eff}} \approx \frac{a + b}{\frac{a}{k_s} + \frac{b}{k_g}}, \quad 419.74 \leq z' \leq 550. \quad (2)$$

steel density	ρ	7854	kg/m ³ (at 300k)
steel thermal conductivity	k_s	60.5	W/m/K at 300K
		56.7	W/m/K at 400K
		48	W/m/K at 600K
		39.2	W/m/K at 800K
		30	W/m/K at 1000K
steel thermal capacity	c_p	434	J/kg/K at 300K
		487	J/kg/K at 400K
		559	J/kg/K at 600K
		685	J/kg/K at 800K
		1169	J/kg/K at 1000K
gas thermal conductivity	k_g	0.06	W/m/K
furnace circulation		800	m ³ /minute
steel strip thickness		0.4–3	mm
steel strip width		700–1500	mm
coil mass		10–20	tonnes
coil inner diameter		508	mm
coil outer diameter		1.5	m
platform mass		37	tonnes
furnace dimensions		$6.5 \times 6.5 \times 4$	m ³

Table 1: Table of steel and coil properties.

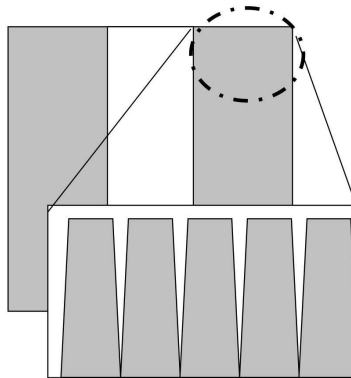


Figure 3: A sketch of the cross section of a coil, with the close up showing how variation in strip thickness causes a variation with height in the gas gap within the coil.

This expression for effective conductivity is only exact for the steady state and the limit of infinite layers [5]. In this z' range,

$$a + b = d, \quad b = s(z' - 418.42), \quad (3)$$

where measurements indicate that the slope s is 0.038/50. In the central contact region between the two sheets a $1\mu\text{m}$ gap (an effective gap due to roughness) gives

$$k_{\text{eff}} \approx \frac{d}{10^{-6}/k_g + (d - 10^{-6})/k_s}, \quad z' \leq 419.74. \quad (4)$$

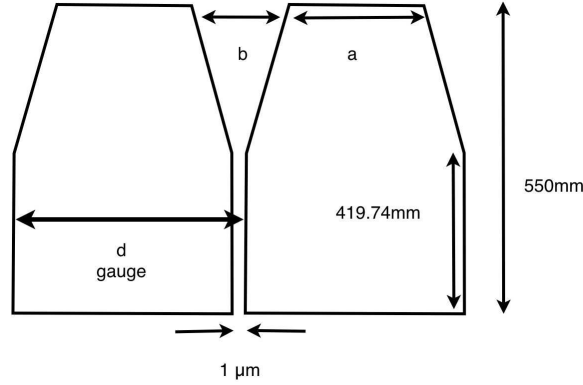


Figure 4: A sketch showing the geometry of the hot gas gap between two sheets of steel in a coil. The sketch shows the upper half of a cross-section through two 1.1m wide sheets.

Using these equations, the effective radial thermal conductivity is in the range 14–25 W/m/K when d is in the range 0.4–3 mm. These thermal conductivities are plotted in Figure 5. Note that these radial thermal conductivities are smaller than the vertical thermal conductivity, $k_s = 30$ W/m/K at 1000K.

If we consider just radial conduction, then the results in Figure 5 indicate that crowning effectively causes an overall reduction in k_r because of the very low radial conduction at the top and bottom of the coils. However, in practice, these ends are heated rapidly by vertical conduction.

3.2 Estimates of heating times

The timescale for heating is

$$t = \frac{\ell^2 \rho c_p}{k}, \quad (5)$$

where ℓ is the lengthscale, and k is the appropriate (effective) thermal conductivity. This formula assumes that the surface of the steel is immediately raised to the target temperature. So an approximate estimate of the time to heat a coil of steel, if there is only axial (vertical) heating, is

$$t = 10\text{--}50 \text{ hours} \quad (6)$$

for $\ell = 350\text{--}750\text{mm}$ (half the height of a coil) and using $k = k_s$. A solution of the heat equation in the vertical direction with upper and lower surfaces fixed at T_{gas} obtained using Maple, is shown in Figure 6.

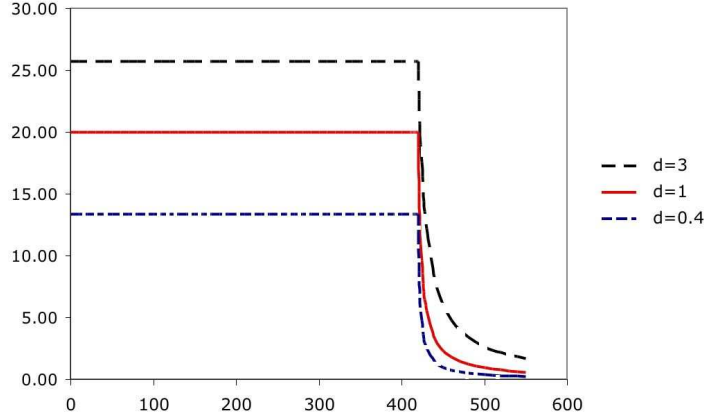


Figure 5: Effective radial thermal conductivities (W/m/K) resulting from the geometry sketched in Figure 4, plotted against vertical distance from the middle of a coil z' (mm), for gauges $d = 0.4, 1,$ and 3 mm, and for a temperature of 1000K .

If we consider heating purely in the radial direction, near the centre of the coil, so that $\ell = 250\text{mm}$, then the corresponding timescales are

$$\begin{aligned}
 t &= 12 \text{ hours,} & \text{when } d &= 0.4 \text{ mm} \\
 t &= 8 \text{ hours,} & \text{when } d &= 1 \text{ mm} \\
 t &= 6 \text{ hours,} & \text{when } d &= 3 \text{ mm} .
 \end{aligned} \tag{7}$$

However, this does not take into account the restrictive effect of Newton heating on the curved surfaces, discussed in detail in the next section.

3.2.1 Radial Boundary Condition

Radial heating is driven by conduction from the hot gas rather than by direct radiant heating from the furnace burners. This means that the heating times above need to be reconsidered in light of the heat transfer coefficient H . When they are at temperature T , the heat flux into the (inner and outer) curved surfaces of the coils is

$$Q_c = H(T_{\text{gas}} - T) , \tag{8}$$

where

$$H = \frac{\text{Nu } k_g}{D} \tag{9}$$

and Nu is the Nusselt number (the ratio between actual — convective — heat transfer and that which would be achieved with only conductive processes at work in the hot gas), and D is the hydraulic diameter of the region the hot gas is flowing through. A number of semi-empirical formulae exist for Nu in the case of forced convection, in terms of the Reynolds number Re ($\approx 2.7 \times 10^4$ for the UAS furnace) and the Prandtl number $\text{Pr} \approx 0.7$, including the laminar flow case:

$$\text{Nu} = 0.648\sqrt{\text{Re}} (\text{Pr})^{\frac{1}{3}} , \tag{10}$$

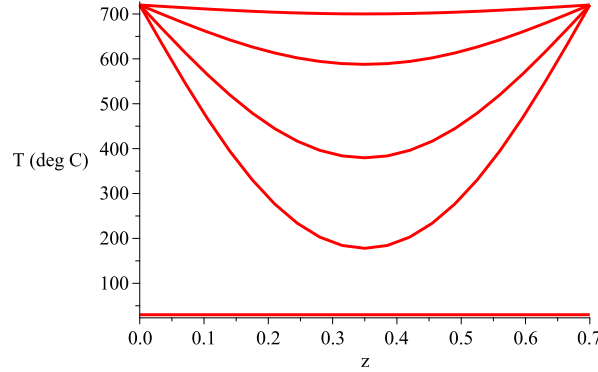


Figure 6: Solutions calculated by Maple to the axial (vertical) heating problem, using $k_s = 30$ W/m/K, $c_p = 1169$ J/kg/K, $T = 720^\circ\text{C}$ top and bottom, and initial temperature 30°C . The different curves show temperatures ($^\circ\text{C}$) at 0, 2, 4, 8 and 16 hours plotted against vertical distance z (m) from the bottom of the steel coil: the lowest curve is the temperature in the coil at time zero; the uppermost curve is the temperature in the coil after 16 hours of heating when this temperature is everywhere close to 720°C .

and, in the turbulent flow case, the Dittus-Boelter formula

$$\text{Nu} = 0.023\text{Re}^{0.8}\text{Pr}^{0.3} , \quad (11)$$

and the Gnielinski formula

$$\text{Nu} = \frac{0.037\text{Re}^{0.8}}{1 + 2.443\text{Re}^{-0.1}(\text{Pr}^{2/3} - 1)} . \quad (12)$$

All of these formulae give values for H in the range 3–5.

The question addressed here is whether the rate of heat transfer from the hot gas is the main limitation, or the rate at which heat is conducted radially into the steel coil from its surface. The Biot number helps answer this, since it is the ratio of the heat transfer rate at the surface to the heat transfer rate inside the coil:

$$\text{Bi} = \frac{H\ell}{k_s} \approx 0.1 . \quad (13)$$

This value being much less than 1 indicates that the rate-limiting factor for radial heat transfer, is heat transfer from the hot gas to the surface of the coil, rather than within the coil. This calculation is supported by numerical solutions to the radial heat equation using Maple, illustrated in Figure 7. In this figure, the internal temperatures stabilise much faster than the overall temperature rises.

The exact details of how the radial thermal conductivity varies with height and with temperature gradients are of less importance than the details of the heat transfer process, across a thermal boundary layer in the hot gas, into the curved vertical surfaces of a coil. Heat transfer in the vertical direction is much more rapid, despite the longer distances involved, because radiation from above and the ventilated platform from below are far more effective at heating the horizontal surfaces.

Furthermore, discussion with the industry representatives suggested that the tensions and roughness of the actual coils would tend to reduce the variations with temperature gradient.

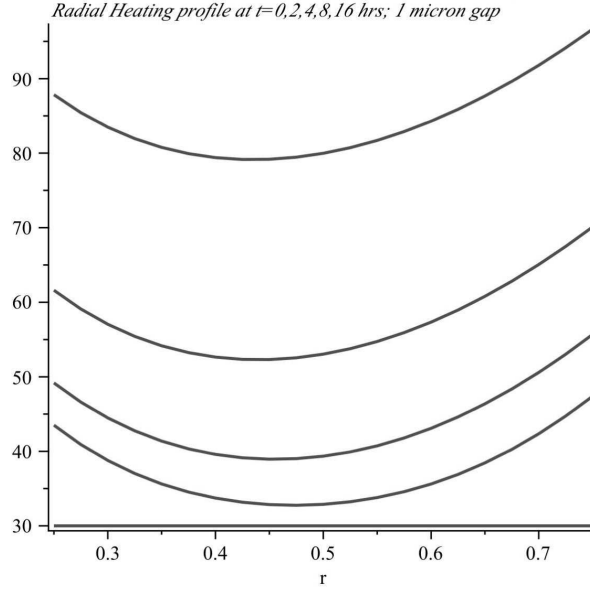


Figure 7: Solutions calculated by Maple to the radial heating problem, using $H = 5$ in the flux boundary condition, $k_s = 20$ W/m/K, $c_p = 1169$ J/kg/K, $T_{\text{gas}} = 720^\circ\text{C}$, and initial temperature 30°C . Temperature ($^\circ\text{C}$) is plotted against radial distance (m) from the centre of the annulus that is the cross-section of the steel coil. Time zero is the lowest curve; 16 hours of heating is the uppermost curve. Note the relatively slow rise in boundary temperatures. Also note that the coldest point is nearer the inner face of the coil, due to its smaller surface area (hence smaller heat flux).

Hence we now consider a model in which the horizontal cross-section of the coil is effectively concentric annuli of metal and gas that remain constant in size.

4 Linear heat transfer — analytic solutions

In this section we find analytic solutions for linear heat transport within a cylindrical shell. This allows us to consider both radial and axial heat flow simultaneously.

We assume that the coil is a homogeneous region, although with anisotropic heat conductance, so that k_r and k_z are constant. The coordinate system is shown in Figure 8. The solution takes the form of a series whose leading order behaviour is governed by a dominant eigenfunction.

In the linear model, (1) is written in the simpler form

$$\frac{\partial T}{\partial t} = D_r \frac{1}{r} \frac{\partial}{\partial r} \left(r \frac{\partial T}{\partial r} \right) + D_z \frac{\partial}{\partial z} \left(\frac{\partial T}{\partial z} \right). \quad (14)$$

Our boundary and initial conditions are

$$k_r \frac{\partial T}{\partial r} = H(T - T_g), \quad \text{at } r = a, \quad (15)$$

$$k_r \frac{\partial T}{\partial r} = -H(T - T_g), \quad \text{at } r = b, \quad (16)$$

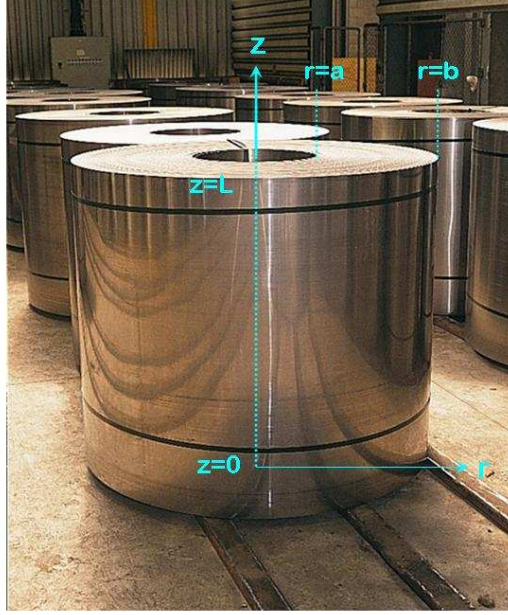


Figure 8: The coordinate system of a coil of height $z = L$ and radius $r \in [a, b]$. (Photograph courtesy of NZ Steel.)

$$T(r, z = 0, t) = T(r, z = L, t) = T_g, \quad (17)$$

$$T(r, z, t = 0) = T_0, \quad (18)$$

where $D_r = k_r/(\rho c_p)$, $D_z = k_z/(\rho c_p)$ are assumed constants, T_g is the external gas temperature, and T_0 the initial temperature of the coil. These equations are scaled using typical values, $t = t_0, r = b, z = L, T = T_g$:

$$t = t_0 t^*, \quad r = b r^*, \quad z = L z^*, \quad u = \frac{T - T_g}{T_0 - T_g}, \quad (19)$$

where r^*, z^*, t^*, u are the non-dimensional variables. There is a choice of two obvious time scales t_0 , using either D_r or D_z . For the problem of interest it is not clear which is dominant and they are of similar magnitude. Hence, without loss of generality we take

$$t_0 = \frac{L^2}{D_z}.$$

The linearised, non-dimensional system is thus

$$\frac{\partial u}{\partial t} = D \frac{1}{r} \frac{\partial}{\partial r} \left(r \frac{\partial u}{\partial r} \right) + \frac{\partial^2 u}{\partial z^2}, \quad (20)$$

$$\frac{\partial u}{\partial r} = +hu, \quad \text{at } r = a, \quad (21)$$

$$\frac{\partial u}{\partial r} = -hu, \quad \text{at } r = b, \quad (22)$$

$$u(r, z = 0, t) = u(r, z = 1, t) = 0, \quad (23)$$

$$u(r, z, t = 0) = 1, \quad (24)$$

where the * notation has been dropped for convenience, $D = D_r L^2 / D_z b^2$ represents the relative diffusivity, $a \in [0, 1]$ (strictly a^*) is the ratio of original lengths a/b , and $h = Hb/k_r$. This equation now represents non-dimensional cooling of a unit cylinder from initial unit temperature to surrounding temperature zero.

The solution is found by separation and Sturm-Liouville theory. A similar solution for the purely radial case can be found, without derivation, in [3] (page 530). Setting

$$u(r, z, t) = R(r)Z(z)T(t) \quad (25)$$

gives

$$Z'' = \mu Z, \quad Z(0) = Z(1) = 0 \quad (26)$$

$$R'' + \frac{1}{r}R' = \omega R, \quad R'(a) = hR(a), \quad R'(1) = -hR(1) \quad (27)$$

$$T' = (D\omega + \mu)T, \quad (28)$$

where ω and μ are members of infinite sets of eigenvalues. The respective eigenfunction solutions are

$$Z = \sin n\pi z, \quad \mu = -(n\pi)^2, \quad n = 1, 2, \dots \quad (29)$$

$$R = C_0(\lambda r) \equiv J_0(\lambda r) + B Y_0(\lambda r), \quad \omega = -\lambda^2, \quad (30)$$

$$T = \exp(-(D\lambda^2 + (n\pi)^2)t), \quad (31)$$

where B is a constant, and J_0, Y_0 are zeroth order Bessel functions. The boundary conditions at $r = a$ and $r = 1$ give

$$-\lambda J_1(\lambda a) - B\lambda Y_1(\lambda a) - hJ_0(\lambda a) - hBY_0(\lambda a) = 0, \quad (32)$$

$$-\lambda J_1(\lambda) - B\lambda Y_1(\lambda) + hJ_0(\lambda) + hBY_0(\lambda) = 0. \quad (33)$$

These have a consistent solution for B when

$$\begin{vmatrix} \lambda J_1(\lambda a) + hJ_0(\lambda a) & \lambda Y_1(\lambda a) + hY_0(\lambda a) \\ -\lambda J_1(\lambda) + hJ_0(\lambda) & -\lambda Y_1(\lambda) + hY_0(\lambda) \end{vmatrix} = 0. \quad (34)$$

This characteristic equation can be solved numerically to find λ , as illustrated in Figure 9 for the case $a = 1/3$ and $h = 1$.

Using (25) the full solution is

$$u(r, z, t) = \sum_{n=1}^{\infty} \sum_{m=1}^{\infty} A_{mn} e^{-(D\lambda_m^2 + (n\pi)^2)t} \sin n\pi z C_0(\lambda_m r), \quad (35)$$

where from (33)

$$B = - \frac{hJ_0(\lambda) - \lambda J_1(\lambda)}{hY_0(\lambda) - \lambda Y_1(\lambda)}, \quad (36)$$

and A_{mn} are constants found by Sturm Liouville orthogonality as

$$A_{mn} = \frac{\int_0^1 \sin(n\pi z) dz}{\int_0^1 \sin^2(n\pi z) dz} \frac{\int_a^1 r C_0(\lambda_m r) dr}{\int_a^1 r C_0^2(\lambda_m r) dr}. \quad (37)$$

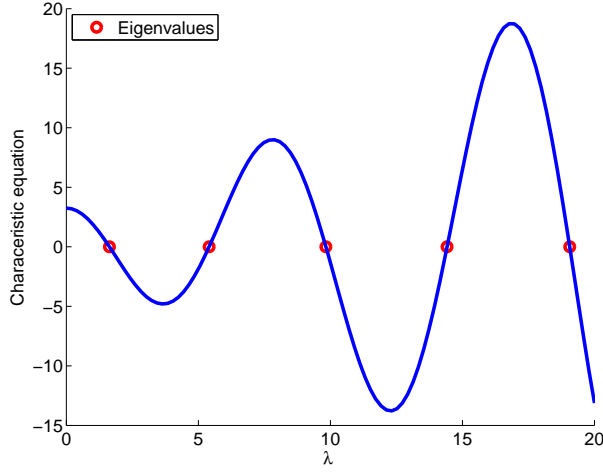


Figure 9: First five eigenvalues shown as zeros of equation (34) for $h = 1$ and $a = 1/3$.

These integrals can be evaluated to give

$$A_{mn} = 2 \frac{(1 - (-1)^n)}{n\pi} \frac{\left[\frac{r}{\lambda_m} C_1(\lambda_m r) \right]_a^1}{\left[\frac{r^2}{2} (C_0^2(\lambda_m r) + C_1^2(\lambda_m r)) \right]_a^1} \quad (38)$$

where C_0 and C_1 are given by (30). Use has been made of results from [1](chapters 9 and 11) summarised here using \mathcal{C}_ν and \mathcal{D}_ν to represent either J_ν or Y_ν :

$$\mathcal{C}'_0(x) = -\mathcal{C}_1(x) \quad (39)$$

$$\int_a^1 r \mathcal{C}_0(\lambda r) dr = \left[\frac{r}{\lambda} \mathcal{C}_1(\lambda r) \right]_a^1 \quad (40)$$

$$\int r \mathcal{C}_0(\lambda r) \mathcal{D}_0(\lambda r) dr = \frac{r^2}{2} (\mathcal{C}_0(\lambda r) \mathcal{D}_0(\lambda r) + \mathcal{C}_1(\lambda r) \mathcal{D}_1(\lambda r)). \quad (41)$$

The solution given by (35) can be evaluated to any degree of accuracy at any point using simple numerical summation. However, the dominant behaviour is given by the leading eigenvalues λ_1 and π . In Figure 9 the eigenvalues are shown as zeros of the characteristic equation (34) with $a = 1/3$ and $h = 1$. Numerically they can be shown to asymptote to being $3\pi/2$ apart.

Figure 10 shows the full solution $u(r, z = 0.5, t = 0.04)$ and the leading eigenfunction, equation (30) with $\lambda = \lambda_1$, using scaled values $h = 1$, $D = 1$, and $a = 1/3$. This illustrates that the leading eigenfunction dominates the solution and that the position of the cold point, $r = r_c$, can be given by finding the maximum of this eigenfunction. The time dependence is then governed by the time decay of the exponential term $\exp(-(D\lambda_1^2 + \pi^2)t)$.

Figure 11 shows the dependence of the cold point position and leading eigenvalue as a function of the scaled surface transfer coefficient h with $a = 1/3$, which is comparable to the practical application. Note that the cold point does not vary considerably with h . As h becomes small, the leading eigenvalue becomes small compared with π , the dominant

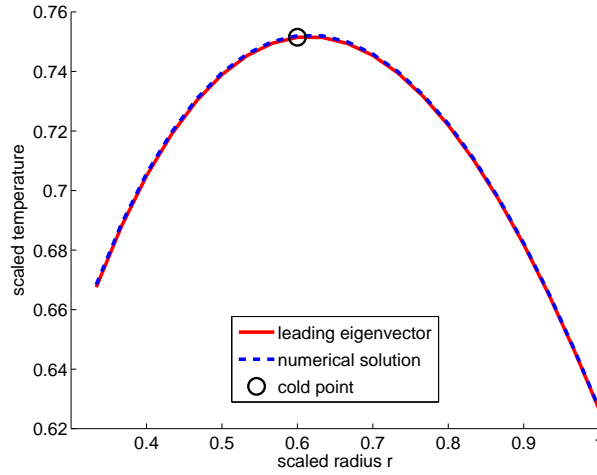


Figure 10: Comparison of full solution $u(r, z = 0.5, t = 0.04)$ and leading eigenfunction (30) for $h = 1$ and $a = 1/3$ with the cold point shown. Hence this eigenfunction is a good predictor of cold point position.

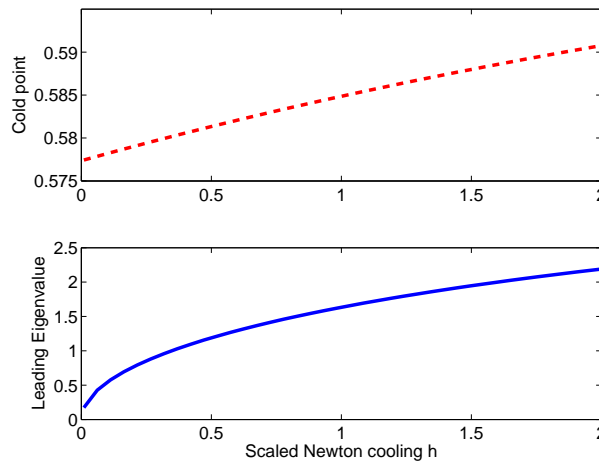


Figure 11: Dependence of the cold point position, $r = r_c$ and leading eigenvalue as functions of scaled surface transfer coefficient h with $a = 1/3$.

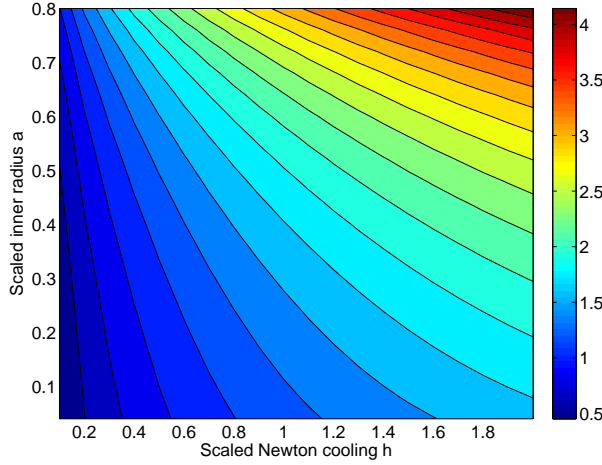


Figure 12: Contour plot showing the dependence of the leading eigenvalue as a function of scaled surface transfer coefficient h and scaled inner width a .

eigenvalue in the z direction; for small h the sides are effectively insulating and diffusion is dominated by the z dependence.

Figure 12 shows a contour plot of the leading eigenvalue as a function of the two parameters governing this variable, h and a . For this application it is unlikely that a will be varied, but this result is included for completeness.

4.1 Implications for heating times

The key feature of the dominant leading term in the solution (35) is the decay in time factor, which in dimensional terms is

$$e^{-\left(\lambda_1^2 \frac{D_r}{b^2} + \pi^2 \frac{D_z}{L^2}\right)t}. \quad (42)$$

The first part of the exponent is due to radial heating, the second part is due to axial heating. As noted previously, since the ratio

$$\frac{\lambda_1^2 D_r L^2}{\pi^2 D_z b^2} \quad (43)$$

is approximately 0.1 (using $\lambda_1 \approx 1$), radial heating is much slower than axial heating. However, the effects as evidenced by the exponential decay term above, are multiplicative. For example, increasing the convective transfer term H by a factor of 5 increases the eigenvalue λ_1 by a factor of 2, and this changes the heating time from a scaled value of 0.98 to 0.89, a 10% improvement.

For the cold point to reach the desired soak temperature of 680°C when gas temperature is 710°C and initial temperature is 30°C, the scaled solution u needs to change from the initial value of 1, to the value 30/680. If we ignore radial heating, this happens at the time

$$t = \frac{L^2}{\pi^2 D_z} |\ln(3/68)| \approx 0.32 \frac{L^2}{D_z} \approx 1.28 \frac{\ell^2}{D_z}. \quad (44)$$

This formula reduces by 10% if radial heating is included, to give

$$t \approx 1.15 \frac{\ell^2}{D_z}. \quad (45)$$

This is almost the same formula as that used in Section 3.2, and gives similar heating times. These results (44) and (45) were checked numerically by setting $u = u_c$ in (35) with $r = r_c$ and $z = 1/2$, where r_c is the cold point established from the leading eigenfunction (27).

5 Numerical solutions

In this section we explore numerical solutions to (1). For the steel coil application we assume that $k_r = k_r(z)$ so that the radial conductivity across the coil is height dependent. We further consider k_z to be constant, ρ to be constant and c_p to be temperature dependent. Using essentially the same non-dimensionalisation system as with the linear solution, with the timescale $t_0 = L^2/(k_z/\rho c_p(1))$, we can write the governing equation as

$$\frac{\partial u}{\partial t} = D_r^* \frac{1}{r} \frac{\partial}{\partial r} \left(r \frac{\partial u}{\partial r} \right) + D_z^* \frac{\partial^2 u}{\partial z^2} - (u + T_1) \frac{\partial \ln c_p}{\partial t} \quad (46)$$

with boundary and initial conditions the same as (21)-(24) and

$$D_r^*(z, u) = \frac{c_p(1)}{c_p(u)} \frac{k_r(z)}{k_z} \frac{L^2}{b^2}, \quad (47)$$

$$D_z^*(u) = \frac{c_p(1)}{c_p(u)}, \quad (48)$$

$$T_1 = \frac{T_g}{T_0 - T_g}. \quad (49)$$

The cumbersome nature of this equation is due to the height dependence $k_r = k_r(z)$ and temperature dependence $c_p = c_p(u)$. If this is relaxed so that k_r and c_p are constant then equation (20) is recovered exactly.

Using second order, central finite differences, the fully nonlinear version of (46) was solved numerically with MATLAB. These experimental results were compared with the analytic solution of Section 4 and found to be accurate for a range of parameter values. Tests for stability and invariance under differing space and time steps were successful.

The discretisation used can be illustrated by considering the numerical strategy specifically applied to (20), where c_p is assumed constant. If $u(i dr, j dz, k dt) \equiv u_{i,j}^k$ represents the temperature at discretized position and time then

$$u_{i,j}^{k+1} = u_{i,j}^k + dt \left[D \left(\frac{\partial^2 u}{\partial r^2} + \frac{1}{r} \frac{\partial u}{\partial r} \right) + \frac{\partial^2 u}{\partial z^2} \right], \quad (50)$$

$$\frac{\partial^2 u}{\partial z^2} = \frac{u_{i,j+1}^k - 2u_{i,j}^k + u_{i,j-1}^k}{dz^2}, \quad (51)$$

$$\frac{\partial^2 u}{\partial r^2} = \frac{u_{i+1,j}^k - 2u_{i,j}^k + u_{i-1,j}^k}{dr^2}, \quad (52)$$

$$\frac{\partial u}{\partial r} = \frac{u_{i+1,j}^k - u_{i-1,j}^k}{2dr}. \quad (53)$$

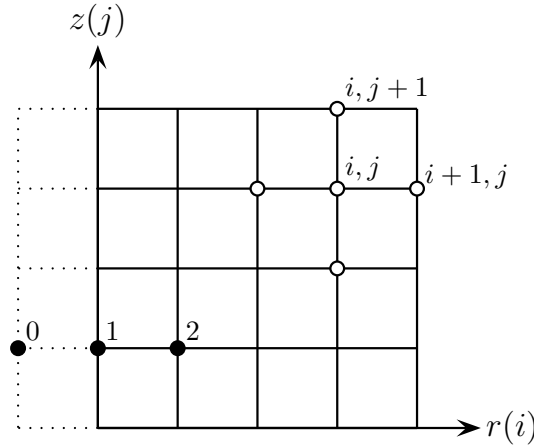


Figure 13: Finite differencing at a central point (i, j) and at a boundary point where a fictitious point is used.

The discretisation is shown in Figure 5. The boundaries $z = 0$ and $z = 1$ are easily defined by setting $u = 0$. On the boundaries $r = a$ and $r = 1$ we use a fictitious point outside of the region which is then eliminated by combining the discretisation above with the discretized boundary condition. Hence at $r = a$ we use the boundary condition (21), and the governing equation (20) and rearrange to find $u_{1,j}^k$:

$$\frac{u_{2,j}^k - u_{0,j}^k}{2dr} = hu_{1,j}^k, \quad (54)$$

$$u_{1,j}^{k+1} = u_{1,j}^k + dt \left[D \left(\frac{\partial^2 u}{\partial r^2} + \frac{1}{r} \frac{\partial u}{\partial r} \right) + \frac{\partial^2 u}{\partial z^2} \right], \quad (55)$$

with the $\frac{\partial^2 u}{\partial r^2}$ and $\frac{\partial u}{\partial r}$ terms involving $u_{1,j}^k$, $u_{2,j}^k$ and the fictitious point $u_{0,j}^k$. Using (54) to replace $u_{0,j}^k$ in (55) gives the new updated value for $u_{1,j}^{k+1}$. This is similarly applied at $r = 1$.

The numerical solution was found to be sufficiently accurate with a spatial discretisation of 21 points in both r and z directions — although a finer grid size of 41 points was necessary for small values of h . The time step was chosen to minimise computational time while remaining within the stability condition

$$dt < \frac{dx^2}{2D} \quad (56)$$

for all the typical length and diffusion scales in the problem. This numerical solution was also used to find estimates for how many terms are required in the numerical evaluation of the series in (35). As expected, for early times more terms are needed, although 10 terms is usually sufficient for accuracy. At later times, as the exponential term decays more rapidly, less terms are needed.

Figure 14 shows a contour plot of temperature in a cross section of the cylinder, with scaled $h = 0.3$, $t = 0.04$, $a = 1/3$, scaled diffusivity $D = 1/2$ and c_p a constant. These parameter values were chosen to represent realistic values for the coiled steel problem.

Figure 15 shows a cross section of the temperature at $r = 2/3$ with the same parameters as Figure 14. Radial diffusivity is likely to vary with height because of crowning: the uneven

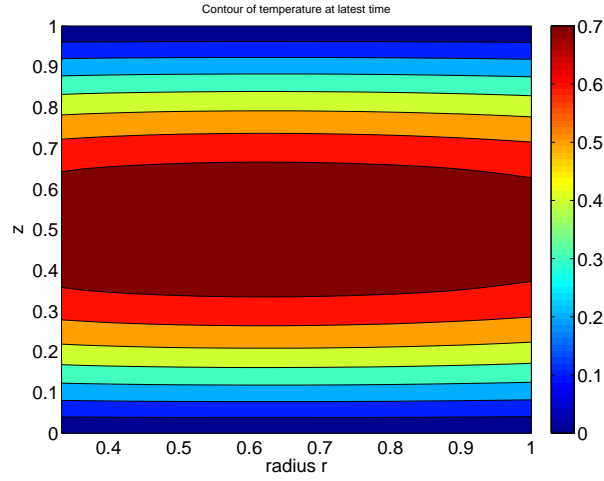


Figure 14: Contour plot of temperature in a cross section of the cylinder, with scaled $h = 0.3$, $t = 0.04$, $a = 1/3$ and scaled diffusivity $D = 1/2$.

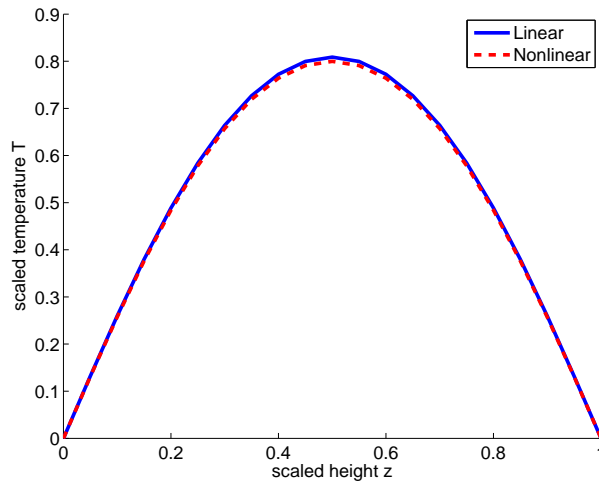


Figure 15: Scaled temperature at $r = 2/3$ versus height with the same parameters as Figure 14. This shows that for Newton cooling on the radial surfaces, varying radial diffusivity has little impact.

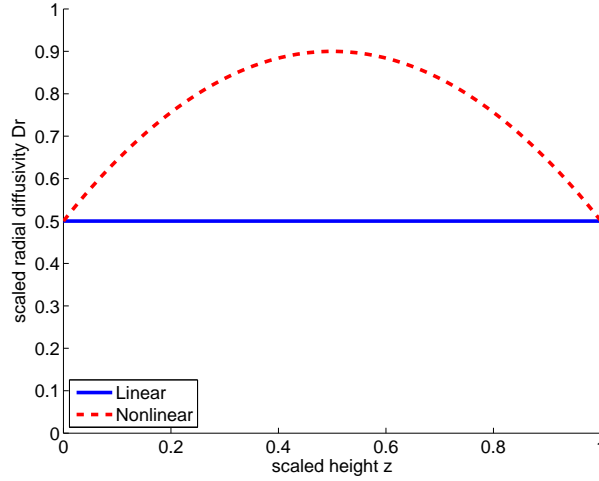


Figure 16: Variation of radial diffusivity with height used in Figure 15 .

thickness across the original cold rolled steel sheets. To investigate this effect, two different solutions are compared, one with the radial diffusivity constant and the other when it varies quadratically as shown on Figure 16. There is very little difference between the solutions. This is because the radial heat transport is so restricted by the surface heat transfer coefficient that heat is predominantly diffused vertically. This is also clear from Figure 14.

6 Variable Diffusivity

The diffusivities that have been used in previous sections to estimate heating times have been based on the properties of steel at 1000K. However, steel diffusivity varies with temperature, and is larger at smaller temperatures, so that we have overestimated heating times. The concept of mean action time [4] allows us to calculate by what factor we have overestimated heating time, by considering that the appropriate average diffusivity to take is

$$D_{\text{effective}} = \frac{\int_{T_0}^{T_g} D(T) dT}{T_g - T_0} . \quad (57)$$

Graphing tabled values of $D(T)$ and fitting a quadratic (using Maple) as illustrated in Figure 17 gives (for T in Kelvin)

$$D \approx 2 \times 10^{-5} - 2.5 \times 10^{-8}T + 4 \times 10^{-12}T^2 \text{ m}^2/\text{s} \quad (58)$$

and

$$D_{\text{effective}} \approx 1 \times 10^{-5} \text{ m}^2/\text{s} , \quad (59)$$

which is a factor of three larger than the value of D used at 1000K.

Hence our estimates of heating time are anticipated to be a factor of three too high.

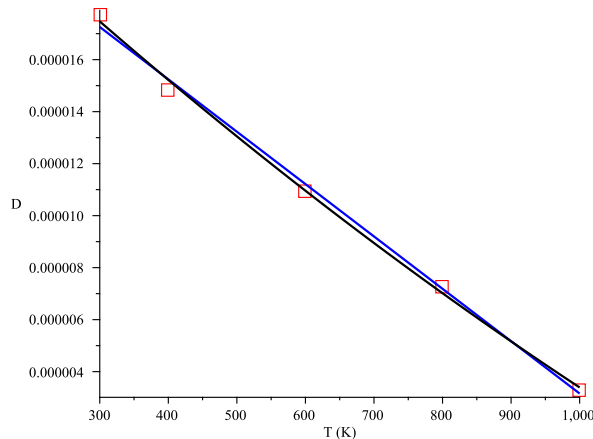


Figure 17: The dependence of diffusivity of steel (m^2/s) on temperature (K), data shown as boxes and a linear and a quadratic fit as curves.

7 Discussion and Conclusions

The analytical and numerical investigations of Sections 4 and 5 suggest that, with the boundary conditions chosen here, the main constriction on the heating of the steel coils is the slow transport of heat through the curved sides of the coils. Further analytical and numerical investigations with radiative heating of all the outer surfaces show a considerable reduction in the heating times [2].

It is difficult without further experimental data to assess the validity of our assumed boundary conditions. We have ignored the effect of the location of the coil in the furnace but industrial experience suggests that failure of the annealing process is associated with particular grid positions within the furnace. There will be further radiation within the furnace such as between the sides of the steel coils. The ceiling plan of the furnace also indicates that some parts of the circular top ends of the coils could be partially shielded from the radiation from above, which would break the cylindrical symmetry which we have assumed. Our modelling underscores the importance of radiative heat transport compared with convective transport.

In any case, our results indicate that the primary variable of concern is the vertical length-scale of the coils, and that considerations such as gauge are secondary, because the radial geometry is in practice independent of gauge, and because radial heat transport is much slower than vertical heat transport. This is because of the boundary conditions rather than the differences in thermal conductivity. Hence, grouping coils by strip width is key to having groups of coils that require the same annealing time in the same batch.

Acknowledgements

We are grateful to the industry representatives Phil Bagshaw, Andrew Mackay and Daniel Yuen for their support and enthusiasm. We also thank the other people who participated in this project who included Seonmin Alm, Barry Cox, Andrew Fowler, Zlatko Jovanoski, Sinuk Kang, Salman Subhani and Ngamta Thamwattana.

References

- [1] Abramowitz, M. & Stegun, I. (1970) *Handbook of Mathematical Functions*, Dover, New York.
- [2] Barry, S.I., & Sweatman, W.L. (2009) Modelling heat transfer in steel coils, *ANZIAM J (E)*, submitted.
- [3] Budak, B.M., Samarskii, A.A., & Tikhonov, A.N. (1964) *A collection of problems in mathematical physics*, Dover, New York.
- [4] Landman, K., & McGuinness, M. (2000) Mean Action Time for Diffusive Processes, *Journal of Applied Mathematics and Decision Sciences*, **4**(2), 125–141.
- [5] Hickson, R., Barry, S., & Mercer, G. (2009) Heat transfer across multiple layers, *ANZIAM J (E)*, submitted.
- [6] Sridhar, M.R., & Yovanovicht, M.M. (1994) Review of elastic and plastic contact conductance models: Comparison with experiment, *J. Thermophysics Heat Transfer*, **8**, 633–640.
- [7] Stikker, U.O. (1970) Numerical simulation of the coil annealing process, in *Mathematical Models in Metallurgical Process Development*, Iron and Steel Institute, Special Report **123**, 104–113.
- [8] Willms, A.R. (1995) An exact solution of Stikker’s nonlinear heat equation, *SIAM J. Appl. Math.* **55**, No. 4, 1059–1073.
- [9] Xhang, X., Yu, F., Wu, W., & Zuo, Y. (2003) Application of radial effective thermal conductivity for heat transfer model of steel coils in HPH furnace, *Int. J. Thermophysics* **24**, No. 5, 1395–1405.
- [10] Zuo, Y., Wu, W., Zhang, X., Lin, L., Xiang, S., Liu, T., Niu, L., & Huang, X. (2001) A study of heat transfer in high-performance hydrogen Bell-type annealing furnaces *Heat Transfer — Asian Research*, **30** (8) 615–623.

The response of power systems to autonomous “grid friendly” devices

Bill Whiten

University of Queensland

Glenn Fulford

Queensland University of Technolog

Roslyn Hickson

University of New South Wales @ADFA

Geoff Pritchard

University of Auckland

1 Introduction

Transpower operates the New Zealand electric power grid. For this MISG project they were interested in the possible effects on the power grid of autonomous load controlling devices which are installed in domestic appliances (such as fridges, air conditioners, heaters). These devices are known as grid friendly devices as they have the potential to assist in the management of grid disturbances by reducing load when there is a drop in power supply (U.S. patent 4317049, “Frequency Adaptive Power-Energy Re-scheduler”, “Grid Friendly” is a trademark of Battelle Memorial Institute). The grid friendly devices are implemented as a small electronic control unit in domestic appliances such as water heaters and refrigerators.

In an alternating current grid the system, frequency drops from the normal 50 Hertz to a lower value when the demand for power (load) is greater than the power being generated. A sudden disturbance, such as a generator going offline, causes a drop in frequency until the control systems increase power generation to make up for the loss. A typical event causes the frequency to drop for about a minute. Grid friendly devices use this connection between load and frequency to determine when to turn appliances off and then back on.

The grid friendly devices are capable of reducing power consumption more rapidly than generation can be increased, and hence can make the power distribution grid more stable and allow quicker recovery from disturbances. This is important as a large uncorrected disturbance can cause load shedding and the protective shutdown of equipment, with resulting major power outages. However unlike other protection devices (such as controlled load shedding) on the power distribution grid, the grid friendly devices work autonomously and are not under the control of the grid operator. One concern is, since not all appliances will be using power when a disturbance occurs their effect is variable, and hence the grid operator cannot predetermine the size of the effect. The grid friendly devices also effect the power balance on the grid when they switch back on, and again this is not under the control of the grid operators. Under some circumstances the effect of the grid friendly devices may be too large and make the disturbance worse.

The aim of this study was to examine whether the grid friendly devices can have undesirable effects on the power grid, and what design of grid friendly device is best suited to providing additional protection to the grid. This report first develops a simplified model of a power grid, looks at the conditions for stable operation of grid friendly devices, examines alternative designs, and makes recommendations for the design of grid friendly devices.

2 Previous investigations

The Pacific Northwest National Laboratory has conducted a demonstration project [1] in several communities in Oregon and Washington states. This project involved 50 retrofitted residential water heaters, 150 specially manufactured clothes driers, and ran for one year. As the study was conducted in the U.S.A, the nominal frequency is 60 Hertz, as opposed to the 50 Hertz used in New Zealand. The controllers switched off heating elements if the frequency dropped below 59.95 Hertz and switched the heating elements on again 16 seconds after the frequency rose above 59.96 Hertz. The controllers were connected via the internet to a central recording system, to assist in project evaluation. This project found that once initial engineering and approval problems were overcome, the equipment ran smoothly with the users not generally noticing any difference. Some problems occurred with data recording, however it was concluded that the project had successfully demonstrated feasibility and the potential to make a significant contribution to the stability of a power grid. It was estimated that a reserve of up to 20% of the total power usage could be made available through the use of grid friendly devices.

Other investigations of the use of grid friendly devices have generally been restricted to simulation studies. Lu and Hammerstrom [2] undertook a preliminary study for the demonstration project. For this study they collected data on the distribution of grid frequency over two years and used this to determine switching frequencies for the grid friendly devices. The switching frequency was chosen to act before the substation frequency protection relays would activate. These protection relays reduce load by creating blackouts. A plot of the number of occurrences and their duration for different switching frequencies was produced. The switching frequency used was chosen to give a reasonable number of switching events for the demonstration project. They mention but did not investigate the possibility of randomising the switching frequency and the delay time.

Recent papers report other simulation studies [3, 5] that include the effect of switching refrigerators off depending on both the grid frequency and the temperature within the refrigerator. For these units the switch off frequency is increased if the refrigerator temperature is sufficiently low. [5] also included a similar scheme for heaters in their analysis. [3] showed that in the presence of significant wind power (which is inherently variable) on the grid, the grid friendly devices reduced the variation in frequency and extended the time available to bring in more generation capacity. Both papers concluded that grid friendly devices would have significant benefits.

The literature has identified significant potential benefits from the grid friendly devices. However it is not clear what the effect of switching large loads, that are a significant portion of the total load, might be on the stability of the grid. This report looks at the effects of different designs, on both the frequency stability of the grid, and at the effect on the controlled generation that is needed to compensate for changes in the power balance on the grid.

3 Transpower model of a power grid

A power grid consists of generators that provide power, consumers that use power and the power lines that connect generators to consumers. As there are both multiple generators and many power users, the grid is a complex network of interacting devices. Transpower came to the MISG with a Simulink [4] model of the power system which accounted for multiple types of generators and the different levels of control within the power grid. Figure 1 gives the top level of this model and Figure 2 the next level for one of the generator types used in the simulation.

This model was clearly too complex for any analytical analysis of its properties and was also considered too complex for the initial investigation of alternative strategies for the grid friendly devices. Although the model had many parts the two dominant parts of the model were the inertia in the generators and a feedback control system that maintains the grid frequency.

The next section takes these two components and develops a simplified model of the power grid with similar response characteristics to the actual grid. It should be noted that the response of the grid varies depending on the actual load and generators active at the time. For this reason we are interested in what can be deduced about the general behaviour of the grid, rather than an exact simulation of the behaviour of one particular configuration of generators and load.

4 Simplified model of power grid

The electrical power grid is such that the power generated must match the power consumed. The frequency of the alternating current power is determined by the rotation speed of the generators and the power input to the generators is adjusted to maintain a nominal frequency of 50 Hertz. A sudden change in the balance of the power generated caused by, for instance, a loss of some generation capacity causes a voltage drop, typically seen as the dimming of lights, and requires extra power from the remaining generators. The generators initially supply some of the required additional power from the inertial energy stored in their rotational motion. Extracting this energy reduces the speed of the generators and hence the frequency seen on the power grid.

A feedback control is used to adjust the power going to one of the generators to bring the frequency back to the standard 50 Hertz. The time taken to adjust the power to the generators depends on the inertia in the generators and the properties of the feedback control system. Typically a disturbance results in a dip in frequency lasting a few tens of seconds. Too large a disturbance on the grid will invoke protection circuits that shut down power usage and generation, causing major blackouts.

The effective performance of the power grid can be described by (1), which is a balance of the following terms: an inertial term for the power available from the inertia of the generators as frequency changes ($m \frac{df(t)}{dt}$), the net variation of power with frequency $k_f(f_0 - f(t))$ where f_0 is the normal frequency which is 50 Hertz in New Zealand, the power supplied by the controlled generator $p_c(t)$, the power supplied by other generators $p_g(t)$, and the power required by users $p_u(t)$

$$m \frac{df(t)}{dt} = k_f(f_0 - f(t)) + p_c(t) + p_g(t) - p_u(t) \quad . \quad (1)$$

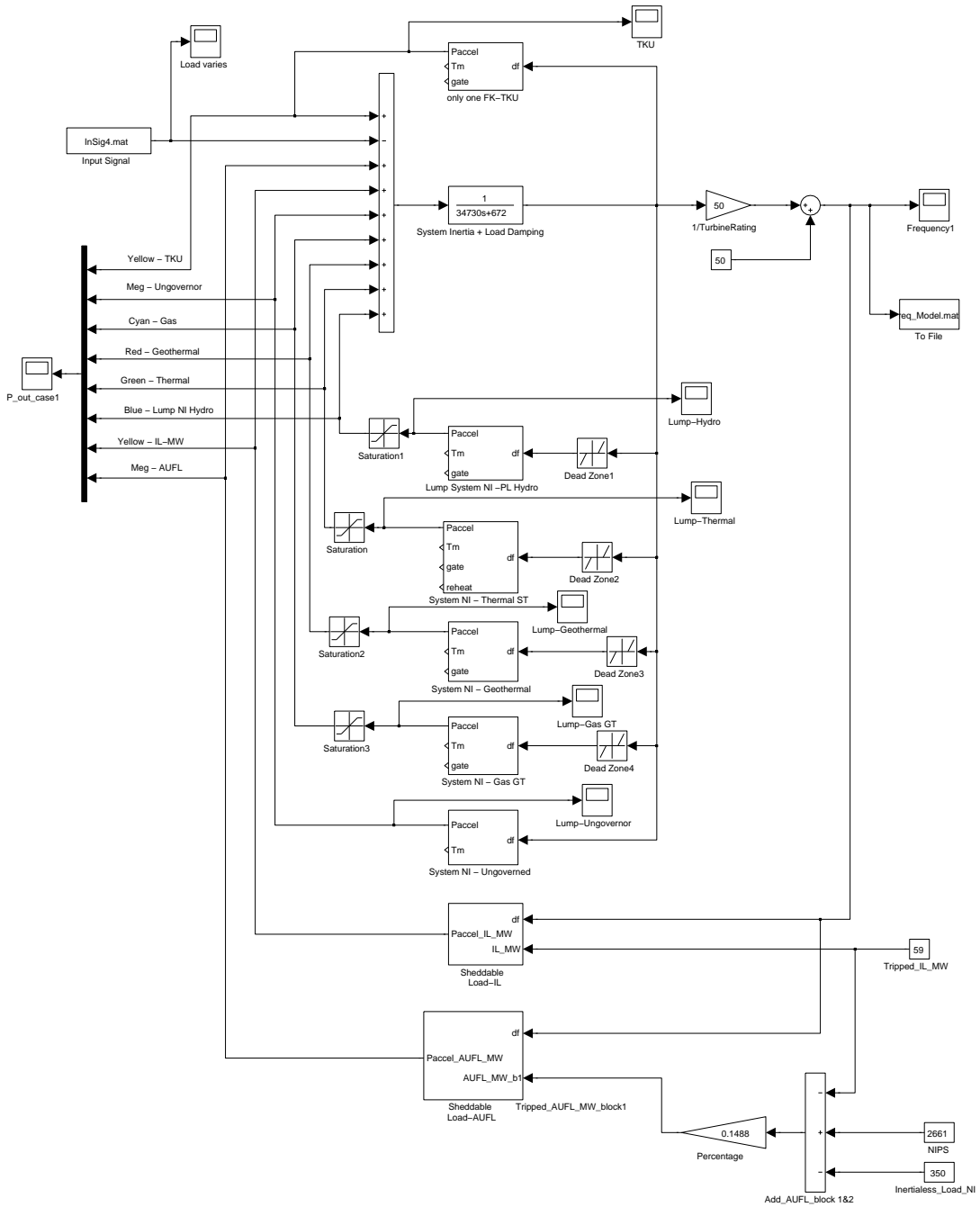


Figure 1: Top level of Transpower Simulink grid model.

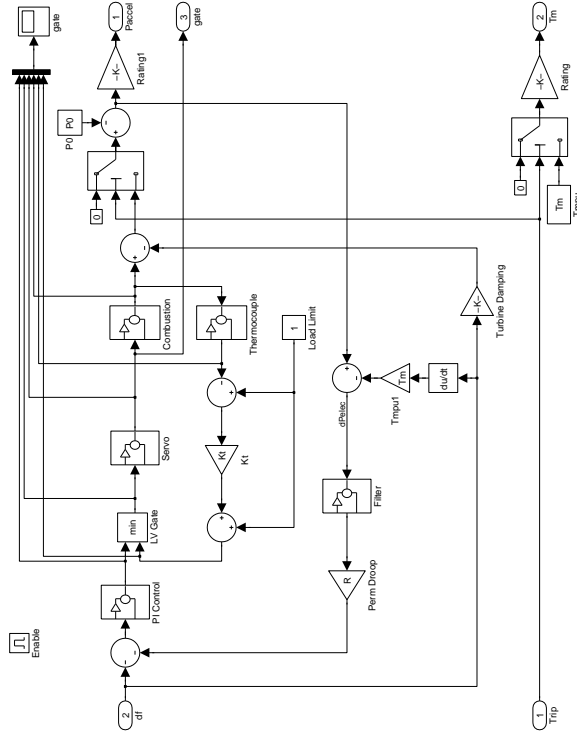


Figure 2: Detail of a generator model in Transpower Simulink model.

The feedback controller is a standard construction, known as proportional plus integral or PI, that consists of two terms, the first proportional to the error in the frequency ($f_0 - f(t)$), and the second proportional to the integral of the error. The two proportionality constants (k_p & k_i) are used to match the controller to the requirements of the process being controlled. The output of this controller sets the power going to the controlled generator. Note that if the frequency is low the controller needs to increase the power to the generator. So the equations describing the controller are

$$p_c(t) = k_p(f_0 - f(t)) + k_i x(t) \quad , \quad (2)$$

where the integral component $x(t)$ is generated by

$$\frac{dx(t)}{dt} = f_0 - f(t) \quad . \quad (3)$$

It is assumed that the control acts promptly in altering the power output of the controlled generator. The controlled generator is chosen for its ability to respond quickly to changes requested by the feedback controller.

For the evaluation of the response of a controlled system it is best to start with the system in steady state and then look at the effect of a disturbance. Thus if an initial (at $t = 0$ for

convenience) steady state operation is assumed

$$f(0) = f_0, \quad x(0) = p_c(0)/k_i, \quad p_c(0) = p_u(0) - p_g(0) . \quad (4)$$

Equations (1), (2) and (3) depend on four parameters (m, k_f, k_p, k_i) which vary according to the grid being simulated, the generators currently being used, and the amount of power being consumed.

For analysis it is convenient to look at variation about the steady state and then reduce to a minimum the number of parameters involved. Selecting scale factors for t and x that simplify the equations gives the following transformed variables with steady state values of zero

$$T = t\sqrt{k_i/m}, \quad F(T) = f(t) - f_0, \quad X(T) = -(x(t) - x(0))\sqrt{k_i/m}. \quad (5)$$

This scaling allows the parameters to be combined into a single parameter

$$K = \frac{(k_f + k_p)}{m\sqrt{k_i/m}} , \quad (6)$$

and finally the power difference can be scaled to a corresponding change in frequency

$$P_d(T) = P_d(t\sqrt{k_i/m}) = \frac{p_u(t) - p_g(t) - (p_u(0) - p_g(0))}{(k_f + k_p)} . \quad (7)$$

It should be noted that the scaling of power to Hertz is system dependent, thus working with the scaled values has the advantage of being independent of the particular grid parameters. The equations could be made non dimensional by dividing by the standard frequency, however as this gives no further advantage, it is more convenient to retain the frequency dimension for $F(T)$.

Hence starting with the frequency and controller equations (1), (2) & (3), eliminating $p_c(t)$, using equations (5) to eliminate t , $f(t)$ and $x(t)$, substituting the values of K and $P_d(T)$ (e.g. by eliminating k_f & $p_u(t)$), and applying the initial steady state conditions to eliminate $x(0)$ and $p_c(0)$ gives

$$\frac{dF(T)}{dT} = -K\{F(T) + P_d(T)\} - X(T) \quad (8)$$

and

$$\frac{dX(T)}{dT} = F(T) . \quad (9)$$

This shows that other than a scaling of the time axis, there is just one parameter that controls the shape of the response to a disturbance from $P_d(T)$. The initial values $F(0)$, $X(0)$ and $P(0)$ are zero for the initial steady state.

Figure 3 shows the range of responses to a step change in $P_d(T)$ for this system as the value of K is changed. The amplitude of the response $F(T)$ depends on the amplitude of the disturbance. Depending on the value of K the response changes from a damped oscillation to an exponential decay.

The speed of response in real time t , for a given K value can be increased by increasing k_i and k_p in the manner that maintains K constant. The above equations appear to indicate the response speed can be increased indefinitely, however physical limits apply to the range and change rate of the controlled generator. These limit the speed at which the system can return

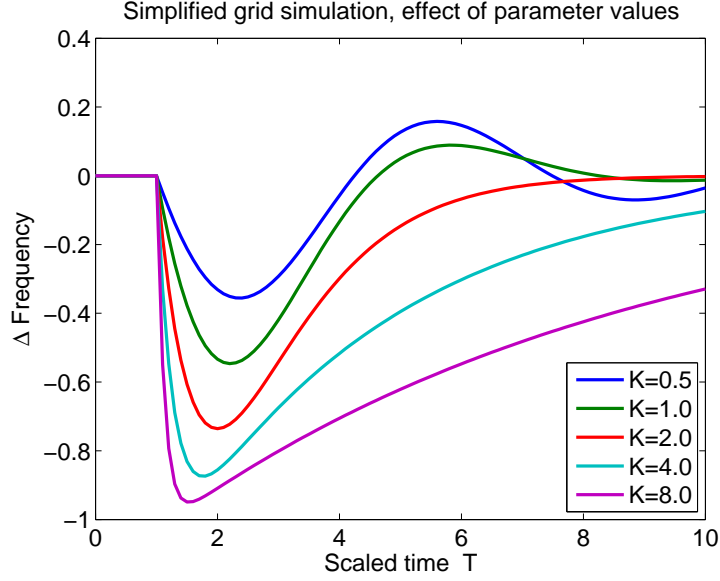


Figure 3: Possible responses of the grid to a step change in power generation, using scaled time. A step change of -1 in frequency, corresponding to a loss of generation capacity, was applied at time 1.

to steady behaviour. In addition the assumed model of the grid response has limitations in that it is only modelling the slower responses of the grid, has neglected the controls within the individual generators and the actual implementation of the controller which could be a discrete approximation to the controller equations used above.

The controller output is $p_c(t)$ which can be obtained from the scaled values as

$$p_c(t) = -k_p F(T) - k_i \left(X(T) / \sqrt{k_i/m} - x(0) \right) \quad (10)$$

and this can be scaled similar to the other power values to give the scaled controller output

$$C(T) = - \frac{k_p F(T) + k_i \left(X(T) / \sqrt{k_i/m} - x(0) \right)}{k_p + k_i} . \quad (11)$$

The range of this variable is determined by the power range of the controlled generator.

Comparing the responses in Figure 3 with an actual response will allow the time scale factor $\sqrt{k_i/m}$ and the value of K to be determined. By combining these, other ratios of the original parameters can be obtained. The values of k_p and k_i can be obtained from the physical controller implementation together with its input and output scale factors. We then have sufficient information to determine the other two original parameters, namely m and k_f .

Inspection of an actual grid response to the loss of a generator supplied by Transpower figure 4, shows that this simple model with a value for K of about 1.5 gives a response similar to that seen in this example. The responses of the power grid to a disturbance vary to some extent depending on the load and generators in use at the time of the disturbance.

The simple model provided two significant advantages: it enabled some analytical analysis of the system behaviour and it provided a convenient system on which to test the effect of various grid friendly devices.

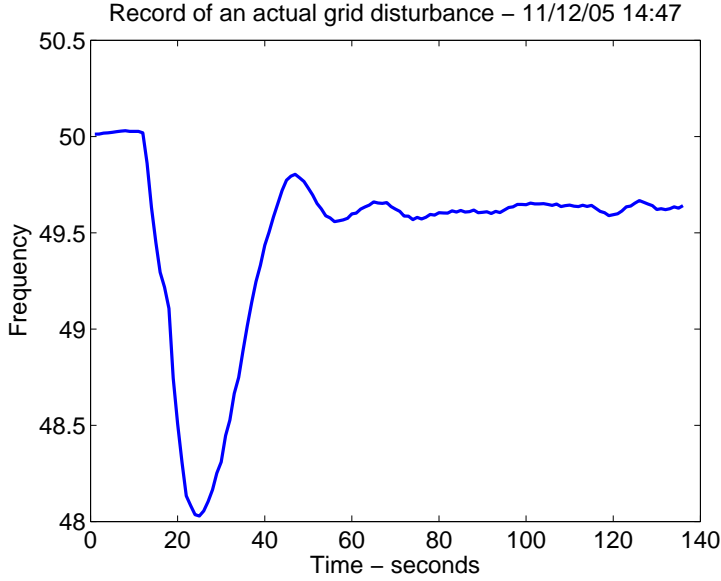


Figure 4: Recorded effect of a step change in power generation on the Transpower grid.

The eigenvalues of the system given by equations (8) and (9) are

$$-K/2 \pm \sqrt{(K/2)^2 - 1} \quad (12)$$

which always have a negative real part and hence this model of the control system is stable for all positive values of m , k_f , k_p and k_i . For small values of K the solution is a decaying oscillation, and for values of K greater than 2 the solution consists of two decaying exponentials.

Note however the model is an approximation that neglects certain aspects of the physical system that would add small higher order terms to the differential equations and possibly change the controller differential equations to difference equations. These could result in the control becoming unstable at high values of the gains k_p and k_i .

5 Inclusion of grid friendly devices

The goal of a grid friendly device is to make a change in the power consumption based on the frequency it sees. This appears in the power equation (1) as part of the power consumption required by the users $p_u(t)$. The power used by the grid friendly devices is determined by their current need for power and by the frequency they see on the grid. In the following we will assume that the need for power is a constant, and the actual amount of power used is reduced based on some algorithm that uses measurements of the frequency.

The effect of the grid friendly devices is conveniently included by removing their effect from the scaled net power $P_d(T)$ and defining the effect of the grid friendly devices as $G(F)$ which is scaled in frequency similarly to $P_d(T)$. Define $P(T)$ as

$$P(T) = P_d(T) - G(F(T)) \quad (13)$$

so that equation (8) becomes

$$\frac{dF(T)}{dT} = -K\{F(T) + P(T) + G(F(T))\} - X(T) \quad . \quad (14)$$

Here $G(F)$ by appropriate choice of the base power level in (7) can be assumed to be zero for normal operation and negative when the frequency drops and the device is not consuming power. This allows steady state values of zero which will be useful for an analysis using stability conditions.

The grid friendly devices are represented here by the function $G(F)$, which is not necessarily a simple function of F as it can also use a memory of past behaviour and possibly incorporate time delays. A major aim of this MISG project was to determine the effect of different algorithms for the behaviour of the grid friendly devices on the grid. From this recommendations for the best designs for the grid friendly devices can be made.

The Simulink diagram for the grid with the inclusion of a grid friendly device is given in Figure 5. This can be compared with Figures 1 and 2 to see how the essential behaviour of the grid is much simpler than a full simulation.

5.1 Stability analysis for grid friendly devices

Equations (9) and (14) describe the behaviour of the combined power grid and grid friendly devices. For a steady state there should be no disturbances entering the grid, which means $P(T)$ is constant. It is then possible to choose $x(0)$ in equation (5) so that $P(T)$ trends to zero after an initial disturbance, such as the loss of a generator. Now consider the energy like term

$$E(T) = F(T)^2 + X(T)^2 \quad . \quad (15)$$

It is clear that if $E(T)$ goes to and stays at zero, $F(T)$ and $X(T)$ have reached steady states of zero. Differentiating this with respect to T , and substituting from the differential equations (9) and (14) gives

$$\begin{aligned} \frac{dE(T)}{dT} &= 2F(T)\frac{dF(T)}{dT} + 2X(T)\frac{dX(T)}{dT} \\ &= 2F(T)\{-K\{F(T) + G(F(T))\} - X(T)\} + 2X(T)F(T) \\ &= -2KF(T)^2 - 2KF(T)G(F(T)). \end{aligned} \quad (16)$$

With $G(F(T))$ zero, (14) and (9) are linear, and hence $E(T)$ must decrease to zero, as its derivative is negative or zero and can only remain zero when both $F(T)$ and $X(T)$ are zero.

As $G(F(T))$ is zero when the grid friendly devices are switched on and negative when they are switched off, the term $F(T)G(F(T))$ can be guaranteed to be positive, provided the grid friendly devices are on (i.e. consume power, $G(F(T)) = 0$) when the frequency is equal to or above the normal frequency ($F(T) \geq 0$). Under this condition the effect of $G(F(T))$ is to make the derivative more negative and hence speed the decrease of $E(T)$ to its stable zero value.

Thus provided the grid friendly devices are only switched off when the frequency is lower than the normal frequency the grid response is stable and further the effect of the grid friendly devices is to improve the stability by creating a faster return to normal conditions.

It should also be noted that large values of K (6) will cause E to reach zero faster and hence a quicker return to stable conditions. This is also seen in the eigenvalues given in (12).

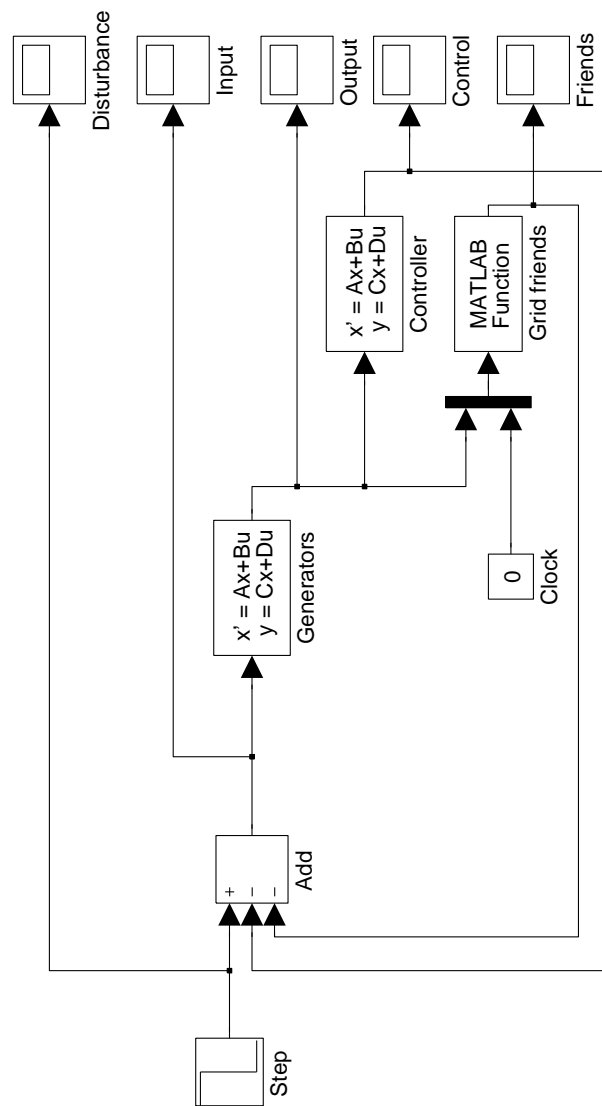


Figure 5: Simulink model of simplified grid equations with grid friendly devices.

This analysis has looked at the stability in terms of the two state variables $F(T)$ and $X(T)$. However it is also desirable that the right hand side of equation (14) remains smooth. In particular repeated switching of large loads on and off is to be avoided. Hence an examination of performance needs to look at both the frequency and the input to the frequency equation.

5.2 An additional stability result

For the case where the frequency response is non oscillatory ($K \geq 2$) and the grid friendly devices act to turn off power progressively at frequencies less than f_0 and also turn the devices back on progressively as the frequency returns to f_0 (but not at a value lower than the turn off frequency) it is possible to derive an additional stability result.

It can be shown that in this case the load changes made by the grid friendly devices maintain a non oscillatory response. Over the range where the grid friendly devices operate proportional to frequency with a positive slope (i.e. less power is used when the grid frequency is lower), their effect is to change the response to that obtained with a larger value of K , which corresponds to an increase in the amount of damping. The derivation of this result is given in the appendix.

6 Simulation of Grid Friendly Devices

The grid friendly devices are actually multiple independent units. When they all switch at the same frequency they can be considered as a single device. Similarly when they switch over a range of frequencies the continuous approximation of a single device can be used. When the devices use a more complex algorithm that involves a memory of past behaviour in the individual devices, it becomes difficult to express this as a single device that integrates the behaviour of the individual devices. For this reason the simulations below have been done using a simulation of a sufficient number (500) of individual grid friendly devices each implementing the algorithm under test.

The following subsections look at different possible implementations of the grid friendly devices. In the formulas where it has been possible to describe the units as a single device this has been done using Q as the total frequency change, and where the formula for a single unit needs to be used a frequency change of q for each unit is used. For comparison, the behaviour of the grid for the same disturbance without any grid friendly devices is given in Figure 6. Here a loss of power disturbance equivalent to a drop in frequency of 10 units occurs at time 1. This graph and the following graphs are generated using (9) & (14), and show the change in frequency (Frequency, equation (5)), the scaled output to the controlled generator (Controlled, equation (11)), and the scaled output of the grid friendly devices (Grid Friendly, introduced in equation (13)).

The controller response has been chosen for a quick recovery to the base frequency with almost no overshoot, and a minimal overshoot in the controlled power. A faster return to the normal frequency can be obtained with a larger overshoot in the controller output, however this is undesirable and may not be feasible. For this reason it is always necessary to check that the controller output is acceptable, as well as checking the response of the controlled variable (frequency in this case). The parameters used in the following simulations are: $k_f/m = 1$, $k_p/m = 1$, and $k_i/m = 1.5$ which give $K = 1.63$.

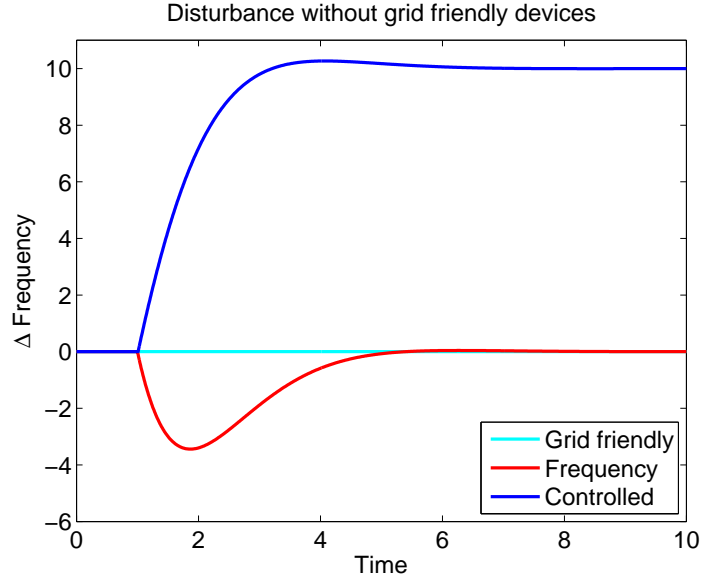


Figure 6: Response of the simulated grid to a disturbance without any grid friendly devices.

6.1 Simple grid friendly devices

The simplest case for the grid friendly function is switching off if the frequency is below a given value ($a < 0$) that is

$$G(F) = \begin{cases} 0, & F > a, \\ -Q, & F \leq a < 0. \end{cases} \quad (17)$$

Figure 7 shows a typical response of this device. Compared with Figure 6 the grid friendly devices have reduced the size of the disturbance in the frequency, but as the grid recovers the grid friendly devices switch on and off rapidly as the switch frequency is crossed, and this holds the frequency at the switching frequency until adjustment from the grid friendly devices is no longer needed. During recovery once the switching frequency is reached the oscillation in the devices delays the recovery of the power grid to the normal frequency. In the case where the grid friendly devices control more power than the disturbance the oscillation starts as soon as the switching frequency is reached.

While this case improves the frequency response by reducing the size of the frequency overshoot, the rapid switching of the devices at the switching frequency delays recovery and is quite undesirable.

6.2 Addition of dead band

To avoid the rapid switching of the grid friendly devices a dead band can be introduced. For this case it is necessary to introduce a memory for the state of the device output when the frequency is in the dead band region $-a < F < -b$ ($a > b > 0$), as in this region there are two possible outputs (0 or $-Q$). The algorithm uses an internal memory Z to remember the state of the output when F is in the dead band and can be implemented as

$$G(F) = Z$$

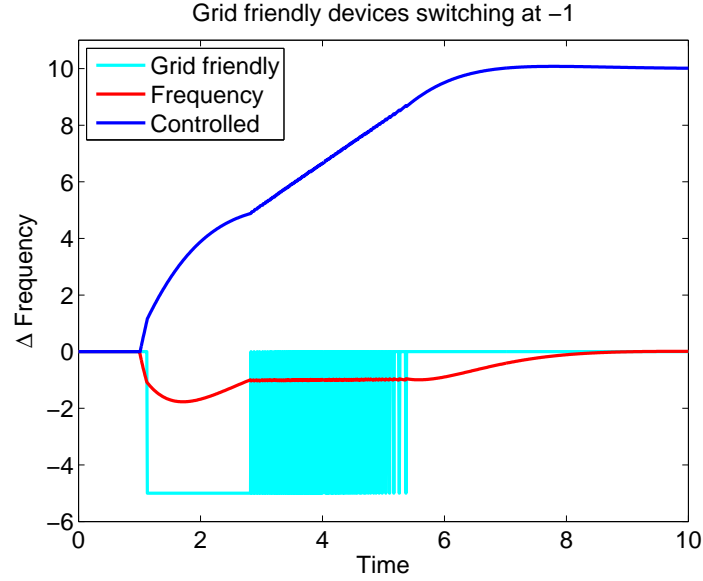


Figure 7: Response from a simple grid friendly device switching at a given frequency.

$$\begin{aligned}
 & \text{if } (F > -b) \quad G(F) = 0 \\
 & \text{if } (F < -a) \quad G(F) = -Q \\
 & Z = G(F) \quad .
 \end{aligned} \tag{18}$$

The value of Z needs to be initialised to zero before this algorithm is run.

As seen in Figure 8 there is again an improved frequency response. However if the grid friendly devices control enough power there will be oscillation between the two switching frequencies. A larger dead band reduces the possibility of oscillation and reduces the frequency of oscillations that do occur. The higher value of the switch on frequency allows a recovery to closer to the normal frequency, before the switching back on of the grid friendly devices acts to delay the recovery to the normal frequency. The repeated switching of the grid friendly devices is also seen in the controlled power as an undesirable saw tooth as the controller output tries to adjust to the oscillating power usage.

6.3 Addition of a delay before switching back on

This case is similar to that used in the grid friendly demonstration trial [1] and investigated in the paper by Lu and Hammerstrom [2]. Here the grid friendly devices do not switch back on until a given time after the frequency has recovered to a value above the switch off level. To implement this access to the time (T) or a count down timer is needed in the grid friendly devices. Here a is the switching level below the normal frequency and c is the time delay

$$\begin{aligned}
 & G(F) = Z \\
 & \text{if } (F < -a) \quad G(F) = -Q; \quad t_0 = T \\
 & \text{if } (F > -a \ \& \ T - t_0 > c) \quad G(F) = 0 \\
 & Z = G(F) \quad .
 \end{aligned} \tag{19}$$

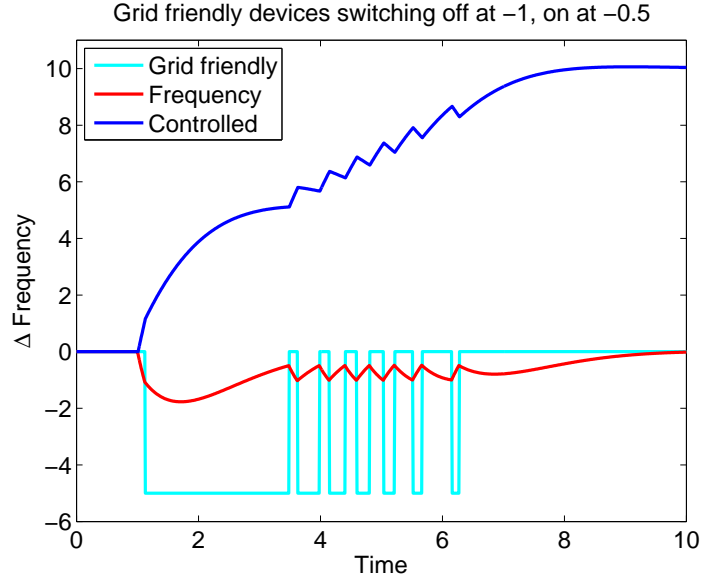


Figure 8: Response from a simple grid friendly devices switching at a given frequency.

This needs to have initial values of $Z = 0$ and $t_0 = T$ set before the algorithm is applied:

In this case the switching on of the devices occurs without consideration of the effect on the grid. When the devices control sufficient power the effect of them switching on may create a disturbance sufficient to drive the frequency low enough to cause the devices to switch off again, starting an oscillation. Figure 9 shows how this type of grid friendly device can give undesirable oscillations. For smaller amounts of grid friendly power there may not be any oscillation, or there could be a few cycles before the grid returns to the steady condition.

6.4 Spreading the switching frequency

Here the switching frequency is spread over a range by each device switching at a different frequency within a predetermined range. The actual frequency used by each device could be set during manufacture, or better, determined by random selections during operation which would make the average performance of each device the same. In this case it is possible to describe the integrated behaviour of the grid friendly devices as ($a > b > 0$)

$$G(F) = \begin{cases} 0 & F > -b < 0 \\ -((b+F)/(b-a)) Q & -b \geq F \geq -a \\ -Q & -a > F. \end{cases} \quad (20)$$

This has the advantage of giving a proportional response that is able to adjust to the size of the disturbance. In particular it avoids the possibility of too large a drop in load and the frequency going above the desired 50 Hertz value. Figure 10 shows the effect of this algorithm. With the switching range chosen suitably the reduction in the frequency drop is similar to switching at a given value, but the return to using power by the grid friendly devices is now smooth. The return of the grid friendly devices does slow the recovery to the normal frequency. However the controller output is now back to an acceptable smooth behaviour.

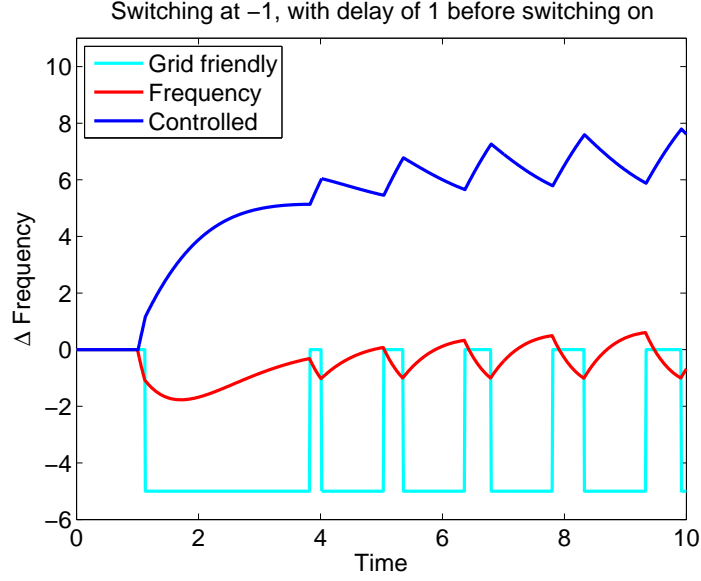


Figure 9: Response from grid friendly devices with a time delay before switching back on.

6.5 Spread switching frequency with dead band

The above sections describe the grid friendly devices as a single unit that combines the effect of the multiple devices. This is difficult to implement for this case and instead a description of one device is given and this is used multiple times in the simulation. To obtain a spread of frequencies, the switch frequencies for the individual devices are determined within the range allowed using random numbers. The frequency range used to switch the device off is from a_{off} to b_{off} ($a_{off} < b_{off} < 0$) and for switching the device back on a_{on} to b_{on} ($a_{on} < b_{on} < 0$ and $a_{off} < a_{on}$, $b_{off} < b_{on}$). The algorithm for each device is

$$\begin{aligned}
 G(F) &= z \\
 \text{if } (F > b_{on} \ \& \ z < 0) \\
 & \quad r = \text{random}(0, 1) \\
 & \quad s_{on} = a_{on} + r(b_{on} - a_{on}) \\
 & \quad s_{off} = a_{off} + r(b_{off} - a_{off}) \\
 & \quad G(F) = 0 \\
 \text{if } (F < a_{off}) \ G(F) &= -q \\
 z &= G(F) \ .
 \end{aligned} \tag{21}$$

Similar to the case in Section 6.2 initialisation of the internal variables is needed. This is

$$\begin{aligned}
 z &= 0 \\
 r &= \text{random}(0, 1) \\
 s_{on} &= a_{on} + r(b_{on} - a_{on}) \\
 s_{off} &= a_{off} + r(b_{off} - a_{off}) \ .
 \end{aligned} \tag{22}$$

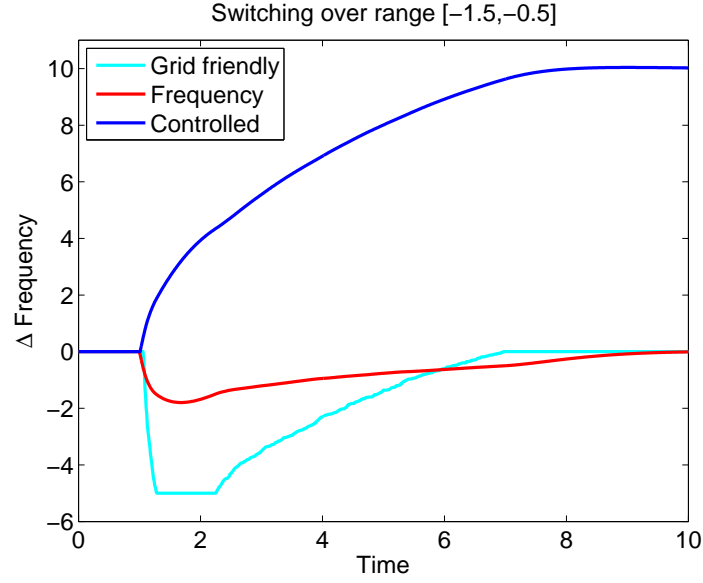


Figure 10: Response from a grid friendly device switching over a range of frequencies.

Note here the change in power is q for one device and the total possible change is the number of devices times q . The total effect of these grid friendly devices (Figure 11) is obtained by adding up the effects of each of the devices. Typically the simulations use 500 devices, which is sufficient to give a close estimate of the effect of many devices.

Similar to the previous case there is an offset from the target frequency as the devices turn back on. However the dead band allows the offset to be moved closer to the normal frequency.

6.6 Addition of a time delay before switch on

Here a range of switch off frequencies are used, but the condition for switching back on includes a random delay after the frequency has recovered beyond the switch on frequency, which is also given a range of values. The random time delay gives the grid frequency more time to recover before the additional load is placed on the grid and ensures there is a progressive addition of load to the grid. To implement the time delay there needs to be access to a clock (T the value of which increases with time), as in the following

$$\begin{aligned}
 G(F) &= z \\
 \text{if } (F > b_{on} \ \&\& \ z < 0 \ \&\& \ T - t_0 > c) \\
 & \quad r = \text{random}(0, 1) \\
 & \quad s_{on} = a_{on} + r(b_{on} - a_{on}) \\
 & \quad s_{off} = a_{off} + r(b_{off} - a_{off}) \\
 & \quad c = c_{min} + r(c_{max} - c_{min}) \\
 & \quad G(F) = 0 \\
 \text{if } (F < a_{off}) \ G(F) &= -q
 \end{aligned}$$

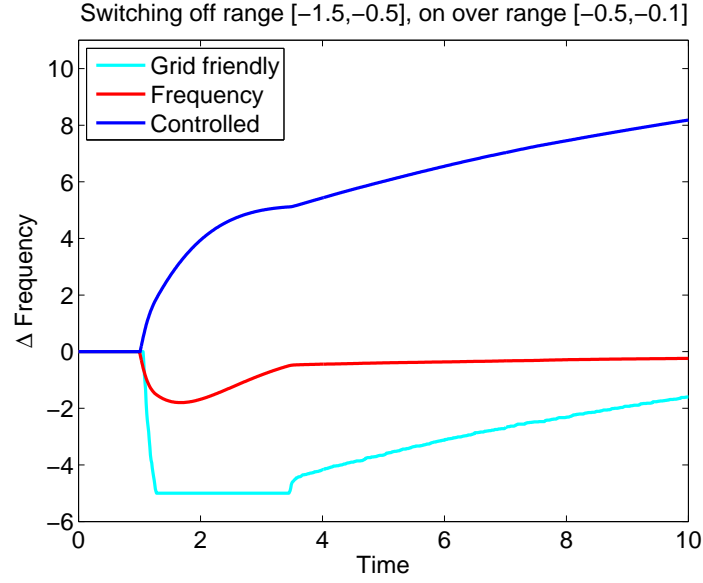


Figure 11: Response from simple grid friendly devices switching over a range of frequencies and using a dead band.

$$\begin{aligned} \text{if } (F < a_{on}) \ t_0 = T \\ z = G(F) \ . \end{aligned} \quad (23)$$

Again an initialisation of the internal variables is needed. This is

$$\begin{aligned} z &= 0 \\ r &= \text{random}(0,1) \\ t_0 &= T \\ s_{on} &= a_{on} + r(b_{on} - a_{on}) \\ s_{off} &= a_{off} + r(b_{off} - a_{off}) \\ c &= c_{min} + r(c_{max} - c_{min}) \ . \end{aligned} \quad (24)$$

This gives the best performance (Figure 12) in that the switching off of the grid friendly devices occurs in proportion to the size of the disturbance, and switching back on is delayed until the frequency has largely recovered. The distribution of time delays brings in the devices slowly after the frequency has recovered sufficiently. Should the extra load from switching some devices back on be sufficient to drop the frequency, others will delay switching back on until the frequency has recovered sufficiently.

7 Comments on simplified model

There are three main approximations made in the simplified model:

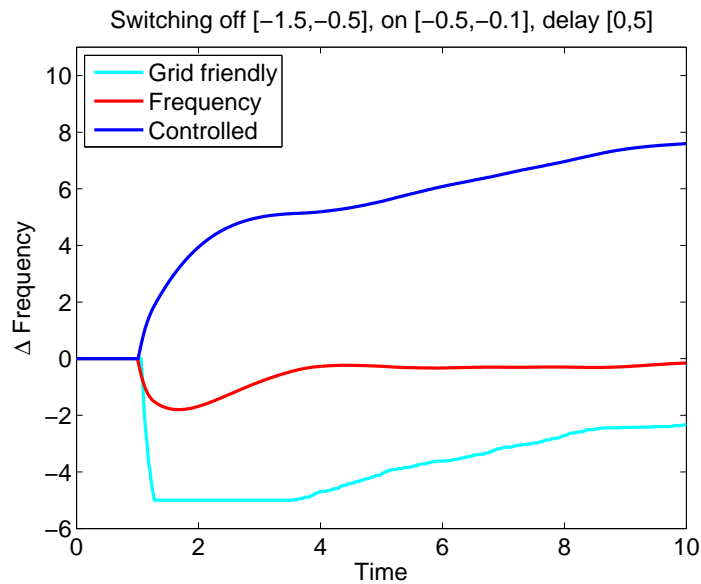


Figure 12: Response from grid friendly devices switching over a range of frequencies and using both a dead band and a delay.

1. The process model for f actually contains additional terms that become significant when the process is required to respond faster than the time scales for which the model was developed.
2. The control is implemented by equipment that is not able to respond at very high speeds. Typically it is implemented using discrete time steps and may be rate limited.
3. The grid friendly devices do not implement a continuous switching of power, but switches network load in discrete steps.

If the feedback gains k_p , k_i or $G(F)$ become too great these approximations become important and the grid system could become unstable. The levels at which this occurs need to be tested on the more complex model.

8 Conclusions

The simplified model has proved very useful for analysis of stability conditions, and for testing the effect of various designs for the grid friendly devices.

The grid friendly devices have a clear ability to assist in making the grid more tolerant to disturbances by decreasing load when there is a drop in generation capacity.

Provided the power being switched by the grid friendly devices is not too large, compared with the disturbance that initiates switching, it makes little difference whether they all switch off at the same frequency or switch off over a range of frequencies. If the grid friendly devices control a larger amount of power switching over a range of frequencies allows the amount of load reduced to be proportionate to the power loss. This then avoids too large a correction that causes the grid frequency to rise above the normal value.

The effect of the grid friendly devices when they switch back on after a disturbance has the potential to cause problems on the grid. If they all switch on at the same frequency or time they create another disturbance and drop in frequency, which may well be sufficient to cause the devices to switch off again, possibly multiple times. To avoid this the switching back on of the grid friendly devices needs to be spread out, either over a frequency, over time or both. Spreading out over frequency even when offset from the switch on frequencies has the effect of delaying recovery to the normal frequency. So the best option is switching back on after a variable delay, provided the frequency has recovered sufficiently, with the recovery frequency value being spread over a range of frequencies.

9 Acknowledgements

The project moderators thank the industry representatives, Doug Goodwin and Cynthia Liu, for their enthusiasm in preparing, presenting and explaining this project for this MISG meeting. The three project moderators are also grateful to Rachel Blakers, Zlatko Jovanoski, Mark Nelson and Peter Tristcher who gave their time and expertise to assist with this project.

10 Appendix: Additional stability result

In this appendix an alternative stability result is derived for the case where the control response is not oscillatory, that is for critically or over damped responses. It is found in this case that a wide range of grid friendly device designs, increase the amount of damping on the power grid.

Consider equations (1), (2) & (3), assume p_g constant, and $p_u(t) = a + bf(t)$ with $a \geq 0$ & $b \geq 0$, for some range of $f(t) < f_0$ which corresponds to the grid friendly devices reducing power usage as the frequency decreases, and increasing power usage when the frequency rises. It is assumed that power usage function corresponding to the combined action of the grid friendly devices, can consist of piecewise sections. This provides a method of specifying a class of grid friendly devices that includes the range of typical implementations.

Differentiate equation (1), replace df/dt by y , substitute for p_c from (2), and substitute for dx/dt from (3) to get

$$\frac{df(t)}{dt} = y(t), \quad \frac{dy(t)}{dt} = -\frac{k_f + k_p + b}{m}y - \frac{k_i}{m}(f(t) - f_0). \quad (25)$$

The condition for these equations to be non oscillatory without the effect of the grid friendly devices (i.e. $b = 0$) is

$$(k_f + k_p)^2 \geq 4mk_i \quad . \quad (26)$$

When $b > 0$ the left hand term in (26) becomes $(k_f + k_p + b)^2$ and the inequality still holds.

Figure 13 shows a solution to (25) and defines three regions. For a loss of generation capacity $f(t)$ is initially less than f_0 . Now consider the (f, y) plane:

In the quadrant $f < f_0$ & $y \leq 0$ (region A): $dy/dt > 0$ & $df/dt \leq 0$ so the solution to (25) always increases in y and exits the quadrant through $y = 0$.

In the quadrant $f \leq f_0$ & $y > 0$ (regions B & C): $df/dt \geq 0$ so that the solution of (25) always travels towards the y axis.

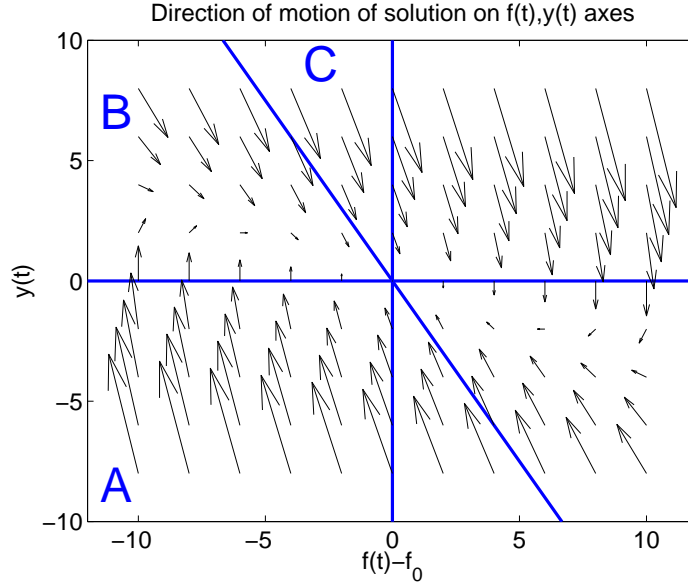


Figure 13: Solution to equations (25) shown as vectors giving magnitude and direction of the solution at various points in the $f(t), y(t)$ plane. The three regions marked are those referred to in the text. Parameters used for this plot are $(k_f + k_p)/m = 3$, $b = 0$ and $k_i/m = 1$. The sloping line is $3(f(t) - f_0) + y(t) = 0$.

On the line

$$(k_f + k_p)(f - f_0) + 2my = 0 \quad (27)$$

the y derivative from (25) becomes

$$\frac{dy}{dt} = -\frac{k_f + k_p + b}{m} \left(-\frac{(k_f + k_p)(f(t) - f_0)}{2m} \right) - \frac{k_i}{m}(f(t) - f_0). \quad (28)$$

Using the inequality (26) this becomes

$$\frac{dy}{dt} \leq -\left(\frac{(k_f + k_p + b)(k_f + k_p)}{2m^2}(f(t) - f_0) - \frac{(k_f + k_p)^2}{4m^2} \right) (f(t) - f_0) \quad (29)$$

and this after simplification is

$$\frac{dy}{dt} \leq \frac{(k_f + k_p)(k_f + k_p + 2b)}{4m^2}(f(t) - f_0). \quad (30)$$

Thus dy/dt is negative on the line (27) for $f < f_0$. The f derivative on the line (27) becomes

$$\frac{df}{dt} = -\frac{(k_f + k_p)}{2m}(f(t) - f_0) \quad (31)$$

which is positive for $f < f_0$.

From (30) & (31) on the line (27) in the (f, y) plane, the slope of the solutions to (25) is

$$\frac{dy/dt}{df/dt} \leq -\frac{(k_f + k_p + 2b)}{2m} \leq -\frac{(k_f + k_p)}{2m}, \quad (32)$$

where the last expression is the slope of the line (27). Hence the solution of (25) crosses the line in the downward direction when $f < f_0$ (or in the limiting case moves along the line).

Hence once the solution to (25) is in the region $f \leq f_0$ between the lines (27) and $y = 0$ (region B, Figure 13), it moves in the direction of increasing f until it reaches the stable point $f = f_0, y = 0$. Solutions that start with $f \leq f_0$ but $y < 0$ (region A) enter the region between lines (27) and $y = 0$ (region B) across the line $y = 0$ and thus then go to $f = f_0$ & $y = 0$.

When the grid friendly devices are implemented as joined piecewise sections with $b \geq 0$ for each section, the solution of (25) is continuous and each section of the solution that starts in the region $f < f_0$ & $y < (k_f + k_p)(f - f_0) + 2my$ (regions A & B, Figure 13) remains in this region. Hence the solution once in this region remains in the region, and heads towards the stable point $f = f_0$ & $y = 0$.

The effect of grid friendly devices implemented in this manner is to increase the amount of damping in the solution of equations (25).

References

- [1] Hammerstrom, D.J. (Principal Investigator) (2007) *Pacific Northwest GridWiseTM testbed demonstration projects - Part II Grid FriendlyTM appliance project*, Pacific Northwest National Laboratory (Richland, Wa), grid-wise.pnl.gov/docs/gfa_project_final_report_pnnl17079.pdf
- [2] Lu, N. & Hammerstrom, D.J. (2006) *Design considerations for frequency responsive Grid FriendlyTM appliances*, IEEE/PES Transmission and Distribution Conference and Exhibition, 2005/2006, (IEEE, Piscataway NJ), 647-652.
- [3] Short, J.A., Infield, D.G. and Freris, L.L. (2007) *Stabilization of grid frequency through dynamic demand control*, IEEE Transactions on power systems 22:3, 1284-1293.
- [4] Simulink (2008) www.mathworks.com/products/simulink/, www.mathworks.com/.
- [5] Xu, Z., Ostegaard, J., Togeby, M. and Marcus-Moller, C. (2007) *Design and modelling of thermostatically controlled loads as frequency controlled reserve* Power Engineering Society General Meeting 2007, IEEE (ISBN 1-4244-1298-6) 1-6.

The shelf life of wine

Geoff Mercer

University of New South Wales @ADFA

Andy Wilkins

CSIRO

Jonathon Crook

Victoria University of Wellington

Steve Barry

University of New South Wales @ADFA

Andrew Fowler

University of Limerick

1 Introduction

The aim of this project was to investigate and develop models for the shelf life of bottled wine and, in particular, the effects of elevated temperatures on the aging process. The MISG group divided the problem into three sub-problems. First, calculations were made to describe the temperature of wine in a single bottle when subjected to an elevated external temperature and then this was extended to pallets of cartons of wine. This has application to determining the temperature of the wine during both the transport and storage of wine. Second, equations were derived for the gas flow through the cork when a wine bottle is subject to oscillatory temperature variation such as is common in a domestic storage situation. This has important implications to the aging processes in the wine as cork breathing can lead to increased oxidation of the wine. Third, the temperature dependent reaction rates of the wine aging processes were considered and calculations performed on how elevated temperatures decrease the shelf life compared to ideal cellaring conditions. Suggestions were made as to relatively simple experiments that can be performed to test the aging models developed here.

2 Heating of the bottle and wine

The temperature of wine in a bottle is quantified using numerical simulation for two simple cases: an initially cool bottle standing in a hot environment; an initially cool, large pallet of bottles standing in a hot environment. These are the two extremes which can occur during the transportation and storage of wine. Throughout the numerical simulations the physical parameters used are given in Tables 1 and 2. The numerical simulations are performed using a finite element package FlexPDE that is space and time adaptive to enable the fine spatial structure such as the glass and cork to be modelled.

Feature	value
Bottle base radius	3.81 cm
Bottle neck radius	1.48 cm
Bottle base height	20.0 cm
Bottle neck height	10.0 cm
Total bottle height	30.0 cm
Cork height	4.0 cm
Bottle volume	981 ml
Wine volume	750 ml
Cork volume	13 ml
Glass volume	213 ml
Head-space volume	5 ml
Volume occupied by bottle in carton	1920 ml
Glass thickness	0.47 cm

Table 1: Values of the parameters used in this study.

Material	k	c	ρ	κ ($\text{m}^2 \text{s}^{-1}$)	κ ($\text{cm}^2 \text{hr}^{-1}$)
Wine	0.52	4180	1000	0.083×10^{-6}	4.48
Glass	1.0	550	2500	0.727×10^{-6}	26
Air	0.016	1000	1.20	13.3×10^{-6}	480
Cork	0.04	800	250	0.20×10^{-6}	7.2
Paper	0.18	1400	1000	0.071×10^{-6}	2.6

Table 2: Thermal properties of relevant materials. Thermal conductivity k ($\text{W m}^{-1} \text{K}^{-1}$), heat capacity c ($\text{J kg}^{-1} \text{K}^{-1}$), density ρ (kg m^{-3}), diffusivity $\kappa = k/(\rho c)$ in $\text{m}^2 \text{s}^{-1}$ and $\text{cm}^2 \text{hr}^{-1}$.

2.1 Heat conduction through a single wine bottle

2.1.1 Numerical simulation

Consider the conduction of heat through a single bottle of wine when subjected to an elevated temperature. Of interest is the time scale involved for the increase in temperature of the wine. We will consider one typical example where the wine, bottle, air and cork are initially at 10°C . At time $t = 0$ the air surrounding the bottle is raised to 40°C and held constant throughout the simulation. Heat is conducted through the wine, bottle, headspace air and cork. To simplify the calculations convection is ignored. Mathematically we have

$$\nabla \cdot (k \nabla T) = \rho c \frac{\partial T}{\partial t} \text{ with } T(r, z, t = 0) = 10^\circ\text{C} \text{ and } T(r = \text{exterior}, z, t) = 40^\circ\text{C}. \quad (1)$$

Here r and z are the radial and axial coordinates respectively, ∇ is the spatial derivative operator in the appropriate coordinates, t is time, k is the thermal conductivity, ρ the density and c the specific heat capacity. The latter 3 parameters vary with r and z , and their values in the wine, glass, cork and air are given in Table 2. Much of this data is found in [3]. There is nothing special about the values 10°C and 40°C , the results hold generally and these values are used for indicative purposes. The paper label on the wine bottle is ignored as its effect

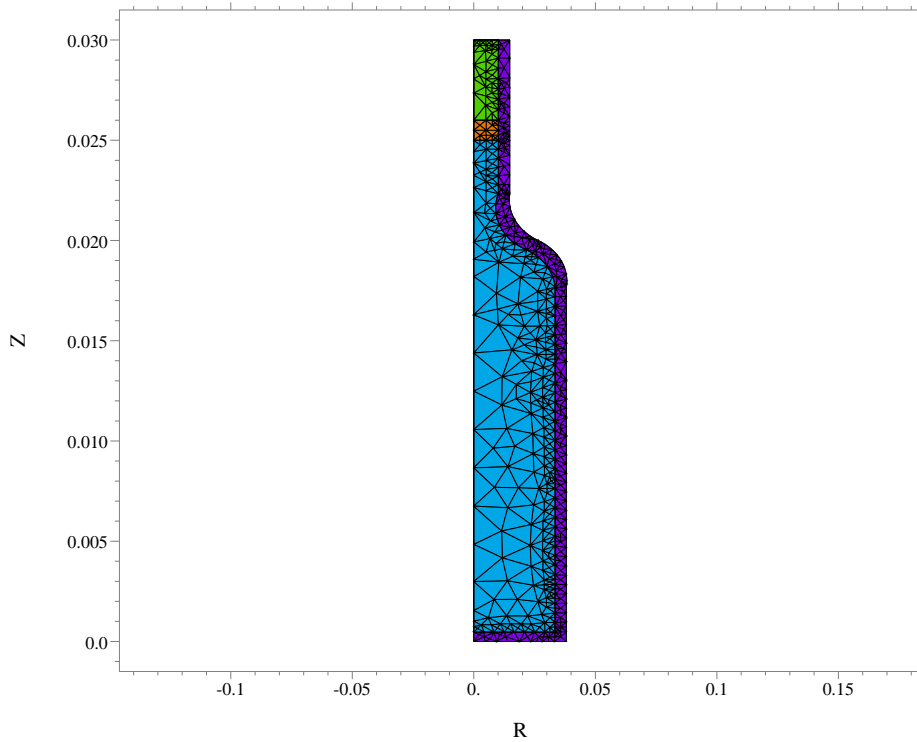


Figure 1: A section of the 3D wine bottle showing the mesh used for the finite element simulation.

on the heat transfer in negligible compared to the glass and wine component. A Dirichlet boundary condition at the air-glass interface is used. This is an extreme case resulting in the fastest heating of the wine and so any estimates obtained for heating times will be on the pessimistic side.

Figure 1 shows a section view of the 3D wine bottle and the finite element mesh used in the simulation. More mesh points are used in areas of large gradients such as through the glass to ensure accuracy of the solution.

Figure 2 shows the pattern of heat conduction through the system with a snapshot of temperature at time 10 minutes as a contour plot. At this stage the glass and the wine in the bottle's neck is close to 40°C , the exterior of the wine is around 35°C and the central area around 11°C . Figure 3 records temperature as a function of time at various positions in the bottle. It is clear from the simulation that the wine in the neck approaches the external ambient temperatures within approximately 1000 seconds (16 minutes), while the temperature in the bottle's middle takes approximately 7000 seconds (2 hours) to almost equilibrate with the ambient.

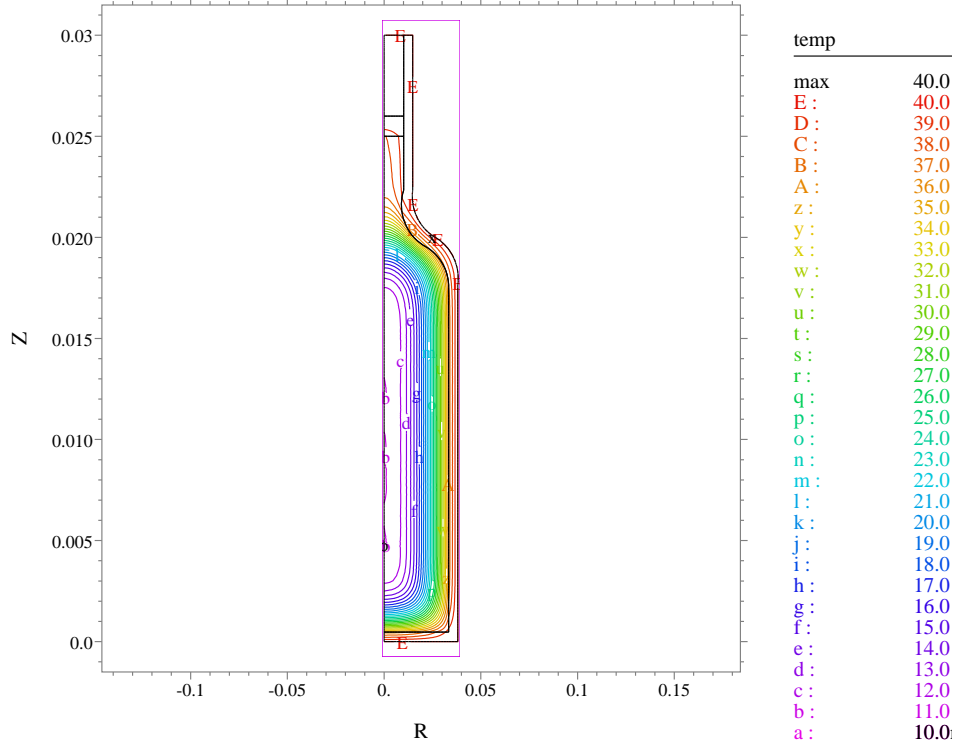


Figure 2: A snapshot of the temperature profile of the wine bottle section after 10 minutes of heating.

2.1.2 Simplified approach

It is possible, using simplifying assumptions, to get a general guide to the time scales involved. For heat conduction problems there is the approximate relationship

$$\text{time taken to travel distance} \sim \frac{\text{distance}^2}{4\kappa}, \quad (2)$$

where κ is the diffusivity ($\kappa = k/(\rho c)$). Hence, for a distance of 3.81 cm (the radius of the bottle) and $\kappa = 4.48 \text{ cm}^2 \text{ hr}^{-1}$ (diffusivity of wine), this yields a time scale of approximately 0.8 hours (2900 seconds) which is consistent with the results presented in Figure 3.

As another approximation consider a well mixed bottle of wine so that the average temperature is the quantity of interest. The average temperature in the wine as a function of time is

$$T_{\text{av}}(t) = \frac{1}{\text{Volume of wine}} \int_{\text{wine}} T(r, z, t) dV.$$

Suppose the average temperature obeys Newton's law of cooling (or heating)

$$\frac{dT_{\text{av}}}{dt} = h(T_{\text{air}} - T_{\text{av}}), \quad (3)$$

for some effective heat transfer coefficient h that needs to be determined. Solving equation (3) gives

$$T_{\text{av}}(t) = T_{\text{air}} + (T_{\text{initial}} - T_{\text{air}})e^{-ht}. \quad (4)$$

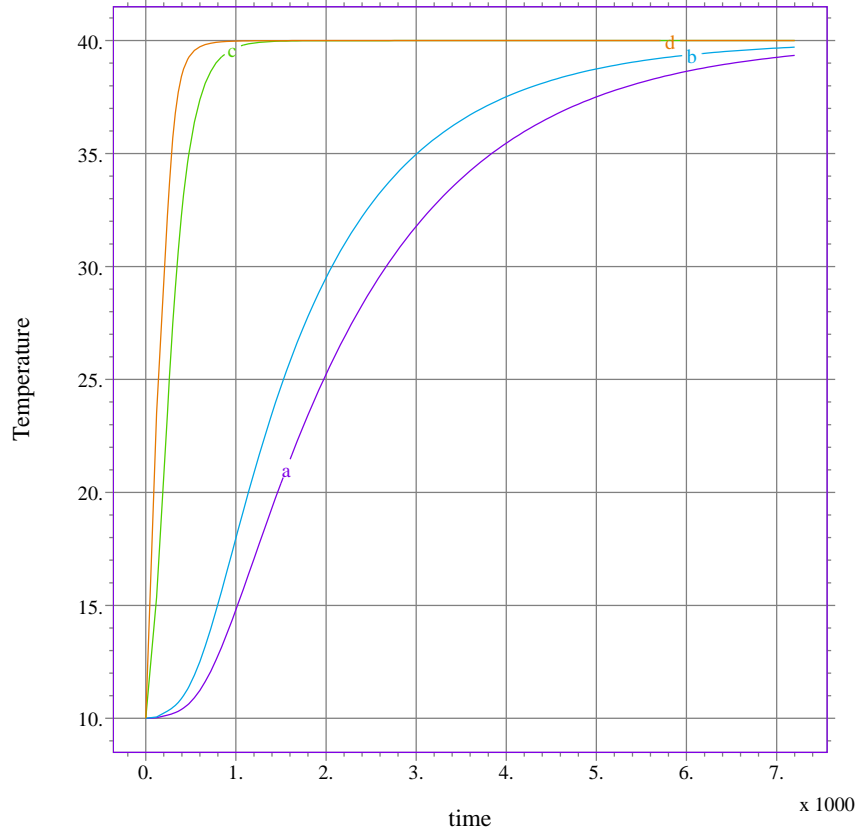


Figure 3: Temperature as a function of time at various places in the bottle for 2 hours (7200 s) of heating. (a) wine in the bottle’s centre near the bottle’s base; (b) wine in the bottle’s centre near the bottle’s top; (c) top of the wine; (d) air at the base of the cork.

Rearranging gives

$$-ht = \log \left(\frac{T_{av} - T_{air}}{T_{initial} - T_{air}} \right) . \quad (5)$$

To verify if investigating the average temperature is a reasonable assumption for our numerical solution we calculate the average temperature of the wine in the bottle from the numerical simulation results and test equation (5). Figure 4 is a plot of equation (5). A straight line plot means we have a good approximation. In the figure the data does indeed fit a straight line after approximately 1000 seconds. The slope of the line is approximately $h = 6.4 \times 10^{-4} \text{ s}^{-1} = 2.3 \text{ hr}^{-1}$. This has shown that the averaged Newton’s law approach is suitable to the accuracy required.

In practical applications there exists other effects not considered in the idealised numerical simulation. These include: (a) convective or mechanical mixing of the wine, (b) cooling of the surrounding air by the wine, and (c) incomplete knowledge of the surrounding air temperature. It may be appropriate to use a heat transfer coefficient from the air to the bottle (instead of keeping the exterior temperature fixed), but in most practical situations it is more useful to use the simple Newton’s law, detailed above, rather than a full three dimensional numerical solution.

The key parameter governing wine the temperature is the heat transfer coefficient h .

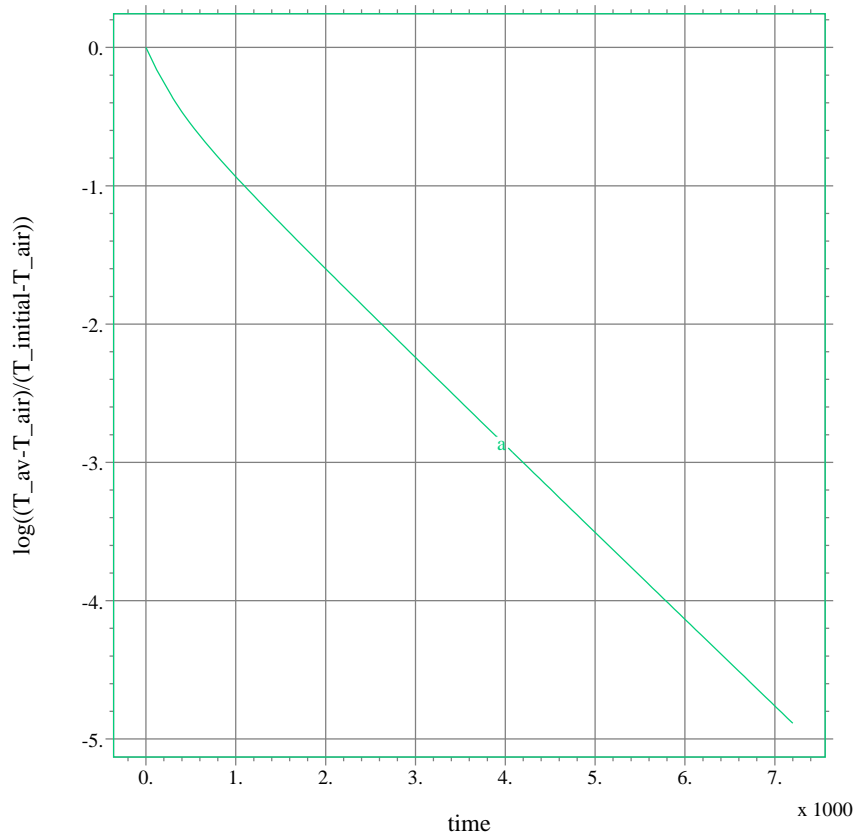


Figure 4: Plot of $\log((T_{av} - T_{air})/(T_{initial} - T_{air}))$ against t ($t = 0$ to 7200 s,) where T_{av} is the average wine temperature. The straight line has slope $6.4 \times 10^{-4} \text{ s}^{-1}$.

Here it has been ‘derived’ from a numerical simulation which represents reality reasonably accurately. In the event that a true experimentally derived value is required the following experiment could be performed. A typical bottle of wine could be placed in a heat bath and the average temperature of the wine plotted in a manner similar to Figure 3. Both the heat bath and the wine should be agitated in a way that duplicates the mixing that will be experienced in real life. The equivalent of Figure 4 yields the heat transfer coefficient h . However, given the results of the next section, it appears unlikely that such accuracy is needed.

2.2 Heat conduction through an array of bottles

2.2.1 Numerical simulation

Armed with the knowledge that it is sufficient to model bottles as averaged ‘lumps’ obeying Newton’s cooling law, it is now appropriate to study heat flow through and around an array of bottles. Numerical simulations are performed for this scenario. The simulation is run using only one row of bottles, but the boundary conditions are periodic so that the results hold for an infinite array of bottles which is more typical of a stacked container. The following assumptions are used.

1. The wine and glass are lumped together into one component with thermal properties of the wine.
2. The cardboard in the packing material is ignored: in real life it mostly serves to prevent convection and has limited thermal effect.
3. The heat transfer is assumed to be purely conductive through the air. Convection is ignored, but if present it may substantially speed heat flow through the array. In this respect the simulations are a best case scenario and in reality the heating time will be shorter due to convection effects.
4. The volume fraction of the wine and glass is 0.5 (corresponding roughly to 981 ml/1920 ml, see Table 1), and the volume fraction of the air is 0.5.

All components in the model are initially at 10°C. To simulate heating in a container or truck during transport the left-hand edge is raised to and kept constant at 40°C for times $t \geq 0$. Mathematically this is

$$\nabla \cdot (k \nabla T) = \rho c \frac{\partial T}{\partial t} \quad \text{with } T(x, y, t = 0) = 10^\circ\text{C} \quad \text{and } T(x = 0, y, t) = 40^\circ\text{C} . \quad (6)$$

Once again, there is nothing special about the values of 10°C and 40°C, the main results below are general. Figure 5 shows a snapshot of temperature at time 300 hours and Figure 6 shows temperature logs at various places in the bottle. After 300 hours the temperature in the first bottle is almost at the outer ambient temperature, the temperature in the third bottle is about 22°C and the seventh bottle is not much above the initial temperature.

2.2.2 Simplified approach

The heat transfer through the system can be well modelled by a one dimensional diffusion equation with constant effective diffusivity κ_{eff} . That is

$$\kappa_{\text{eff}} \frac{\partial^2 T}{\partial x^2} = \frac{\partial T}{\partial t} \quad \text{with } T(x, t = 0) = T_{\text{initial}} \quad \text{and } T(x = 0, t) = T_{\text{hot}} . \quad (7)$$

The effective diffusivity κ_{eff} is an averaged diffusivity and is independent of spatial position and needs to be found from experiments or numerical simulations. The solution of equation (7) is well known to be

$$T(x, t) = T_{\text{hot}} + (T_{\text{initial}} - T_{\text{hot}}) \text{erf} \left(\frac{x}{\sqrt{4\kappa_{\text{eff}}t}} \right) , \quad (8)$$

where the error function, $\text{erf}(y)$, is

$$\text{erf}(y) = \frac{2}{\sqrt{\pi}} \int_0^y e^{-z^2} dz . \quad (9)$$

It is possible to extract a value for κ_{eff} from the 2D numerical simulation. Integrals of error functions are well known and lead to

$$\begin{aligned} \int_0^\infty (T(x, t) - T_{\text{initial}}) dx &= (T_{\text{hot}} - T_{\text{initial}}) \int_0^\infty \left(1 - \text{erf} \left(\frac{x}{\sqrt{4\kappa_{\text{eff}}t}} \right) \right) dx \\ &= \sqrt{\frac{4\kappa_{\text{eff}}t}{\pi}} (T_{\text{hot}} - T_{\text{initial}}) . \end{aligned} \quad (10)$$

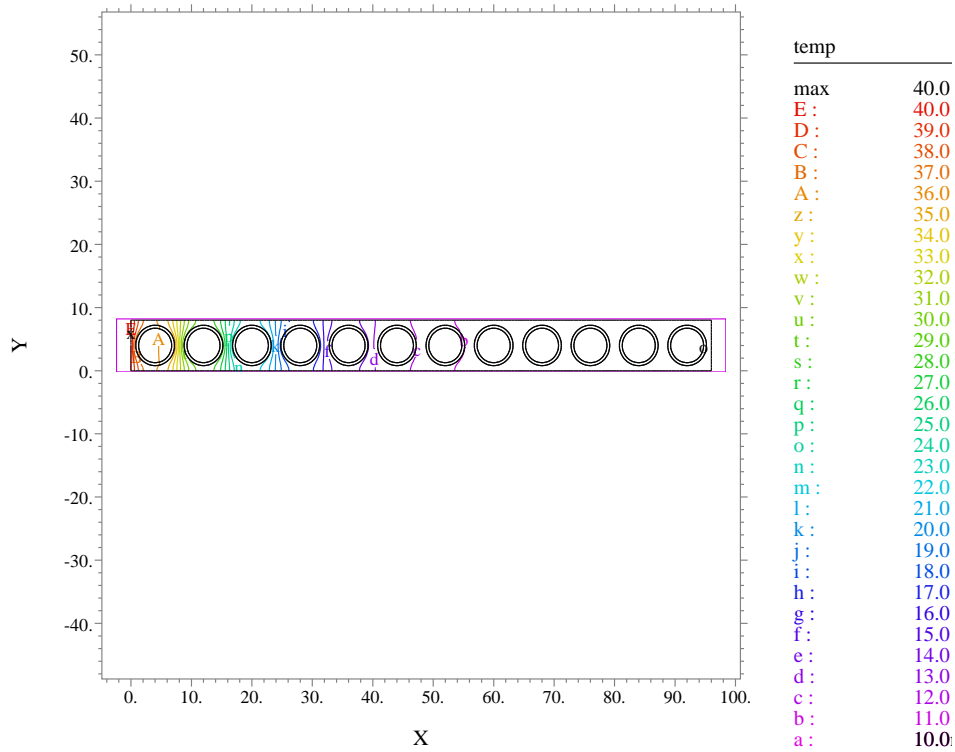


Figure 5: A snapshot of the temperature profile of the bottles and surrounding air after 300 hours of heating. The initial column of bottles (represented by the single bottle on the left) is close to ambient.

Hence, if the theory is correct, plotting the integral on the left against \sqrt{t} should yield a straight line. This is indeed true for this numerical simulation and the straight line has slope

$$\frac{4\kappa_{\text{eff}}}{\pi} = 1.27 \text{ cm}^2 \text{ hr}^{-1},$$

which implies

$$\kappa_{\text{eff}} \approx 1.0 \text{ cm}^2 \text{ hr}^{-1}. \quad (11)$$

The next subsection justifies this quantity with further theory. As has been mentioned before, this parameter dictates the distance travelled by heat through the rule-of-thumb formula equation (2). Therefore, in 1 hour heat will have diffused approximately 1 cm, and in 12 hours approximately 2.5 cm.

2.2.3 The effective diffusivity from theory

In this section the effective conductivity and heat capacity (and hence diffusivity) for the array of wine bottles packed in cartons is explored theoretically in order to check the apparently low value of κ_{eff} quoted in equation (11). Packings of both spheres and cylinders in a space are considered.

Let $\phi = \text{volume fraction of wine} = 0.5$. If the wine and air increase in temperature at the same rate, as suggested by the simulation, the effective heat capacity of the wine-air mixture

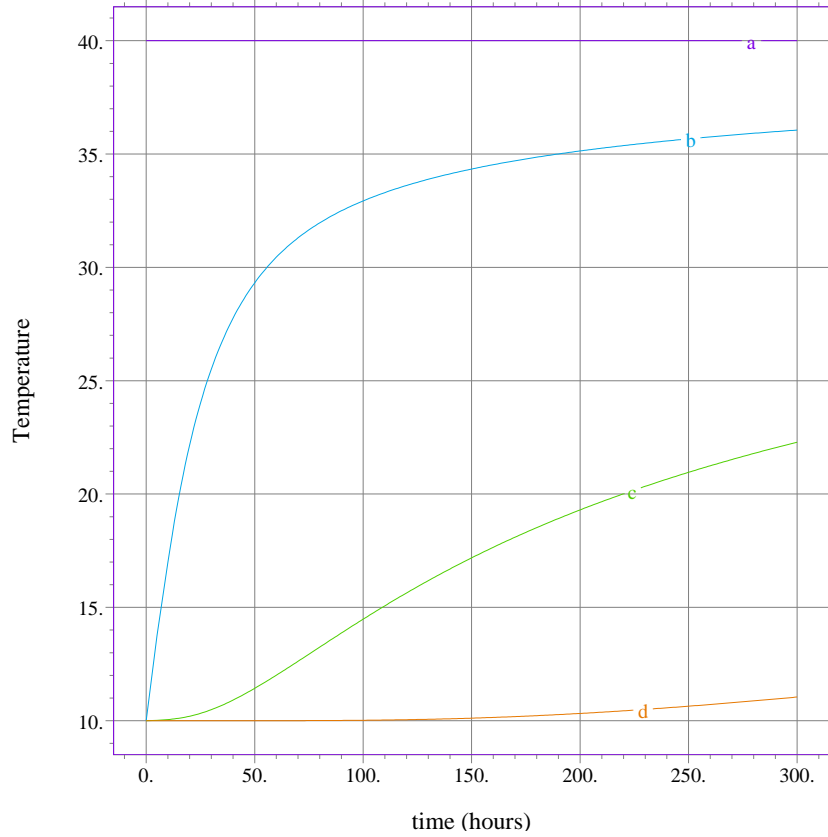


Figure 6: Temperature as a function of time (a) at the left edge; (b) in the first bottle from the left edge; (c) third bottle; (d) seventh bottle.

is simply a weighted average

$$(\rho c)_{\text{eff}} = \phi \times (\rho c)_{\text{wine}} + (1 - \phi) \times (\rho c)_{\text{air}} \approx 2 \times 10^6 \text{ J K}^{-1} \text{ m}^{-3}. \quad (12)$$

The literature reveals many different approximations for the effective thermal conductivity of different shapes packed in air. We will outline five of these.

Series approximation

Treating the wine and air in series (for example wine, air, wine, air, wine, ...) results in

$$k_{\text{eff}}^{\text{series}} = \phi k_{\text{wine}} + (1 - \phi) k_{\text{air}}. \quad (13)$$

This provides an upper bound on k_{eff} . Inserting parameter values yields

$$k_{\text{eff}}^{\text{series}} = 0.268 \text{ W m}^{-1} \text{ K}^{-1}. \quad (14)$$

Parallel approximation

Treating the wine and air in parallel results in

$$\frac{1}{k_{\text{eff}}^{\text{parallel}}} = \frac{\phi}{k_{\text{wine}}} + \frac{1 - \phi}{k_{\text{air}}}. \quad (15)$$

This provides a lower bound on k_{eff} . Inserting parameter values yields

$$k_{\text{eff}}^{\text{parallel}} = 0.031 \text{ W m}^{-1} \text{ K}^{-1}. \quad (16)$$

Maxwell approximation

[6] improved upon the lower bound given by the parallel approximation for the situation for conducting spheres of given volume fraction ϕ periodically dispersed in a insulating medium. His formula is

$$\frac{k_{\text{eff}}^{\text{m}} - k_{\text{air}}}{k_{\text{eff}}^{\text{m}} + k_{\text{air}}} = \phi \frac{k_{\text{wine}} - k_{\text{air}}}{k_{\text{wine}} + k_{\text{air}}}. \quad (17)$$

Inserting parameter values gives

$$k_{\text{eff}}^{\text{m}} = 0.044 \text{ W m}^{-1} \text{ K}^{-1}. \quad (18)$$

Cheng and Torquato approximation

[2] found an approximate expression for the effective conductivity of a dilute mixture of conducting spheres as

$$k_{\text{eff}}^{\text{ct}} = k_{\text{air}} \left(1 - \frac{3\phi}{D_{\text{ct}}} \right), \quad (19)$$

where

$$D_{\text{ct}} = -\beta_1^{-1} + \phi + c_1\beta_3\phi^{10/3} + c_2\beta_5\phi^{14/3} + c_3\beta_3^2\phi^{17/3} + c_4\beta_7\phi^6 + c_5\beta_3\beta_5\phi^7 + c_6\beta_9\phi^{22/3},$$

with

$$\beta_i = \frac{k_{\text{wine}} - k_{\text{air}}}{k_{\text{wine}} + (i+1)k_{\text{air}}/i},$$

and $c_1 = 1.30472$, $c_2 = 0.07232$, $c_3 = -0.52895$, $c_4 = 0.15256$, $c_5 = -0.30667$, $c_6 = 0.01045$. Inserting parameter values yields

$$k_{\text{eff}}^{\text{ct}} = 0.066 \text{ W m}^{-1} \text{ K}^{-1}. \quad (20)$$

Perrins, McKenzie and McPhedran approximation

[9] calculated an approximation to the effective conductivity for the situation where conducting cylinders with volume fraction ϕ are immersed in an insulating medium. To low order, their expression reads

$$k_{\text{eff}}^{\text{pmm}} = k_{\text{air}} \left(1 + \frac{2\beta\phi}{1 - \beta\phi - 0.305827\beta^2\phi^4} \right). \quad (21)$$

Inserting parameter values yields

$$k_{\text{eff}}^{\text{pmm}} = 0.045 \text{ W m}^{-1} \text{ K}^{-1}. \quad (22)$$

The effective diffusivity

The effective diffusivity is given in terms of the effective heat conduction, density and heat capacity as $\kappa_{\text{eff}} = k_{\text{eff}}/(\rho c)_{\text{eff}}$. Using the above approximations gives the results in Table 3. The value of $1 \text{ cm}^2 \text{ hr}^{-1}$ found from the experimental simulation agrees with these theoretical calculations and hence is reasonable.

Approximation	Diffusivity κ_{eff}
Parallel (lower bound)	$1.55 \times 10^{-8} \text{ m}^2 \text{ s}^{-1} = 0.56 \text{ cm}^2 \text{ hr}^{-1}$
Maxwell (lower bound)	$2.22 \times 10^{-8} \text{ m}^2 \text{ s}^{-1} = 0.80 \text{ cm}^2 \text{ hr}^{-1}$
Perrins	$2.27 \times 10^{-8} \text{ m}^2 \text{ s}^{-1} = 0.82 \text{ cm}^2 \text{ hr}^{-1}$
Numerical simulation	$2.77 \times 10^{-8} \text{ m}^2 \text{ s}^{-1} = 1.00 \text{ cm}^2 \text{ hr}^{-1}$
Cheng Torquato	$3.30 \times 10^{-8} \text{ m}^2 \text{ s}^{-1} = 1.19 \text{ cm}^2 \text{ hr}^{-1}$
Series (upper bound)	$1.34 \times 10^{-7} \text{ m}^2 \text{ s}^{-1} = 4.82 \text{ cm}^2 \text{ hr}^{-1}$

Table 3: The effective diffusivity in the various approximations and numerical simulation.

2.2.4 Obtaining κ_{eff} from experiments

Due to the rapidity of heat flow through a single bottle (Section 2.1) relative to an array of bottles, it is appropriate to use the diffusion equation with some experimentally measured effective diffusivity κ_{eff} . In the event that an experimentally derived value for κ_{eff} is required, the following will be of use. A solution of the 1D diffusion equation with oscillatory heating (such as diurnal heating) on one side is

$$T(x, t) = T_{\text{mean}} + A \exp\left(-\sqrt{\frac{\omega}{2\kappa_{\text{eff}}}}x\right) \sin\left(\omega t - \sqrt{\frac{\omega}{2\kappa_{\text{eff}}}}x\right). \quad (23)$$

This solution has the following properties:

- At $x = 0$, the temperature is sinusoidal with frequency ω and amplitude ($T(x = 0, t) = T_{\text{mean}} + A \sin \omega t$). This situation is often encountered with diurnal heating of pallets or containers by the sun either in transit or storage.
- The temperature of the interior ($x > 0$) is also sinusoidal with the same frequency ω , but there is a phase lag given by $\sqrt{\omega/2\kappa_{\text{eff}}}x$. This observation provides one method of measuring κ_{eff} .
- The amplitude of the internal temperature oscillations decays exponentially via the prefactor $\exp(-\sqrt{\omega/2\kappa_{\text{eff}}}x)$. This provides another method of measuring κ_{eff} .

2.3 Slowing temperature increases

In practical applications convective or mechanical mixing of the air surrounding packaged bottles would increase the speed of the heat transfer substantially. The value given in equation (11) should be considered as a ‘best practice’ value to be aimed for by wine distributors or storers. Values inferred from the literature, although never measured particularly carefully, are around $10 \text{ cm}^2 \text{ hr}^{-1}$ or more [4]. This is clearly an area of research that needs further experimental work. The determination of the effective diffusivity is a relatively straightforward experiment to perform using thermocouples and data loggers.

By reducing air flow around the bottles substantial slowing of the heat transfer can be obtained. Because κ_{eff} can theoretically be made small (an order of magnitude smaller than some experiments suggest) a study into the most effective use of thermal blankets, or even simple bubble-wrapping during transport is recommended. Theoretically, over the course of a couple of days in transit, only the bottles closest to the heat source are being overly heated.

This suggests that using a thermal blanket or equivalent to reflect heat, reduce convection and to act as a sacrificial heat sink may ameliorate many potential overheating problems for short haul transport (2 days or less). For long haul transport (4 days or more) the entire container will reach close to the ambient temperature. In this scenario temperature controlled transport and storage is recommended.

2.4 Conclusion

Wine temperature was quantified using numerical simulation for two simple cases: an initially cool bottle standing in a hot environment; an initially cool, large pallet of bottles standing in a hot environment. These are the two extremes which can occur during the transportation and storage of wine. The results imply the following general conclusions.

1. A single bottle of wine exposed to raised ambient temperatures will achieve that ambient temperature in approximately one to two hours. This time is decreased if there is mixing of the wine such as induced by convection or mechanical agitation during transportation.
2. In contrast, if convection of air around wine bottles, cartons and pallets can be minimised, the interior bottles in a standard 12-bottle carton takes approximately four days to achieve ambient temperature. This is because the air, which is conducting the heat, has such a low thermal mass compared to the wine. This scenario can be thought of as ‘best practice’.
3. To achieve close to best practice, convection can be minimised with simple procedures such as shrink/bubble-wrapping pallets, or by using a thick thermal blanket to act as a sacrificial thermal buffer to protect the outer bottles (which achieve ambient temperatures within about a day).
4. The mathematical results also allow other scenarios to be investigated and quantified easily.

3 Gas transport through the cork

When the temperature in the bottle increases the pressure of the air between the wine and the cork increases, forcing air through the cork. As the bottle cools the reverse occurs, drawing fresh air into the bottle. This phenomena is known as cork breathing. We consider here the temperature induced pressure increase in the air gap, the volumetric expansion of the wine, and the permeability of the cork, deriving exact and approximate equations for the air flow through the cork.

3.1 Flow calculations

The increase in volume of the wine is proportional to temperature increase of the wine and is effected little by the pressure of the air

$$V_w(t) = V_w(0)(1 + \alpha_v(T_w(t) - T_w(0))), \quad (24)$$

where $V_w(t)$ [m³] is the volume of the wine, $T_w(t)$ [K] is the wine temperature at time t [s], and α_v [m³ K⁻¹] is the volumetric expansion coefficient of wine. The volume of the bottle, V_b ,

remains effectively constant hence the air volume, $V_a(t)$ [m^3], is related to the wine volume by

$$V_a(t) + V_w(t) = V_b. \quad (25)$$

The flow of air through the cork is relatively slow and pressure driven, hence is well modelled by Darcy's law

$$w(t) = k \frac{P(t) - P_0}{L}, \quad (26)$$

where $w(t)$ [m s^{-1}] is the air velocity through the cork, $k(t)$ is the permeability of the cork [$\text{m}^2 \text{s}^{-1} \text{Pa}^{-1}$] (including the viscosity), $P(t)$ [Pa] is the pressure, P_0 is atmospheric pressure, and L [m] is the length of the cork. This flux of air through the cork is related to the loss of air mass through the cork by

$$\frac{dm_a(t)}{dt} = -\rho_a(t)w(t)A = -kA \frac{\rho_a(t)(P(t) - P_0)}{L}, \quad (27)$$

where $m_a(t)$ [kg] is the mass of air in the gap between cork and wine, $\rho_a(t)$ [kg m^{-3}] is the density of the air, and A [m^2] is the cross-sectional area of the cork.

The permeability, k , is in reality a function of time, although this time dependence only affects the flow minimally. When moist air is flowing out of the bottle, the viscosity will be higher and hence the permeability lower. When dry air flows into the bottle through the cork the permeability is higher. The level of moisture in the air is also temperature dependent. This may be a minor effect but one that can be easily considered by having k as a function of time in the governing equations.

The pressure in the air is modelled by the perfect gas law

$$\frac{P(t)V_a(t)}{m_a(t)T_a(t)} = \frac{P(0)V_a(0)}{m_a(0)T_a(0)} = \beta, \quad (28)$$

where $T_a(t)$ is the temperature of the air and β is a constant.

Combining (27) and (28) gives

$$\frac{dm_a(t)}{dt} = -\frac{k(t)A}{L} \left[\frac{\beta m_a^2(t)T_a(t)}{V_a^2(t)} - \frac{P_0 m_a(t)}{V_a(t)} \right], \quad (29)$$

with the volume correction, equations (24) and (25), giving $V_a(t)$.

Equation (29) is a logistic equation, common in population modelling, with slowly varying parameters; that is $m' = -c_1 m^2 + c_2 m$ with $c_1(t)$ and $c_2(t)$ slowly changing. The equilibrium for (29) occurs when

$$m_a = m_a(0) \frac{V_a(t)}{V_a(0)} \frac{T_a(0)}{T_a(t)} \equiv g(t), \quad (30)$$

hence as the temperature changes, driving volume and pressure changes, the differential equation (29) works to bring $m_a(t)$ into this balance. However, as $g(t)$ varies slowly with time, the mass of air is always chasing this equilibrium, $m_a \rightarrow g$, being closer to it if the cork permeability is large. Numerical solutions to (29) can easily be found and approximate and analytic solutions can also be found. These are explored in Section 3.3.

3.2 Limit of very permeable cork

If the cork closure is assumed very permeable (such as in the case of a defective cork), then the pressure responds rapidly to reach it's equilibrium state, shown in equation (30). The volumetric expansion of wine with an expansion coefficient of $\alpha_v = 2 \times 10^{-4} \text{ K}^{-1}$, gives an approximate increase in wine volume of 4.5 ml over 30 degrees. This is comparable to the head space volume of 5-15 ml. Anecdotally, this is thought to be cause of corks being expelled from the bottle during long term transport when the head space is too small. Thus volumetric wine expansion can cause air loss through the cork of the order of 30 % to 100%.

The mass of air in the head space will also change due to the air expansion and loss through the cork. If $dT_a = T_a(t) - T_a(0)$ then the relative change in mass, assuming no wine expansion, is

$$\frac{m - m_0}{m_0} = \frac{V_a(0)T_a(0)}{V_a(0)T_a(t)} - 1 = \frac{1}{1 + dT_a/T_a(0)} - 1 \quad (31)$$

$$\approx \left(1 - \frac{dT_a}{T_a(0)}\right) - 1 \approx -\frac{dT_a}{T_a(0)}. \quad (32)$$

This gives an approximate measure of the air mass change due to air pressure changes. For a temperature rise of 30 degrees, an initial temperature of $T_a(0) = 283 \text{ K}$ (10° C) this gives magnitudes of approximately 11% mass flow. This is an upper bound on the air flow into the bottle of approximately 11% mass loss/gain in the course of a 30 degree temperature rise during one day. Hence approximately ten days of diurnal temperature changes will change virtually all the air in the bottle in the limit of a very permeable cork due to air expansion changes only.

3.3 Approximate solutions

This section explores some approximate solutions to equation (29) with the cork no longer very permeable so that its permeability is now important. Each of the solutions assume that the driving temperature, $T(t)$, changes slowly or remains close to the initial equilibrium state. It is not immediately apparent which approximation is the most valid until numerical simulations can compare the results with the full numerical solution. In our simulations we consider no volumetric wine expansion, equivalent to the situation of a large head space. Later work will consider the effect of air loss due to both wine expansion and air temperature.

It is informative here to non-dimensionalise the system with respect to typical scales:

$$m_a(t) = m_a(0) m(t^*), \quad V_a(t) = V_a(0) V(t^*), \quad (33)$$

$$P_a(t) = P_a(0) P(t^*), \quad t = t_0 t^*, \quad (34)$$

$$k(t) = k(0) k^*(t^*), \quad (35)$$

where $*$ denotes non-dimensional variables, and the typical time scale t_0 can be shown to be

$$t_0 = \frac{L V_a(0)}{k(0) A P_a(0)}.$$

Using these scalings (29) reduces to

$$\frac{dm(t)}{dt} = -c_1(t) m(t)^2 + c_2(t) m(t), \quad (36)$$

where we have dropped the * notation herein, and

$$c_1(t) = \frac{k(t)T(t)}{V^2(t)}, \quad c_2(t) = \frac{k(t)}{V(t)}. \quad (37)$$

Changes in the temperature $T(t)$ forces equation (36) from the equilibrium state, $m = c_2(t)/c_1(t) = V(t)/T(t) = \gamma(t)$, with $k(t)$ and $V(t)$ changing slightly. We note that $c_1(t)$ contains the main time dependent term $T(t)$, which drives the process. However, $c_2(t)$ only varies slightly with time, as both k and V only change slightly with temperature and time.

First Approximate Solution

The first approximate solution assumes $c_1(t)$ and $c_2(t)$ are approximately constant in equation (36), leading to

$$m(t) \approx \frac{\gamma m(0)}{m(0) + (\gamma - m(0))e^{-c_2 t}}, \quad (38)$$

where $\gamma \equiv \gamma(t)$ and $c_2 \equiv c_2(t)$. This solution will be exact if γ and c_2 are constant. As $t \rightarrow \infty$ this gives the equilibrium solution $m \rightarrow \gamma$. This solution is most valid when the temperature change is a rapid jump, giving new values of c_1 and c_2 which do not then change with time.

Second Approximate Solution

A second approximate solution uses a technique described in [10]. The method uses two different time scales, $t_0 \equiv t$ and $t_1 \equiv \epsilon t$, with ϵ small and $c_2 = c_2(t_1)$ and $\gamma = \gamma(t_1)$. That is, c_1 and c_2 vary on the slower time scale, while $m(t)$ chases the equilibrium on a faster time scale. The mass is written as $m = m(t_0, t_1, \epsilon)$ with equation (36) becoming

$$\frac{\partial m}{\partial t_0} + \epsilon \frac{\partial m}{\partial t_1} = -c_2(t_1)(m - \gamma(t_1)). \quad (39)$$

Expanding in a perturbation series $m = m_0(t_0, t_1) + \epsilon m_1(t_0, t_1) + \dots$ and equating coefficients gives

$$\frac{\partial m_0}{\partial t_0} = -c_2(t_1)(m_0 - \gamma(t_1)) \quad \text{and} \quad \frac{\partial m_1}{\partial t_0} = -c_2(t_1)m_1 - \frac{\partial m_0}{\partial t_1}. \quad (40)$$

These two equations have solutions, using the initial condition $m = m_a(0) + \epsilon 0 + \dots$,

$$m_0 = (m(0) - \gamma)e^{-c_2 t_0} + \gamma, \quad (41)$$

$$m_1 = \left(\gamma' t + \frac{1}{2}(m(0) - \gamma)c_2' t^2 - \frac{\gamma'}{c_2} e^{c_2 t} + \frac{\gamma'}{c_2} \right) e^{-c_2 t_0}, \quad (42)$$

where γ and c_2 are functions of t_1 and hence $\gamma' = d\gamma/dt_1$. This solution satisfies the initial condition $m = m(0)$ and has the long term behaviour

$$m(t) \approx \gamma(\epsilon t) - \epsilon \frac{\gamma'(\epsilon t)}{c_2(\epsilon t)}. \quad (43)$$

That is, the mass attempts to reach the equilibrium point γ but since this equilibrium keeps changing slowly with time, it lags by a small amount.

Third Approximate Solution

Our third approximate solution is to assume $c_1(t)$ is a slowly varying function of time and that $c_2(t) = c_2$ remains constant, since only c_1 contains the driving term $T(t)$ and c_2 contains terms which only vary slightly with time. With this assumption the solutions obtained in [10] can be followed exactly to give

$$m \approx \frac{\gamma(\epsilon t)m(0)}{m(0) + \left(\gamma(\epsilon t) - \frac{\gamma(\epsilon t)}{\gamma(0)}m(0)\right)e^{-c_2 t}} - \epsilon \frac{\gamma'(\epsilon t)\gamma^2(0) - \gamma'(0)\gamma^2(\epsilon t)e^{-c_2 t}}{c_2\gamma^2(0) \left(1 + \left[\frac{1}{m(0)} - \frac{1}{\gamma(0)}\right]\gamma(\epsilon t)e^{-c_2 t}\right)^2}. \quad (44)$$

This has the required behaviour that at $t = 0$ then $m(0) = 0$. As $t \rightarrow \infty$ then $m \rightarrow \gamma - \epsilon \frac{\gamma'}{c_2}$ indicating the same time lag behaviour as shown earlier. Usually the temperature change is gradual, moving the system from an initial equilibrium state when $m(0) = \gamma(0) = 1$ towards a new equilibrium state as $\gamma(t)$ and $c_2(t)$ change with temperature. If this were the case the solution is greatly simplified to be (43). However, if there is an initially rapid rise in temperature then the initial state can be considered not to be in equilibrium, so $m(0) = 1$ but $\gamma(0) \neq 1$, and (44) is necessary. Note that the first term in (44) is similar, but not exactly the same as (38).

3.4 Results

This section considers the numerical and approximate solutions for two different temperature change cases. The first case is a gradual rise in temperature (see Figure 7) and the second case a sinusoidally variable temperature for different amplitude and period.

Figure 8 shows the mass of air changing as a function of time when the temperature changes linearly as $T = 1 + \epsilon t$, $\epsilon = 0.1$ (as shown in Figure 7) with $V(t) = k(t) = 1$, and $m(0) = 1$. Equation (44) represents the full numerical solution slightly better than (42). The asymptotic solution given by (43) is also shown. As discussed earlier, the mass of air approaches this asymptotic solution for large time, mirroring the lower equilibrium solution $\gamma(t)$ but with a lag $\epsilon \gamma'(\epsilon t)/c_2(\epsilon t)$. Approximations one (38) and approximation two (zeroth order, (41)) both asymptote to the wrong solution $\gamma(t)$, although they well represent the exact solution for small time. All solutions remain sandwiched between the lower limit, $m = \gamma(t)$, and the upper limit, equation (43).

Of main interest for the wine transport and storage is regular diurnal temperature changes and a calculation of the mean air flow in and out of the cork. That is, for a temperature profile

$$T = 1 + a \sin(\epsilon t). \quad (45)$$

Figure 9 shows the air mass change for a sinusoidal temperature change $T = 1 + 0.1 \sin(\epsilon t)$ with $\epsilon = 0.3$. The same notation is used as for Figure 8. Many of the curves are indistinguishable except at small times. Approximations (44) and (42) almost perfectly match the asymptotic solution given by equation (43). The inaccurate approximation (41) matches the highly permeable cork case $m = \gamma(t)$. For this large value of ϵ the numerical solution does not match the various asymptotic solutions. For $\epsilon < 0.1$ the numerical result matches the asymptotic solution.

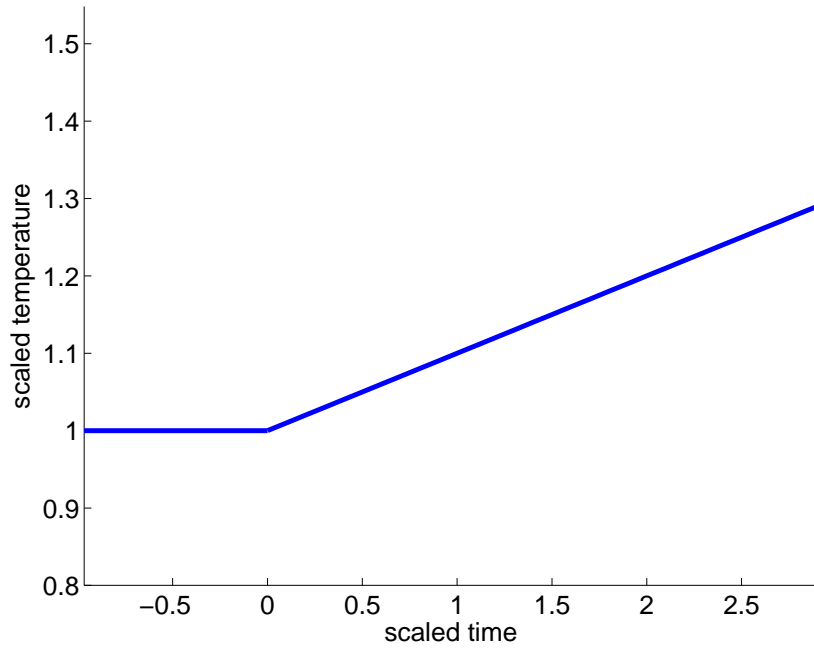


Figure 7: The temperature change being considered, a gradual linear increase.

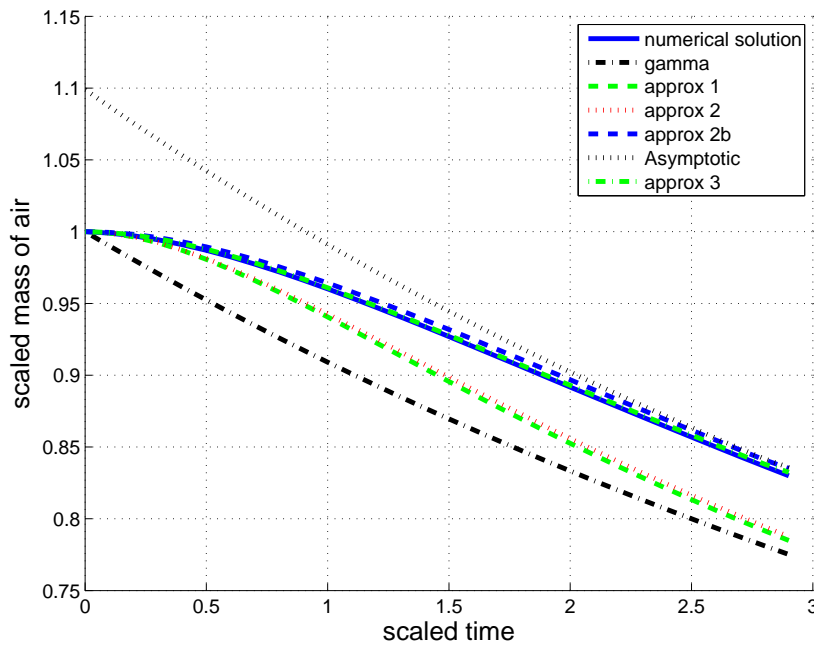


Figure 8: Air mass versus time for a linear temperature rise. Blue solid line is numerical solution to (29). Black dot-dash line is $m = \gamma(t)$. The green dashed line is approximation one (38). The red dotted line the second approximation (41). The full second approximation, (41) and (42), is the blue dashed line ‘approx 2b’. The third approximation, (44), is the green dot-dash line. The asymptotic solution (43) is the upper black dotted line.

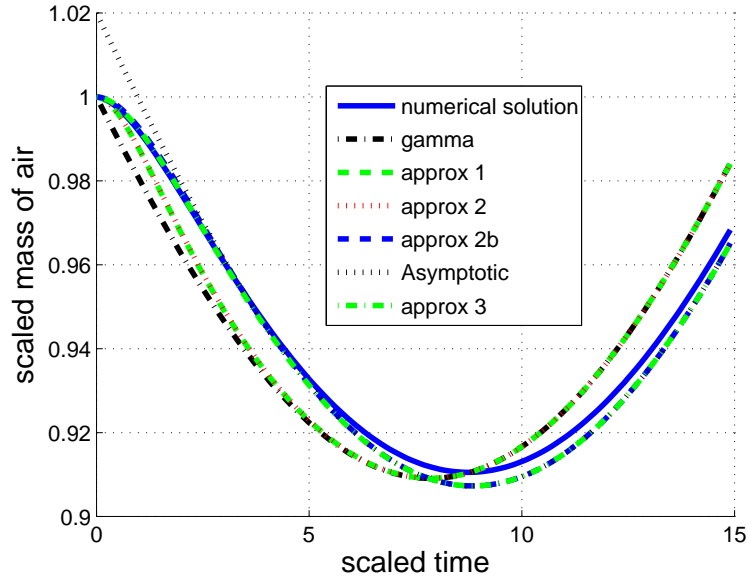


Figure 9: Air mass change for sinusoidal temperature variation with the same notation and parameters as Figure 8

We require the difference between the maximum and minimum values of air mass, $\bar{m} = 2(\max(m) - \min(m))$, since this is how much air has flowed in and out of the bottle. Figure 10 illustrates \bar{m} for varying ϵ and a , showing an expected linear behaviour of mass flux with increasing magnitude, at least for small a . This illustrates the limitation of the various approximations as ϵ increases. When $\epsilon \rightarrow 0$ the temperature changes are so slow that in effect the cork is completely permeable. As ϵ increases, the oscillations in temperature are fast enough that the air does not have time to flow out of the cork before the temperature has reversed direction. Hence one expects that $\bar{m} \rightarrow 0$ as ϵ increases. This behaviour is not reflected in any asymptotic solutions as it is a highly nonlinear effect. Large ϵ corresponds to a long period of temperature oscillations such as seasonal variation under cellar conditions.

3.5 Future Work

There are several aspects of this work that could be explored. First, the permeability of wine cork is not well known and this is the crucial parameter in determining mass of air flow through the cork. Some data exists on dry cork board ($k \approx 2.4 - 5.7 \times 10^{-11} \text{m}^2$ [7]) however this is not indicative of permeability of a wet compressed cork. Second, the numerical results on air flow through cork included here took $V(t) = k(t) = 1$ which is a simplification to allow each effect to be studied separately. Future work will include temperature dependent expansion of the wine, the viscosity of moist and dry air, and the temperature dependent moisture content in the air. An additional effect is the time delay between thermal diffusion into the air and wine within the bottle, the wine exhibiting a longer time lag. This may have a small effect on the air flow through the cork.

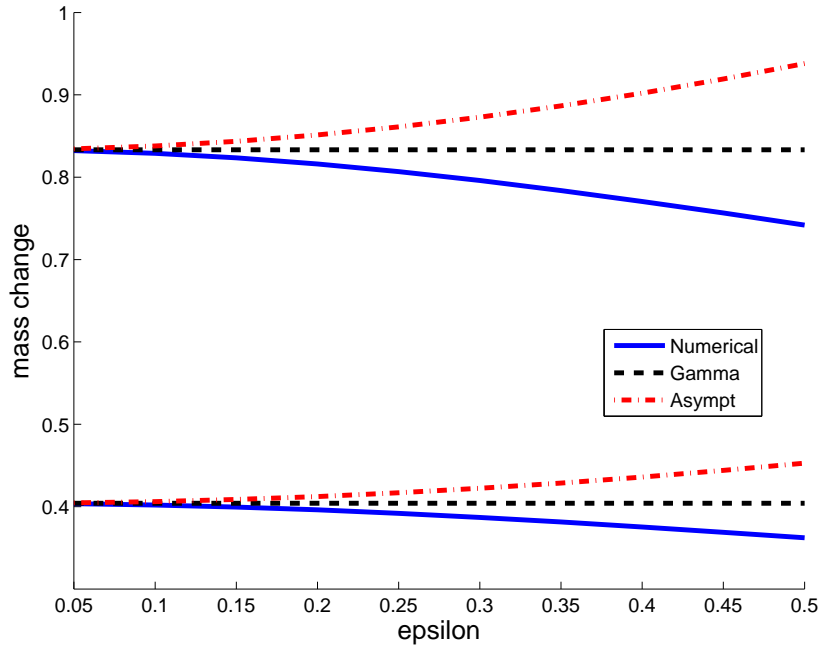


Figure 10: Total diurnal mass change versus parameters a and ϵ in equation (45). The curve shows mass flow versus ϵ with $a = 0.1$ (lower curves) and $a = 0.2$ (upper curves). The behaviour is shown using numerical solution (solid blue lines), the limiting solution $m(t) = \gamma(t)$ (black dashed lines), and asymptotic solution (equation (43), red dot-dash lines).

4 Oxidation of wine

Wine changes in the bottle through a sequence of oxidative reactions, mediated through the supply of oxygen to the wine. During storage at uniform temperature, oxygen is supplied to the wine by diffusion through the cork, and this occurs at a very slow rate. During transport, or if the external temperature fluctuates in storage, thermal expansion and contraction of the wine can cause forced flow of oxygen through the cork, and this is described by Darcy's law, as described in Section 3.

4.1 Wine chemistry

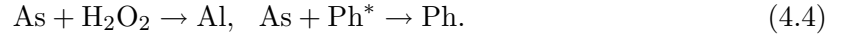
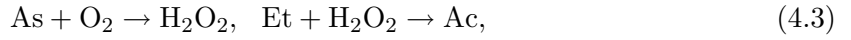
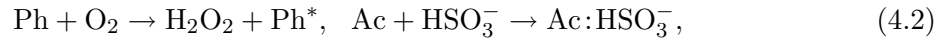
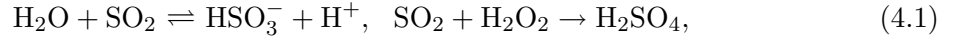
The primary oxidative reaction of importance is the oxidation of a class of phenols. Amongst these are the tannins, and the oxidative effect on some of these is to cause *browning* of the wine, for example discolouration [5]. A secondary effect of the oxidation of phenols is the production of hydrogen peroxide, H_2O_2 , and the peroxide is a strong oxidiser, which reacts with the alcohol (ethanol, $\text{C}_2\text{H}_6\text{O}$) to produce acetaldehyde, $\text{C}_2\text{H}_4\text{O}$, which causes deterioration in aroma and taste of the wine.

In order to prevent such reactions, it is common practice to add sulphur dioxide, SO_2 , which reacts directly in its molecular form with the peroxide to form sulphuric acid, H_2SO_4 . When dissolved in water, SO_2 dissociates to form the bisulphite ion HSO_3^- , and this bisulphite takes acetaldehyde out of solution by forming a bound complex. This dissociation of SO_2 is highly pH dependent.

Sometimes ascorbic acid (vitamin C, $C_6H_8O_6$) is added to prevent discolouration; it does this by effectively reversing the phenol oxidation. However, ascorbic acid has other undesirable effects: it reacts with peroxide to form an aldehyde, another chemical which causes taste deterioration, and it oxidises to form more peroxide.

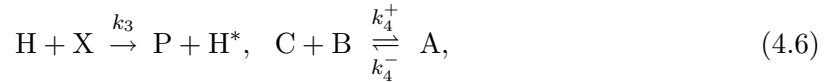
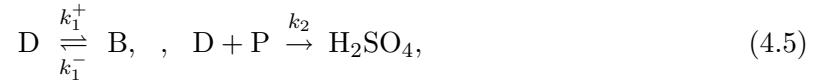
4.2 Differential equations

A set of reactions to describe these processes is the following:



In these reactions, we denote ascorbic acid as As, ethanol as Et, acetaldehyde as Ac, aldehyde as Al, phenol as Ph or Ph^* ; Ph^* represents the more oxidised, discoloured form. The bound acetaldehyde–bisulphite complex is denoted $Ac:HSO_3^-$.

We rewrite these equations using the abbreviations D for dioxide, B for bisulphite, P for peroxide, H and H^* for the phenol and oxidised phenol, X for oxygen, C for acetaldehyde, S for ascorbic acid, A for the $Ac:HSO_3^-$ complex, and L for the aldehyde. Adding rate constants, they are



We apply the law of mass action to these reactions, and this leads to the following set of ordinary differential equations, in which we use the same symbols to denote the concentrations of the chemicals. We suppose the wine is well-mixed, which will be a valid assumption during transport, although not necessarily during storage, and we also suppose that ethanol is essentially unchanged, being present in large quantity (e. g., 12% by volume). The equations are

$$\dot{D} = k_1^- B - k_1^+ D - k_2 DP, \quad (4.9)$$

$$\dot{B} = -k_1^- B + k_1^+ D - k_4^+ BC + k_4^- A, \quad (4.10)$$

$$\dot{P} = k_3 HX + k_5 SX - k_6 P - k_7 SP - k_2 PD, \quad (4.11)$$

$$\dot{H} = -k_3 HX + k_8 SH^*, \quad (4.12)$$

$$\dot{H}^* = k_3 HX - k_8 SH^* [-R], \quad (4.13)$$

$$\dot{X} = -k_3 HX - k_5 SX [+V], \quad (4.14)$$

$$\dot{C} = -k_4^+ BC + k_4^- A + k_6 P, \quad (4.15)$$

$$\dot{S} = -k_5SX - k_7PS - k_8SH^*, \quad (4.16)$$

$$\dot{L} = k_7PS, \quad (4.17)$$

$$\dot{A} = k_4^+BC - k_4^-A, \quad (4.18)$$

where the overdot represents the time derivative.

The posited terms V and R warrant some discussion. As wine matures, the phenols are oxidised to form larger molecules, and these eventually precipitate and fall out of solution. If necessary, this could be described by a suitable loss term R . Consulting equation (4.14), we see that oxygen is depleted by its reaction, principally with the phenols, and this depletion takes about a week under normal circumstances [1]. Once the oxygen is removed, there is no source for peroxide, total SO_2 ($B + D + A$) is conserved, the reactants reach steady state, and the reactions cease. Thus the continuing maturation and aging of wine requires the supply of oxygen, and this is indicated by the source term V .

4.3 Determining a usable model

In order to analyse these equations, we would need estimates of the rate constants and, importantly, their variation with temperature. However, this information is not readily available and is unlikely to be available in the future. Instead, we are motivated by the experimental results of [8], who interpreted SO_2 loss and browning in terms of a first order rate equation. Implicitly, he supposes that SO_2 satisfies a first order rate equation of the form

$$\dot{D} = -k_{\text{eff}}D, \quad (4.19)$$

where the effective rate coefficient k_{eff} is a strong function of temperature of the Arrhenius form

$$k_{\text{eff}} = k_0 \exp \left[-\frac{E}{RT} \right], \quad (4.20)$$

where E is the activation energy, R is the gas constant, and T is absolute temperature. One object of analysing the system of equations (4.9)–(4.18) is to see in what circumstances an effective equation of the form (4.19) can be obtained. In the present paper, we limit ourselves to this goal.

We suppose that the dissociation reactions are fast. If $k_4^\pm \gg \frac{1}{TS}$, where TS is the time scale of interest (of SO_2 decay), then $k_4^-A \approx k_4^+BC$ determines A . If also $k_1^\pm \gg \frac{1}{TS}$, then $k_1^-B \approx k_1^+D$ and thus the dioxide satisfies the rate equation

$$\dot{D} \approx -k_2PD. \quad (4.21)$$

This provides a single rate equation for D , providing the peroxide concentration is constant. It remains to consider whether this is true.

We will suppose that the peroxide reactions are fast, since peroxide is a strong oxidant, so that we take (4.11) to be at equilibrium. Then

$$P \approx \frac{k_3HX + k_5SX}{k_6 + k_7 + k_2D}. \quad (4.22)$$

We suppose also that (with a source term V) the oxygen equation (4.14) is fast (since oxygen concentrations are very low), so that X equilibrates as

$$X \approx \frac{V}{k_3H + k_5S}. \quad (4.23)$$

Then (4.21) becomes

$$\dot{D} = -\frac{k_2VD}{k_6 + k_7S + k_2D}. \quad (4.24)$$

The rate law (4.24) forms the essential conclusion of this analysis. Further forms are possible, depending on the behaviour of the ascorbic acid S . If the removal of S is fast, then $S \approx 0$, or if the reaction is slow, then $S \approx \text{constant}$. In any event, (4.24) takes the well known Michaelis–Menten form

$$\dot{D} = -\frac{VD}{K + D}, \quad (4.25)$$

where

$$K = \frac{k_6 + k_7S}{k_2}. \quad (4.26)$$

In this form there are good prospects to be able to fit this model to experimental results and obtain a useful model of the aging process. There are only 3 parameters (k_2 , k_6 and k_7) to fit experimental data to. The limited experimental data available on the aging process supports the Michaelis-Menton form for the model and in some cases suggests an even simpler first order form with a single rate constant that is temperature dependent through an Arrhenius relationship. It is a relatively straightforward experiment to perform to test whether the single Arrhenius rate constant is applicable. Details of this experiment can be found in [8]. If $D \ll K$, then we regain the first order rate equation (4.19). If, for example, $S = 0$ or k_7 is small, then, with an obvious notation,

$$k_{\text{eff}} = \frac{k_2V}{k_6} = \frac{k_2^0V}{k_6^0} \exp \left[-\frac{(E_2 - E_6)}{RT} \right], \quad (4.27)$$

and the effective activation energy of the reaction is $E = E_2 - E_6$.

As a first point in determining an appropriate model for the aging process experimental data should be fitted to (4.19). If this provides a good fit then a more complicated model is not required. If the fit is not good then the the Michaelis–Menten form (4.24) should be used.

4.4 Applying a model

Using the limited data available in the literature for one red wine type (see [8]), calculations were performed for the first order Arrhenius case (4.19) to quantify the effect of elevated temperature on the SO₂ reduction and the browning. From [8, 1] the activation energy for the red wine the used in their experiments was $E = 35,700 \text{ kJ mole}^{-1}$ for SO₂ and $E = 66,400 \text{ kJ mole}^{-1}$ for browning. Figure 11 shows the results of solving (4.19) for the SO₂. The percentage decline in SO₂ is shown for 3 different temperatures (10, 20 and 40° C) versus time. Clearly the elevated temperatures have a dramatic effect on the SO₂ decline with the higher temperatures leading to more rapid SO₂ reduction.

Results of solving (4.19) were compared to ideal cellaring conditions at 10°C and expressed as a percentage of time to reach the same state (% of SO₂ present or % of browning occurring)

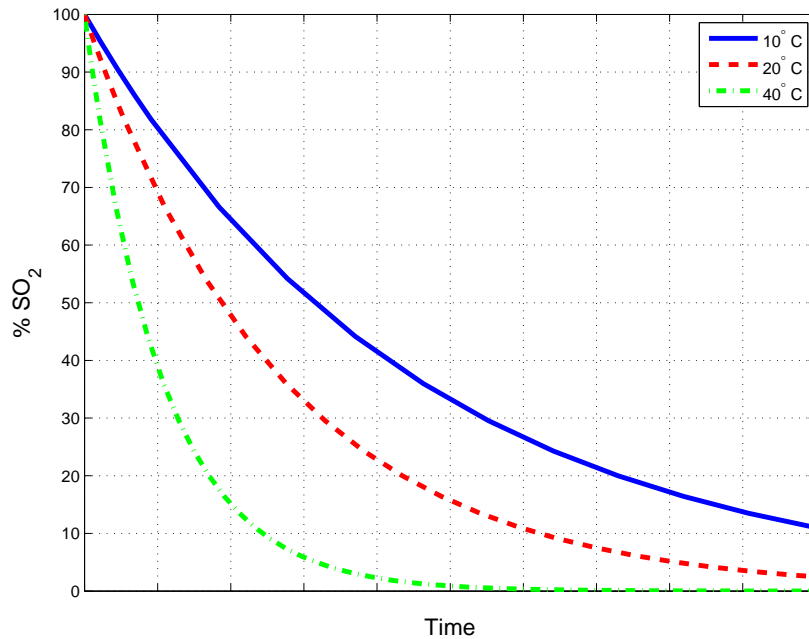


Figure 11: Percentage decline in SO₂ for 3 different temperatures from solving (4.19) using the data from [8].

relative to ideal conditions. Figure 12 shows the effect of elevated temperature on the shelf life. At 20°C the time to reach the critical SO₂ level was 59% of ideal conditions and 38% for browning. That is the shelf life measured by SO₂ level is almost half and measured by browning is approximately one third compared to ideal cellar conditions. This dropped dramatically for 40°C to 23% and 8% respectively. Depending on which is the critical parameter (SO₂ level or browning) this means that at 40°C the shelf life is between 8% and 23% of the ideal cellaring shelf life. So, for example, a wine with a shelf life of approximately 10 years under ideal conditions would have its shelf life reduced to between about 10 months and 2.3 years depending on which measure of shelf life (browning or SO₂ level) was considered.

With better data derived from experimental work this method could be used to give reasonable estimates for the reduction in shelf life of wine when subjected to elevated temperatures. Both Michaelis-Menton type reactions and first order reactions can be considered in a straightforward manner in these types of models. Different wines will no doubt have different activation energies and these will need to be determined experimentally for each wine type to use these models. It is a relatively straightforward experiment to determine these activation energies and this is certainly the first step that should be considered to determine useful data for the models.

5 Conclusion

In summary three separate models have been developed for various aspects related to the shelf life of wine. These are heating of wine during transport, oxygen ingress through the cork and

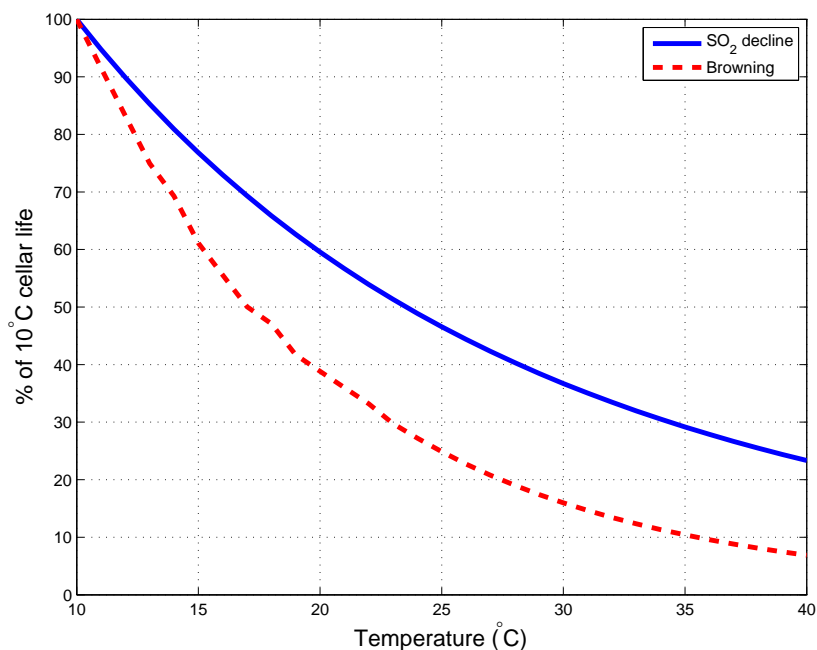


Figure 12: The temperature dependence of shelf life of the red wine considered in [8] as a percentage of the shelf life at ideal cellaring conditions

oxidative chemistry models. Estimates for the time wine takes to almost reach ambient external temperature for both single bottles (order of two hours) and in a container (order of 4 days) have been obtained. Long haul transport was found to be the area most affected by heating issues. Air flow through the cork was determined under oscillatory temperature regimes (either a domestic diurnal scenario or a longer cellaring seasonal one). A critical parameter is the cork permeability which is currently unavailable for wet compressed cork as found in the bottle. It is recommended that straightforward experiments be conducted to determine this parameter. The model developed for the oxidation of wine was shown to reduce down to the well known Michaelis-Menton form or the even simpler first order Arrhenius form under certain assumptions. If these relationships are appropriate then relatively simple models of the shelf life of components (for example sulphur dioxide or browning) are easily developed. Experiments to test the model assumptions have been recommended.

Followup from the industry partner (Provisor) and wine producing companies at an industry forum shows that there is considerable interest in this project. The heating of wine in containers during long haul transport is of particular concern to the major exporting wineries as they sometime suffer substantial losses as overheating occurs in shipping to the Northern hemisphere due to transitting through the tropics. Many companies have thermocouple traces (all unpublished data) of temperature within the containers that they have difficulty interpreting. The current study will be of assistance to them and this is an area of future research. Oxygen ingress through the cork is considered less of an issue as increasingly wine is being bottled with other closures (mostly screw cap) although it is important in some markets (notably the USA and France) where cork is still the preferred closure. The models for

the oxidation of wine presented is an area of ongoing research in conjunction with Provisor. Future work will be to construct similar models for reductive chemistry which is more applicable to wine bottled under screw cap. Other components of the wine, such as tannins and flavours, will also be included in the models.

References

- [1] Boulton, R.B., Singleton, V.L., Bisson, L.F. & Kunkee, R.E. (1997) *Principles and practices of winemaking*, CBS, New Delhi, India.
- [2] Cheng H. & Torquato, S. (1997) Effective conductivity of dispersions of spheres with a superconducting interface, *Proc. Roy. Soc. London A*, **453**, 145-161.
- [3] Kaye, G.W.C. & Laby, T.H. (1973) *Table of physical and chemical constants and some mathematical functions*, 14ed. Longman, New York.
- [4] Laffer, P.L. (2004) Management of wine quality during transport *Proceedings of the twelfth Australian wine industry technical conference*, ed. R Blair, P Williams and S Pretorius, 219-221.
- [5] Li, H., Guo, A. & Wang, H. (2008) Mechanisms of oxidative browning of wine, *Food Chemistry*, **108**, 1-13.
- [6] Maxwell, J.C. (1891) *A treatise on electricity and magnetism*, Dover, New York.
- [7] Nield, D.A. & Bejan, A. (1999) *Convection in porous media (2nd ed)*, Springer, New York.
- [8] Ough, C.S. (1985) Some effects of temperature and SO₂ on wine during simulated transport or storage, *Amer. J. Enol. Vitic.* , **36** (1), 18-22.
- [9] Perrins, W.T., McKenzie, D.R. & McPhedran, R.C. (1979) Transport properties of regular arrays of cylinders. *Proc. Roy. Soc. London, Ser. A*, **369**, 207-225.
- [10] Shepherd, J.J. & Stojkov, L. (2007) The logistic population model with slowly varying carrying capacity, *ANZIAM J(E)* (EMAC2005), **47**, C492-C506.